N° ordre : 2015-44

Thèse de l'Université de Lyon
délivrée par l'Ecole Centrale de Lyon
Spécialité : Electronique, microélectronique, optique et lasers, optoélectronique, microondes, robotique

soutenue publiquement le 11 Décembre 2015
par
M Jérémie Maire

préparée au laboratoire INL

titre :

Thermal phonon transport in silicon nanostructures

Transport des phonons dans les nanostructures de silicium

Ecole Doctorale d'Electronique, Electrotechnique et Automatique

composition du jury :
M Christian Seassal en qualité de directeur de thèse
M Masahiro Nomura en qualité d'encadrant
M Iilari Maasilta en qualité de rapporteur
M Stephan Dilhaire en qualité de rapporteur
M Olivier Bourgeois en qualité d'examinateur
M Sebastian Volz en qualité d'examinateur
M Karl Joulain en qualité d'examinateur

Acknowledgments

First and foremost, I offer my sincerest gratitude to my research supervisor, Masahiro Nomura, who accepted me as a full-fledged member of his laboratory. I would like to thank him for his trust, patient guidance, and the many advices he gave me.

My deep gratitude goes to Christian Seassal, who accepted to supervise this work despite the distance and helped me along the way for a smooth development of the thesis. I am also grateful for the various useful discussions we had.

Special thanks to Dominique Collard without whom I would not have been able to do my PhD here. Not only did he accept and support my application, but he made it possible to have the support of CNRS.

I would like to thank all the people from the Institute of Industrial Science, the University of Tokyo who helped me all along. My thanks go to Kazuhiro Hirakawa for the numerous fruitful discussions. I am also thankful to Satomi Ishida, Munekata Arita and Kenji Yoshida for their support and training in clean room and the many discussions we had.

I would also like to express my gratitude to the students and members of Nomura laboratory, especially Wataru Shimizu, Ryouhei Tanabe, Yuta Kage, Roman Anufriev, Junki Nakagawa and Aymeric Ramiere, but also from other laboratories, especially from Hirakwa laboratory, who helped me to integrate in the new environment that is Japan, provided me with opportunities to practice my Japanese but were understanding when I had to switch to English. They created a very warm environment for me to enjoy my stay and conduct research in an efficient way. I particularly want to thank all the secretaries, from Nomura and Hirakawa laboratories as well as LIMMS, INL, the EEA doctoral school, Ecole Centrale Lyon and CNRS for the time they spent to help me with administrative paperwork and for all the help they provided for the PhD as well the procedures necessary due to my being in Japan; I also give my thanks to Miss Yumi Hirano and Nathalie Frances for their administrative help.

Naturally, I would like to thank my friends and family who renewed their support in favor of my stay in Japan despite my previous misfortune.

Last but not least, I would like to thank Iilari Maasilta and Olivier Bourgeois for accepting the role of reviewer for this thesis and to Sebastian Volz, Stefan Dilhaire and Karl Joulain for evaluating my work.

Résumé

Lors de deux dernières décennies, la nano-structuration a permis une augmentation conséquente des performances thermoélectriques. Bien qu'à l' origine le silicium (Si) ai une faible efficacité thermoélectrique, son efficacité sous forme de nanostructure, et notamment de nanofils, a provoqué un regain d'intérêt envers la conduction thermique au sein de ces nanostructures de Si. Bien que la conductivité thermique y ait été réduite de deux ordres de grandeur, les mécanismes de conduction thermique y demeurent flous. Une meilleure compréhension de ces mécanismes permettrait non seulement d'augmenter l'efficacité thermoélectrique mais aussi d'ouvrir la voie à un control des phonons thermiques, de manière similaire à ce qui se fait pour les photons. L'objectif de ce travail de thèse était donc de développer une plateforme de caractérisation, d'étudier le transport thermique au sein de différentes nanostructures de Si et enfin de mettre en exergue la contribution du transport cohérent de phonons à la conduction thermique.

Dans un premier temps, nous avons développé un système de mesure allant de pair avec une procédure de fabrication en salle blanche. La fabrication se déroule sur le site de l'institut de Sciences Industrielles et combine des manipulations chimiques, de la lithographie électronique, de la gravure plasma et du dépôt métallique. Le système de mesure est base sur la thermoreflectance : un changement de réflectivité d'un métal a une longueur d'onde particulière traduit un changement de température proportionnel.

Nous avons dans un premier temps étudié le transport thermique au sein de simples membranes suspendues, suivi par des nanofils, le tout étant en accord avec les valeurs obtenues dans la littérature. Le transport thermique au sein des nanofils est bien diffus, à l'exception de fils de moins de 4 µm de long a la température de 4 K ou un régime partiellement balistique apparait. Une étude similaire au sein de structures périodiques 1D a démontré l'impact de la géométrie et l'aspect partiellement spéculaire des réflexions de phonons a basse température. Une étude sur des cristaux phononiques (PnCs) 2D a ensuite montré que même si la conduction est dominée par le rapport surface sur vole (S/V), la distance inter-trous devient cruciale lorsqu'elle est suffisamment petite.

Enfin, il nous a été possible d'observer dans des PnCs 2D un ajustement de la conductivité thermique base entièrement sur la nature ondulatoire des phonons, réalisant par-là l'objectif de ce travail.

Mots-clés: Si, conductivité thermique, thermoreflectance, couches minces, nanofils, cristaux phononiques, cohérence.

Abstract

In the last two decades, nano-structuration has allowed thermoelectric efficiency to rise dramatically. Silicon (Si), originally a poor thermoelectric material, when scaled down, to form nanowires for example, has seen its efficiency improve enough to be accompanied by a renewed interest towards thermal transport in Si nanostructures. Although it is already possible to reduce thermal conductivity in Si nanostructures by nearly two orders of magnitude, thermal transport mechanisms remain unclear. A better understanding of these mechanisms could not only help to improve thermoelectric efficiency but also open up the path towards high-frequency thermal phonon control in similar ways that have been achieved with photons. The objective of this work was thus to develop a characterization platform, study thermal transport in various Si nanostructures, and ultimately highlight the contribution of the coherent phonon transport to thermal conductivity.

First, we developed an optical characterization system alongside the fabrication process. Fabrication of the structures is realized on-site in clean rooms, using a combination of wet processes, electron-beam lithography, plasma etching and metal deposition. The characterization system is based on the thermoreflectance principle: the change in reflectivity of a metal at a certain wavelength is linked to its change in temperature. Based on this, we built a system specifically designed to measure suspended nanostructures.

Then we studied the thermal properties of various kinds of nanostructures. Suspended unpatterned thin films served as a reference and were shown to be in good agreement with the literature as well as Si nanowires, in which thermal transport has been confirmed to be diffusive. Only at very low temperature and for short nanowires does a partially ballistic transport regime appear. While studying 1D periodic fishbone nanostructures, it was found that thermal conductivity could be adjusted by varying the shape which in turn impacts surface scattering. Furthermore, low temperature measurements confirmed once more the specularity of phonon scattering at the surfaces. Shifting the study towards 2D phononic crystals (PnCs), it was found that although thermal conductivity is mostly dominated by the surface-to-volume (S/V) ratio for most structures, when the limiting dimension, i.e. the inter-hole spacing, becomes small enough, thermal conductivity depends solely on this parameter, being independent of the S/V ratio.

Lastly, we were able to observe, at low temperature in 2D PnCs, i.e. arrays of holes, thermal conduction tuning based on the wave nature of phonons, thus achieving the objective of this work.

Keywords: Si, thermal conductivity, thermoreflectance, thin films, nanowires, phononic crystals, coherence.

Table of Contents

List of achievements

Peer-reviewed articles

- J. Maire and M. Nomura, “Reduced Thermal Conductivities of Si 1D periodic structure and Nanowires,” Jpn. J. of Appl. Phys, 53, 06JE09 (2014)

- R. Anufriev, J. Maire, and M. Nomura, “Reduction of thermal conductivity by surface scattering of phonons in periodic silicon nanostructures,” Phys. Rev. B 93, 045411 (2016).
- M. Nomura, Y. Kage, J. Nakagawa, T. Hori, J. Maire J. Shiomi, R. Anufriev, D. Moser, O. Paul, “Impeded thermal transport in Si multiscale hierarchical architectures with phononic crystal nanostructures,” Phys. Rev. B 91, 205422 (2015)
- M. Sakata, T. Hori, T. Oyake, J. Maire, M. Nomura, J. Shiomi, “Tuning thermal conductance across sintered silicon interface by local nanostructures,” Nano Energy 13, 601 (2015).
- M. Nomura, J. Nakagawa, Y. Kage, J. Maire, D. Moser, and O. Paul, “Thermal phonon transport in silicon nanowires and two-dimensional phononic crystal nanostructures,” Appl. Phys. Lett. 106, 143102 (2015).
- M. Sakata, T. Oyake, J. Maire, M. Nomura, E. Higurashi, and J. Shiomi, “Thermal conductance of silicon interfaces directly bonded by room-temperature surface activation,” Appl. Phys. Lett. 106, 081603 (2015).
- M. Nomura and J. Maire, “Towards heat conduction control by phononic nanostructures,” Thermal Science and Engineering, 53, 67-72 (2014)
- M. Nomura and J. Maire, “Mechanism of reduced thermal conduction in fishbone type Si phononic crystal nanostructures,” J. Electron. Mater. 44, 1426 (2014).

Articles in preparation

- J. Maire, R. Anufriev, H. Han, S. Volz, and Masahiro Nomura, “Thermal conductivity tuning by thermocrystals,” Arxiv (2015)
- J. Maire and Masahiro Nomura, “From diffusive to ballistic heat transport in Si nanowires,” in preparation

International conferences

- J. Maire, R. Anufriev, and M. Nomura, “Thermal conductivity tuning by disorder in Si phononic crystal,” Phonons 2015, UK, July (2015).
- J. Maire, T. Hori, J. Shiomi, and M. Nomura, “Thermal conductivity reduction mechanism in Si 1D phononic crystals at room temperature,” MRS Spring Meeting, San Francisco, April (2015).
- J. Maire and M. Nomura, "Thermal Conductivity in 1D and 2D Phononic Crystal Nanostructures," 2013 Material Research Society Fall meeting, BB10.09, Boston, USA, Dec. (2013).
- J. Maire and M. Nomura, "Reduced Thermal Conductivities of Si 1D Phononic Crystal and Nanowire", 26th International Microprocesses and Nanotechnology Conference, 6B-2-3, Sapporro, Japan, Nov. (2013).
- J. Maire and M. Nomura, "Reduced thermal conductivity in a 1D Si phononic crystal nanostructure," The 18th International Conference on Electron Dynamics in Semiconductors, Optoelectronics and nanostructures, TuP-30, Matsue, Japan, July (2013).

Japanese domestic conferences

- Maire Jeremie，Roman Anufriev and 野村政宏, “Thermal conduction control by phononic crystal nanostructures,” 第 76 回会応用物理学会秋季学術講演会，15p-2C-19，名古屋 (2015).
- Jeremie Maire, Takuma Hori, Junichiro Shiomi, Masahiro Nomura, “Thermal conductivity reduction mechanism in Si 1D phononic crystals at room temperature,” 第 62 回応用物理学会春季学術講演会, 12a-A22-3，神奈川 (2015).
- Maire Jeremie，野村政宏，“Temperature dependence of thermal conductivity for Si nanostructures,” 第 75 回会応用物理学会秋季学術講演会, 18p-A7-16，札幌(2014).
- Jeremie Maire，堀琢磨，塩見淳一郎，野村政宏“シリコン一次元周期ナノ構造における熱伝導率低減の起源に関する考察,” 第 61 回応用物理学会春季学術講演会, 19p-F11-10，青山学院大学，神奈川 (2014).
- Jeremie Maire、野村政宏“一次元Ｓｉフォノニック結晶ナノ構造の熱伝導率測定,” 第 74 回応用物理学会秋季学術講演会, 20p-C13-4，同志社大学，京都 (2013).

Author contributions

This work was supervised by Prof. Masahiro Nomura.

The candidate built and improved the optical measurement system. He wrote the Labview control program built the 3D FEM model used to extract the thermal conductivity presented in Chapter III. The candidate is also responsible for optimizing the fabrication process conditions.

All fabrication for nanowires and fishbone nanostructures presented in Chapter IV and 80 nm-thick 2D PnCs in Chapter V has been done by the candidate. Similarly, measurements and analysis for thin films, nanowires and fishbone structures were also performed by the candidate. The study on disorder, from fabrication to analysis, has also been done by the candidate.

The candidate also contributed to the measurement and analysis for the other 2D PnCs.

Monte-Carlo simulations were conducted by T. Hori from Shiomi laboratory, the University of Tokyo.

Thermal conductance calculations from the phonon dispersion have been done by R. Anufriev from Nomura laboratory, the University of Tokyo, who has also been the main contributor for the design, measurement and analysis of 2D PnCs of thickness 80 nm shown in section V.3.2.

145 nm-thick 2D PnCs presented in section V.3.1 have been studied by J. Nakagawa from Nomura laboratory, the University of Tokyo.

List of abbreviations

BTE	Boltzmann transport equation
RTA	Relaxation time approximation
MC	Monte-Carlo
FEM	Finite-element method
SEM	Scanning electron microscope
ICP	Inductively coupled plasma
RIE	Reactive ion etching
IPA	Isopropanol
HF	Hydrofluoric
EB	Electron-beam
TDTR	Time-domain thermoreflectance
DT	Decay time
RMS	Root-mean-square
PnC	Phononic crystal
MFP	Mean free path

List of abbreviations

Chapter I

Introduction

I.1 General introduction

I.2 Principle and efficiency of a thermoelectric device

I.3 Objective and realization of the work

I.4 Outline of the Thesis

I.1 General Introduction

Energy, but also environmental concerns, have become one of the most important issues over the past few decades. A considerable focus has been made over renewable energies, including solar energy, wind, and heat (among others). So far, the latter has been used mostly through solar thermal energy and geothermics, as a heating system for some individual houses, for example. Currently, photovoltaic energy is the most commonly used one, although it cannot provide all the energy necessary for an oil-free society alone. Moreover, given that energy use efficiency is far from perfect in any device, the part of energy used accounts for less than 50% of the energy provided, with the remaining being lost as wasted heat [1,2]. Therefore, re-using this wasted energy has become a major challenge, as illustrated in Figure I.1. Given that heat is a poor energy source, it needs to be transformed into electricity, which is more versatile and easily transported.

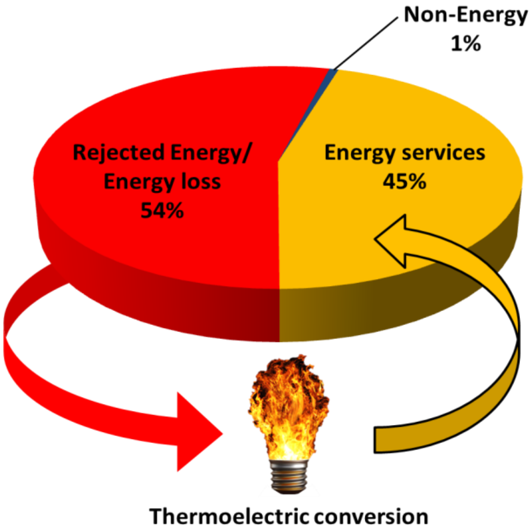

Figure I.1 Repartition of useful and waste energy in the world in 2007 [2].

Although the required efficiency for large scale commercial applications [3] has not been reached, thermoelectricity is expected to bring another evolution in our society of ever increasing connected objects. If it seems unrealistic to expect thermoelectric devices to output large quantities of energies from natural heat sources, it is however possible to power-up low energy electronic chips combined for example with wireless transmission modules. Such devices, equipped with both sensors and communications possibilities, could be deployed as grid sensors. For example, they could be used inside buildings structures to determine stress or the appearances of cracks due to time or earthquakes and thus prevent the fall of the building. It could be used to detect forest fires by being positioned regularly in sensitive areas. Many more usages are possible, but with current battery technologies, installing such sensor networks is not practical. With thermoelectricity, however, the lifetime of such devices would be greatly enhanced, rendering them viable and convenient as long-term monitoring tools.

I.2 Principle and efficiency of a thermoelectric device

The principle of a thermoelectric device, also known as a Peltier device, consists in the conversion of a temperature difference into electric current. In any material to which a temperature difference is applied, the charge carriers will tend to diffuse from the hot side the cold side, according to Kelvin law. Using two semiconductor branches, respectively n- and p-doped, linked together by an electrode on their hot side, electrons and holes, respectively, will diffuse in the same direction, creating a potential difference between the cold sides of both materials. This phenomenon, called the Seebeck effect, is the cause for the thermoelectric power generation. The principle is depicted in Figure I.2(a). It was first discovered in 1821 by Thomas Johann Seebeck, soon followed by the discovery of the opposite effect. In 1834, Jean Charles Athanase Peltier demonstrated the induction of a temperature difference by a current. It was soon shown that what is now called a Peltier device is reversible, i.e. a temperature difference can generate a current, and an input current can also generate a temperature difference.

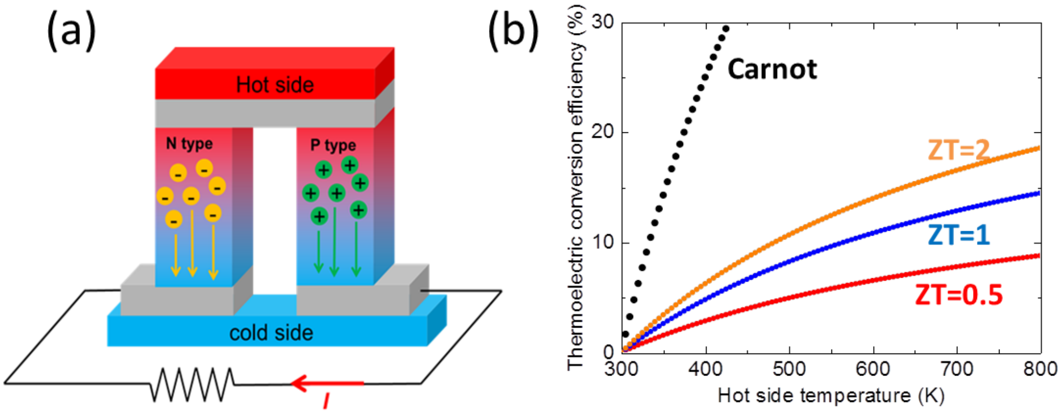

Figure I.2 (a) Principle of a thermoelectric device and (b) Thermoelectric conversion efficiency as a function of the hot side temperature, when the cold side is fixed at 300 K, for different values of ZT.

The common benchmark used to characterize the efficiency of a thermoelectric device is the thermoelectric figure of merit ZT given by:

$$\mathrm{ZT} = \frac{S^2\sigma}{\kappa}T \tag{1.1}$$

where S [$\mathrm{VK^{-1}}$] is the Seebeck coefficient, σ[1/Ωm] is the electrical conductivity and κ[$\mathrm{Wm^{-1}K^{-1}}$] is the thermal conductivity. This figure of merit appears in the global efficiency of a thermoelectric device, calculated as follow [4]:

$$\eta = \frac{T_h - T_c}{T_h} \cdot \frac{M_0 - 1}{M_0 + T_c/T_h} \tag{1.2}$$

where T_h and T_c are the temperatures on the hot and cold side respectively and M_0 is given by:

$$\mathrm{M}_0 = \sqrt{1 + Z(T_h + T_c)/2} \tag{1.3}$$

It is clear from these equations that the total efficiency of a thermoelectric device is dominated by two main parameters: (1) the difference in temperature between the hot and cold sides, and (2) the thermoelectric figure of merit. Both of them should be as large as possible. In Figure I.2(b), we plot the efficiency versus the difference in temperature for different values of ZT. We can see that, in order to reach an efficiency of 10% for a difference in temperature less than 100 K, it is necessary that ZT be clearly over 2.

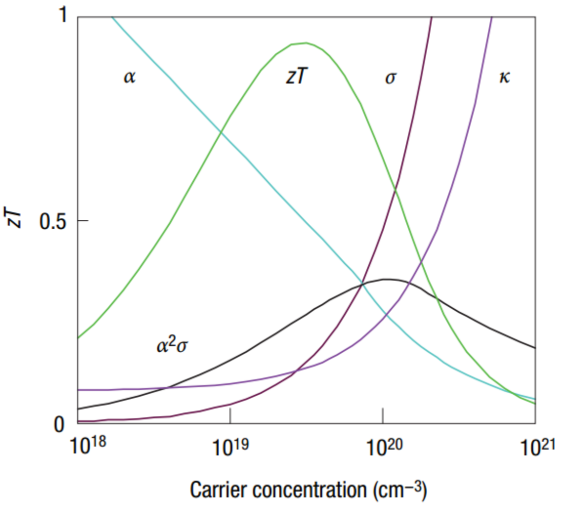

Figure I.3 Evolution of the Seebeck coefficient α (blue), the electrical conductivity σ (brown) and the thermal conductivity κ (violet), as well as the resulting power factor (black) and figure of merit (green) versus carrier concentration. The trends are extracted from the literature [5] and modelled for Bi_2Te_3.

In order to achieve such a high value, all parameters involved in the formula needs to be thoroughly optimized. However, the difficulty resides in the fact that they are inter-related. Figure I.3 provides a guide for the evolution of the different parameters versus the carrier concentration [5]. For example, it is usually not possible to independently tune both the electrical conductivity and the Seebeck coefficient [6]. They also evolve in the opposite direction when changing the carrier concentration. On the other hand, the thermal conductivity changes very little for small concentration and increases quickly above a certain value. From the expression of the figure of merit, it stands out that the power factor $S^2\sigma$ should be maximized while the thermal conductivity κ should be minimized.

Brief history of the thermoelectric figure of merit

After an increase in the figure of merit in the 1950s up to 1, this value remained nearly constant until the 1990s (Figure I.4). The most commonly considered material at room temperature for a high ZT is Bi_2Te_3 [7,8]. Carriers in this alloy have a very high mobility, while the heavy atoms with high mass anisotropy cause a very low thermal conductivity, down to 1.4 $W.m^{-1}.K^{-1}$ at room temperature. The combination of these two aspects makes this material one of the most efficient thermoelectric materials.

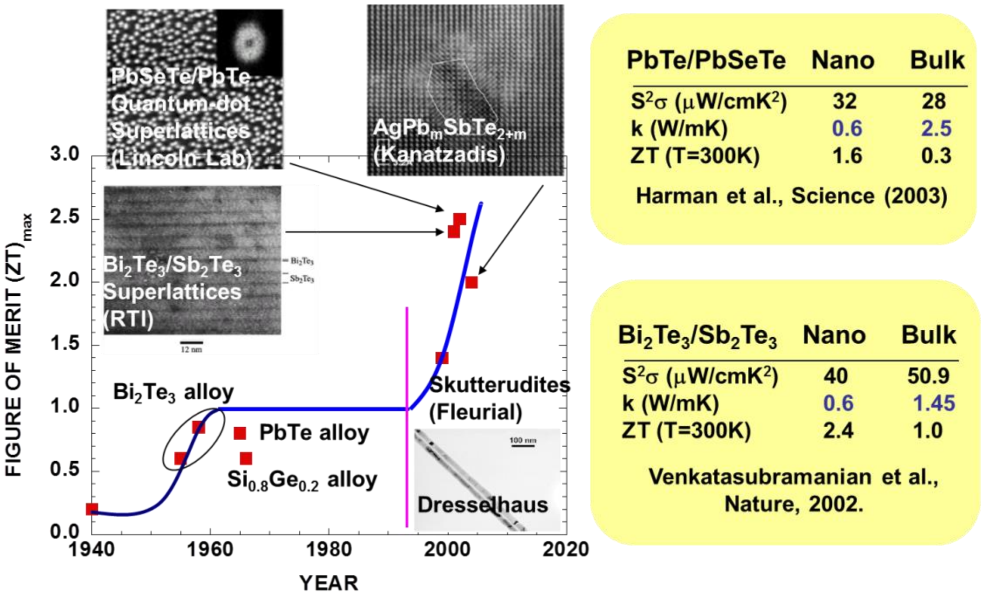

PbTe/PbSeTe	Nano	Bulk
$S^2\sigma$ ($\mu W/cmK^2$)	32	28
k (W/mK)	0.6	2.5
ZT (T=300K)	1.6	0.3

Harman et al., Science (2003)

Bi_2Te_3/Sb_2Te_3	Nano	Bulk
$S^2\sigma$ ($\mu W/cmK^2$)	40	50.9
k (W/mK)	0.6	1.45
ZT (T=300K)	2.4	1.0

Venkatasubramanian et al., Nature, 2002.

Figure I.4 History of the thermoelectric figure of merit [9].

In 1994, Slack *et al.* theorized the concept of “phonon glass electron crystal” [10] as the ideal form of a thermoelectric material. Phonon glass refers to the hindering of phonons by the structure of the material while electron crystal will facilitate carriers’ transport. According to the authors, it would be possible to increase ZT up to a value of 4 with nanostructures. Furthermore, they expect an increase in efficiency with the use of Skutterdites, which have been investigated since the 1970s [11]. The principle is that loosely bonded atoms will vibrate and further reduce the thermal conductivity.

At the same epoch, a pioneering work of Prof. Dresselhaus' group in MIT [12,13] reported the use of superlattice to achieve a higher figure of merit for small periods. In 2002, this led to the report of ZT=2.4 in a superlattice of Bi_2Te_3 and Sb_2Te_3 and an even higher ZT above 2.5 using a quantum dots superlattice. The principal reason behind this increased efficiency is the very low thermal conductivity. It has been reduced substantially due to phonon scatterers with sizes of a few nanometers. Given these small dimensions, heat carriers, i.e. phonons, are efficiently scattered by surfaces and their transport is thus greatly hindered, as will be detailed in the following chapter.

Thanks to the advances in micro- and nano-fabrication, it has become easier to study the impact of such small dimensions on heat transport. This applies not only to efficient thermoelectric materials such as Bi_2Te_3, but also to a wider range of materials, including previously poor thermoelectric materials such as Si and Germanium. This direction of research reached encouraging results, and a number of publications—on superlattices and nanowires at first—have emerged. More recently, periodic patterning has attracted much attention in order to control the heat flow with phononic crystals in similar ways as light with photonic crystals.

This renewed burst in micro- and nano-scale heat transport proves useful, not only for thermoelectric applications, but also for a variety of other applications, either direct ones like thermal coating, or indirect ones like thermal management in electronic and optoelectronic chips, or phase change memories, among many others. Contrary to thermoelectricity which requires the lowest possible heat conductivity, heat dissipation in electronic chips requires the opposite, i.e. a higher heat dissipation rate. In order to achieve any of these contradictory effects, a better understanding of transport mechanisms, at interfaces for instance, is required. Lastly, phonon transport represents just one aspect of a larger understanding about phonons, which include their generation, detection, and manipulation. While this field is lagging behind its photonic counterpart, where effects such as cloaking [14], confinement [15,16], slow light [17], or guiding [18] have already been achieved, a strong research effort in this direction offers interesting prospects.

I.3 Objective and realization of the work

The project this work is part of ultimately aims at the development of Si thermoelectrics and Si phononic devices. Here, our purpose is to better understand heat conduction and, more specifically, thermal phonon transport in Si nanostructures. Si presents several advantages, such as its low cost and abundance. Also, its toxicity compared to heavy materials incorporating Pb, Bi or Te is negligible. Lastly, Si is a well-known material, which makes nanoscale fabrication all the more accessible, thanks to already well documented processes. The interest of nanostructures resides in the novel properties they display. This has been extensively proven (initially with light). Nowadays a great number of photonic devices make use of these particular properties to display novel effects such as slow light, cloacking, confinement, or 3D photonic guiding. When it comes to phonon transport, some similar effects have been achieved at low frequencies, i.e. up to the range of a few MHz [19–22]. Thermal phonon transport, however, poses two major challenges to achieve this level of control: (i) the high frequencies involved, i.e. up to a few THz, with their associated small wavelengths, and (ii) the very wide range of frequencies occupied by thermal phonons. In order to reach these applications, as well as more efficient thermoelectric devices, it is first crucial to have a deeper understanding of precise thermal transport mechanisms in nanostructures. We can then develop structures which make use of the wave properties of thermal phonons.

In order to study heat transport in Si nanostructures, we developed a complete fabrication, measurement, and analysis ecosystem. The fabrication is done in clean room on-site at the Institute of Industrial Science, the University of Tokyo. Most of the equipment was already present and accessible upon specific training, from manipulation of chemicals to the use of electron-beam lithography, metal deposition, and plasma etching systems. The last step, i.e. release of the suspended structure, was optimized with inspiration from colleagues from the same Institute [23]. The characterization system was entirely developed during the course of this work. The requirements were a system fast enough to allow for the measurements of a vast number of structures with accuracy in the norm for such measurements. Furthermore, it was necessary to have the possibility to vary the temperature over a temperature range as wide as possible, especially towards low temperatures. The optical measurement system was designed and built by adapting the thermoreflectance measurement method for our needs. The Labview program was developed to automatize measurement as much as possible, as well as accelerate and facilitate the subsequent analysis. We also developed the model in COMSOL to extract the thermal conductivity from the thermal decay curves produced by the measurement system. Both the fabrication method and the measurement system are detailed in chapter III.

Upon developing these aspects, we studied simple structures such as membranes and nanowires in order to ascertain the reliability of the measurement and analysis. Then, the work revolved around two main ideas. The first one was to diminish thermal conductivity at room temperature in various kinds of Si nanostructures. This reduction stems mainly from incoherent scattering processes due to the nanoscale nature of the structures. The second one was to clearly demonstrate the influence of coherent thermal phonon transport on the thermal conductivity in Si nanostructures. Due to the characteristic length scales involved, this is expected to arise mostly at cryogenic temperatures. We thus designed periodic nanostructures called phononic crystals (PnC). These PnCs display wave properties that greatly vary from the simple thin film or nanowires, which proves convenient to show the appearance of wave effects. From this study, we report the first demonstration of thermal conduction tuning by PnCs using the wave nature of phonons at 4K.

I.4 Outline of the Thesis

This work is organized as follows.

In Chapter II, we present a general approach towards phonon transport in Si, based on the Boltzmann transport equation, followed by thermal conductivity models, including a discussion about the different scattering mechanisms. Then we provide the descriptions of Monte-Carlo (MC) simulations that were used to support our experiments. Finally, we show a method to calculate the thermal conductance based on the elasticity theory, i.e. the wave properties of phonons.

In Chapter III, we detail the steps necessary for the fabrication process in the order they are performed. Then, after introducing the time-domain thermoreflectance (TDTR) method, we explain our implementation of this technique, including the Labview acquisition program and the FEM simulations used to extract the thermal conductivity.

In Chapter IV, we focus on thermal conductivity measurements in simple thin films, followed by nanowires and fishbone periodic nanostructures. Data is presented between 4 K and room temperature and results are compared to available data in the literature.

In Chapter V, after a brief review of 2D phononic crystals in the literature, we present results of thermal conductivity measurements in 2D PnCs, starting from the particle picture. This specific study aims at clarifying the impact of the shape, i.e. lattice type and hole size, on thermal conductivity at room temperature and 4 K. Lastly, we demonstrate thermal conductivity tuning by disorder in 2D PnCs, in the wave regime.

Chapter II

Theory of thermal phonon transport in Si

In this chapter, we present an insight into nanoscale thermal conduction mechanisms in semiconductors, and more specifically in Si. In the first section, we will present the most common approach to the estimation of the thermal conductivity, namely the Boltzmann transport equation, associated with the relaxation time approximation that allows for estimations of the relative importance of each phonon scattering mechanism. Then, we detail two types of simulations that have been used to complement our experiments. The first type consists in a ray tracing simulation using the MC method which is based on phonons being considered as particles. The second one is the computation of the phonon dispersion and extraction of the transport properties in the wave regime, leading to the thermal conductance.

In semiconductors, thermal conductivity can be split in two contributions as follow:

$$\kappa_{tot} = \kappa_{el} + \kappa_{l} \tag{2.1}$$

where κ_{el} is the electronic contribution to the thermal conductivity and κ_{l} the lattice thermal conductivity. Due to the semiconductor nature of Si, the electronic contribution tends to disappear at lower temperatures or lower doping densities, hence the focus on the lattice thermal conductivity in this work.

II.1 Lattice thermal conductivity

Lattice thermal conduction is dominant for most undoped semiconductors in the temperature range considered here, i.e. below 300 K. In the crystal lattice, atoms vibrate around their thermal equilibrium position, coupled with neighboring atoms. This common vibration can be characterized by standing waves at equilibrium. The quantum of vibration of the lattice is called a “phonon” and a temperature difference will induce propagation of these modes in a privileged direction. The energy of a phonon is given by $\mathrm{E} = \hbar\omega = h\nu/\lambda$ with $\hbar$ the Planck constant, ω the angular frequency, ν the propagation speed and λ the corresponding wavelength.

Dispersion relation of phonons for simple atomic structures consists of acoustic (in-phase) and optical (out-of-phase) “branches”. Often, optical phonons, with high frequencies, contribute very little to thermal transport [24], except in their interactions with acoustic phonons. Indeed, at low temperatures, i.e. below room temperature, the system does not reach high enough frequencies to excite the optical modes. Moreover, even at higher frequencies, optical phonons have very low group velocities, in addition to being only lightly populated. These two parameters make their contribution to thermal transport usually negligible, although following equations will be given in the general case, including both acoustic and optical modes.

Since phonons are bosons, they follow the Bose-Einstein distribution, we can write the distribution function for any given wavevector $\vec{k}$, at equilibrium, with the formula:

$$f_{\vec{k}\,eq} = \frac{1}{\exp\left({\hbar\omega_{\vec{k}}}/{k_B T}\right) - 1} \tag{2.2}$$

where k_B is the Boltzmann constant, $\omega_{\vec{k}}$ the frequency of a phonon of wavevector $\vec{k}$ and T the temperature.

Our main parameter of interest, i.e. the thermal conductivity κ, is usually calculated by solving the Boltzmann transport equation (BTE). The assumption most often made is the relaxation time approximation (RTA). In the BTE, any deviation from the equilibrium distribution will be "corrected" by the scattering mechanisms. The general form of the BTE is given by:

$$\frac{\partial f_{\vec{k}}}{\partial \mathrm{t}} + \overrightarrow{\mathrm{v}_g}.\vec{\nabla} f_{\vec{k}} = \left(\frac{\partial f_{\vec{k}}}{\partial \mathrm{t}}\right)_{collision} \tag{2.3}$$

with v_g the group velocity. The RTA provides further simplifications under the assumption that perturbations from equilibrium are small, i.e. local equilibrium:

$$\frac{\mathrm{f}_{\vec{k}} - f_{\vec{k}\,eq}}{\tau_{\vec{k}}} = -(\overrightarrow{\mathrm{v}_g} \cdot \vec{\nabla}\mathrm{T})\frac{\partial f_{\vec{k}\,eq}}{\partial \mathrm{T}} \tag{2.4}$$

with $\tau_{\vec{k}}$ a realaxation time for collisions, or also lifetime of the particle and $\overrightarrow{\mathrm{v}_g} \cdot \vec{\nabla}\mathrm{T}$ denotes the particle velocity along the temperature gradient.

The heat flux due to one phonon mode is the product of its speed by its energy, the total heat flux is their sum over all modes multiplied by their occupation. Since the thermal conductivity is the heat flux divided by the temperature gradient, we can obtain an expression for the thermal conductivity. However, rather than solving the thermal conductivity for the precise phonon spectrum, in this section we use the Debye approximation of phonon dispersion, i.e. $\omega = v\vec{k}$, and assume isotropic group velocities. After all simplifications are carried out, the resulting expression for the thermal conductivity is:

$$\kappa = \frac{1}{3}\int_{0}^{\omega_{\mathrm{D}}} \tau_\omega \, {v_\omega}^2 \hbar\omega \frac{\partial \mathrm{f}(\omega, \mathrm{T})}{\partial \mathrm{T}} \, D(\omega) d\omega \qquad (2.5)$$

with $D(\omega)$ the density of states and $\omega_{\mathrm{D}} = 6\pi^2 v^3 N/V$ the Debye cutoff frequency where N is the number of atoms in the specimen and V its volume.

Or, using the heat capacity [25,26], and posing $\mathrm{x} = \hbar\omega/k_B T$:

$$\kappa = \frac{1}{3}\int_{0}^{x_{\mathrm{D}}} C_{ph}(x) v_x \, \Lambda_x dx \qquad (2.6)$$

with Λ the phonon mean free path (MFP) and the heat capacity being:

$$C_{ph} = \frac{9\mathrm{N}k_B T}{{x_{\mathrm{D}}}^3}\int_{0}^{x_{\mathrm{D}}} \frac{x^4 e^x}{(e^x - 1)^2} dx \qquad (2.7)$$

This formula is part of the Debye theory, which is usually used at low temperature, i.e. $\mathrm{T} < \theta_D$, where θ_D is the Debye temperature and equals 640 K for Si. While it can still be used at room temperature, Einstein model provides a better fit to experimental results, in which the heat capacity is given by:

$$C_{ph} = \frac{3\mathrm{N}\hbar^2\omega^2}{k_B \mathrm{T}^2} \frac{e^x}{(e^x - 1)^2} \qquad (2.8)$$

To obtain an accurate estimate it is thus necessary to have a precise knowledge of the heat capacity, the scattering rates, but also parameters extracted from the band diagram, such as frequencies and velocities. In the next section, the different scattering mechanisms and some thermal conductivity models will be detailed, as well as their range of application.

II.2 Models for the relaxation times of phonons

The relaxation time is an important parameter that enters in the thermal conductivity expression, as shown in the previous section. Its value is dependent on the system studied, but also on the temperature and the frequencies of phonons of interest. In order to simplify its estimation, three categories are considered to account for most of the scattering: point defect scattering (isotopes and impurities), boundary scattering (especially important in case of small systems, i.e. which dimensions are comparable to the phonon MFPs), and phonon-phonon scatterings (Umklapp and normal processes).

Boundary scattering refers to any scattering occurring at either a free surface or an interface between materials. Grain boundaries are another example of efficient phonon scatterers as mentioned in more detail in the conclusion. The three phonon normal process is shown in Figure II.1(a): Two phonons of wavevectors k_1 and k_2 result in a third phonon of wavevector k_3 with $k_1 + k_2 \rightarrow k_3$. It is also possible to observe the opposite occurrence, i.e. $k_3 \rightarrow k_1 + k_2$.

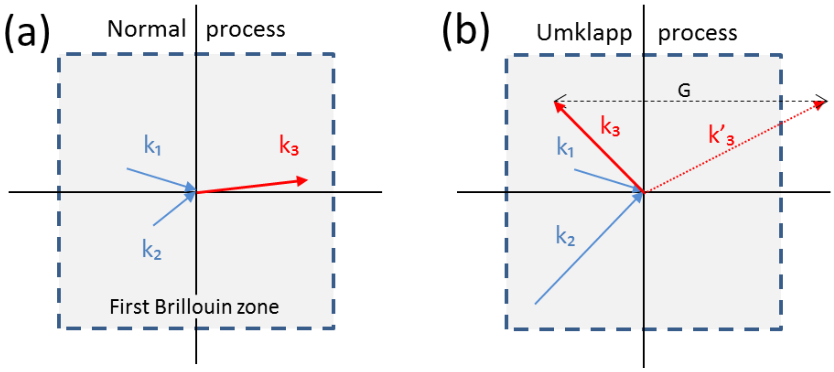

Figure II.1 Schematic representation of (a) the Normal scattering process (N- Process) and (b) the Umklapp scattering process (U-Process) in the reciprocal space.

Umklapp scattering can be seen as a particular case of a three phonon process. The specificity is that the resulting k'_3 wavevector points out of the Brillouin zone, which is equivalent, by addition of a reciprocal lattice vector G, to a wavevector inside the first Brillouin zone (Figure II.1(b)). Thus, contrary to normal processes that conserve momentum, Umklapp scattering change the total phonon momentum.

All scattering phenomena have separate relaxation times linked by the universally used Matthiessen's rule:

$$\frac{1}{\tau} = \sum_i \frac{1}{\tau_i} \tag{2.9}$$

where each τ_i corresponds to a specific relaxation time determined for each mechanism and τ is the overall relaxation time. Especially in low dimension anisotropic systems, each relaxation time is wavevector dependent. In this case, an average value over the wavevectors is often taken to simplify the calculation process. In order to make realistic calculations, some assumptions also need to be made over relaxation times or phonon band properties. A few widely used models have historically been developed around these assumptions and the three most widely used are briefly presented here.

II.2.1 Klemens model

Historically one of the first detailed model taking different expressions for different scattering mechanisms, the Klemens model's [27,28] specificity is to calculate separately the thermal conductivities for each scattering mechanism. The contributions are summed up as:

$$\frac{1}{\kappa_l} = \sum_i \frac{1}{\kappa_i} \tag{2.10}$$

with each κ_i a thermal conductivity associated with a specific scattering mechanism. Klemens was the first to give a point-defect scattering rate for defects smaller than the incident phonon wavelengths as:

$$\tau_D^{-1} = \frac{V}{4\pi v^3}\omega^4 \sum_i f_i \left(\frac{\overline{\mathrm{m}} - \mathrm{m}_i}{\overline{\mathrm{m}}}\right)^2 \tag{2.11}$$

where $\overline{\mathrm{m}}$ is the average mass of all atoms, m_i is the mass of an atom of fraction f_i and V is the volume per atom. This is often simplified with: $\tau_D^{-1} = \mathrm{A}\omega^4$. This equation has later been modified by Abeles [29].

The expression for the Umklapp process is given by:

$$\tau_U^{-1} = B_{\mathrm{U}} T^3 \omega^{\mathrm{n}} \exp(-\,\theta_D/\mathrm{mT}) \tag{2.12}$$

with B_{U} a constant, n and m constants with n=1 or 2. This expression is given for low temperatures while the expression at higher temperatures is given by:

$$\tau_U^{-1} = \mathrm{B'T}\omega^2 \tag{2.13}$$

with B' a constant. All B's in this section denote constants.

In this model, an estimate for the normal process scattering rate is given by: $\tau_N^{-1} \propto T^3\omega^2$. However, since the momentum is conserved, it cannot be directly summed with the other processes mentioned here, such as isotope scattering, Umklapp process or boundary scattering.

II.2.2 Callaway model

The Callaway model [30] was developed in 1959 to express thermal conductivity at low temperatures (below 100 K). The phonon spectrum assumes a Debye-like distribution without distinction between longitudinal and transverse phonons. The phonon branches are also considered non-dispersive like in the Klemens model. The different scattering rates are described in the following subsections.

II.2.2.1 Point defect scattering:

This scattering takes the same form as in the Klemens model. The phonons velocity is an averaged value over longitudinal and transverse branches. Since the phonon spectrum is Debye-like, this expression is valid only for T<<θ_D. For Si, θ_D = 640 K so the expression is valid at low temperatures.

II.2.2.2 Boundary scattering:

The expression of the boundary scattering is here given by:

$$\tau_B^{-1} = v_B / L_0 \tag{2.14}$$

where v_B is the average velocity and L_0 the characteristic length of the sample.

Here the scattering is considered purely diffusive and is the same for the other models presented here. Further discussion on the diffusive/specular scattering will be developed in the next section.

II.2.2.3 Three phonon normal process:

In the Callaway model, the normal process has a similar expression as in the Klemens model:

$$\tau_N^{-1} = B\omega^a T^b \tag{2.15}$$

where B is a constant independent of ω and T and (a;b) is a couple of constant chosen to fit experimental data, depending on the materials under investigation. For group IV and group III-V semiconductors, commonly accepted values are (a;b) = (1;4) and (2;3) [30,31], respectively.

II.2.2.4 Umklapp scattering:

The expression for the Umklapp scattering was given by Peierls as:

$$\tau_U^{-1} = B_1 T^n \omega^2 \tag{2.16}$$

with B_1 a fitting parameter containing $\exp(-\theta_D/\mathrm{mT})$, where m and n are constants used to fit experimental data. This expression is also only valid for low temperatures, where Umklapp scattering has little effect, thus again limiting the whole model to the low temperature range, i.e. $T \ll \theta_D$.

II.2.3 Holland model

The Holland model [32] is very similar to the Callaway model with one major difference: the longitudinal and transverse phonons are considered to have separate contributions and the model attempts to describe higher temperatures, with $T > 0.1 \cdot \theta_D$. The main differences compared to the previous models are found in the expression of the normal process and Umklapp scattering.

II.2.3.1 Three phonon normal process:

Here the two expressions chosen for transverse and longitudinal are similar to the Callaway model. For high temperatures, the expressions used are also derived from Herring [33]:

$$\tau_{N,T}^{-1} = B_T \omega T \tag{2.17}$$

$$\tau_{N,L}^{-1} = B_L \omega^2 T \tag{2.18}$$

Comparing the expression at lower and higher temperatures, we can notice that at high temperatures, the temperature dependence becomes smaller. It is also worth noting that the impact of normal processes is less critical than that of Umklapp process since normal process conserve the total momentum. This is all the more true at higher temperatures, where the impact of Umklapp processes keeps on increasing.

II.2.3.2 Umklapp scattering:

In this model, Umklapp scattering possess different expressions for longitudinal and transverse modes. While the expression for the longitudinal modes can be taken from the previous models, the expression for transverse modes is given by:

$$\tau_{U,T}^{-1} = \frac{B_{U,T}\omega^2}{\sinh\left(\frac{\hbar\omega}{k_B T}\right)} \tag{2.19}$$

Taking into account these different expressions for the scattering times and their temperature of effect, it is possible to get back to a general shape of the thermal conductivity from low to higher temperatures, as depicted in the following Figure II.2:

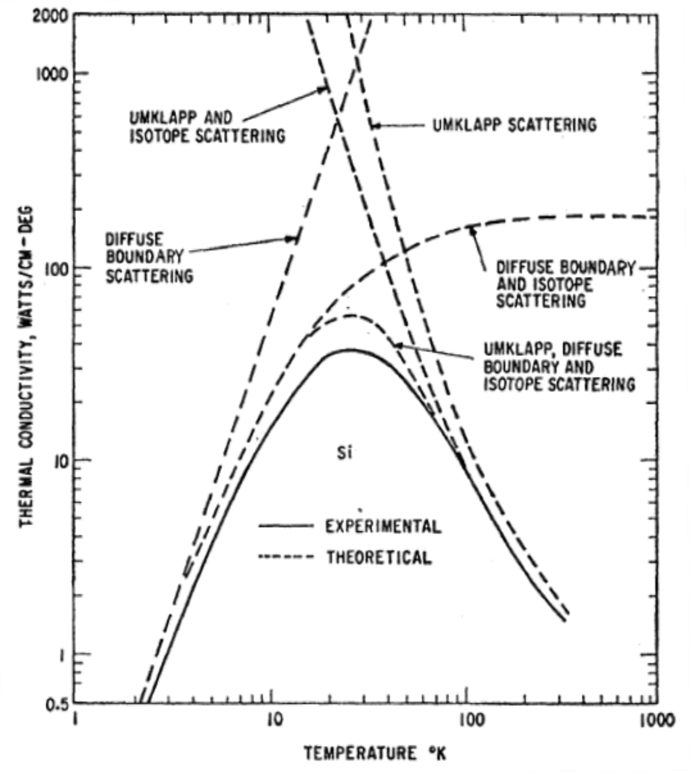

Figure II.2 Comparison of the temperature-dependent thermal conductivity of Si between experiment and simulation [34].

This approach provides a good description of the thermal transport phenomenon, and has been further refined by combining or modifying parts of these models. A specific method often used to solve the BTE is described in the following section: from first principle calculation to get the atomic force constants, to MC based simulations to eventually get back to the heat flux.

II.3 Monte Carlo simulations

The statistical Monte-Carlo method is one of the most common methods to compute the thermal conduction models presented in the previous sections, i.e. solving the BTE under the relaxation time approximation for instance. Here, MC simulations consist in solving the BTE in the frequency dependent relaxation time approximation. The transport equation is written as:

$$\frac{\partial \mathrm{f}}{\partial \mathrm{t}} + V_g \times \nabla f = -\frac{f - f_{eq}}{\tau} \tag{2.20}$$

However, in order to perform this simulation, some parameters need to be calculated beforehand, requiring other calculation methods. The succession of simulation procedures, from initial parameters to the thermal conductivity is summarized in Figure II.3.

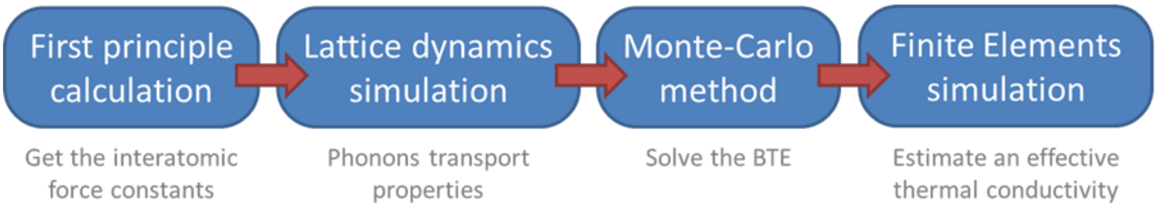

Figure II.3 Flowchart of the simulation.

In the following subsections we provide a brief description of the calculation steps and their purpose.

II.3.1 First principle calculation

The purpose of the first-principle calculation is to obtain the inter-atomic force constants [35]. First, the potential energy is constructed as a Taylor expansion in atoms displacements around their equilibrium position that can be described by:

$$\begin{aligned} \mathrm{V} = \mathrm{V}_0 + \sum_i \Pi_i u_i + \frac{1}{2!}\sum_{ij} \Phi_{ij} u_i u_j + \frac{1}{3!}\sum_{ijk} \Psi_{ijk} u_i u_j u_k \\ + \frac{1}{4!}\sum_{ijkl} X_{ijkl} u_i u_j u_k u_l \end{aligned} \tag{2.21}$$

with Π, Φ, Ψ, X, the interatomic force constants of the 1st to 4th order respectively and u_i the displacement of atoms. Since we consider that the atoms are usually around the equilibrium position, the Π_i are usually null. As can be seen from this equation, depending on the order of the force constant, it is required to consider a certain number of atoms' impact on their neighbors. Thus, in a supercell with its atoms in their equilibrium position, a few neighboring atoms are slightly displaced around this equilibrium position and the impact on a single atom of interest is studied. The displacement here is on the order of 0.01 Å and for first, second and third order force constants, 1, 2 and 3 atoms are moved respectively.

II.3.2 Lattice dynamics simulation

The purpose of this step is to calculate the phonon transport properties of the bulk in the material of interest, which are required both for the MC simulations as well as for calculating the phonon MFPs. Since the phonon dispersion relation is well known for Si, lattice dynamics (LD) simulations allow this dispersion to be plotted and then compared to experimental results. It is then possible to extract the frequency dependent heat capacity as well as the group velocity. The last parameters extracted from the simulation are the relaxation times of phonons that will also be later used in the MC simulations.

The LD simulation consists in forming a dynamical matrix of the crystal, i.e. a matrix of the force constants in the reciprocal space. Once diagonalized, its eigenvectors result in the phonon normal modes. It is then possible, from these modes as well as the cubic force constants [36–38], to calculate the phonon lifetimes. With them, solving the BTE under the relaxation time approximation leads to the thermal conductivity for bulk, whereas for nanostructures it is necessary to implement the geometry in order to get an accurate representation of the surface scattering.

II.3.3 Monte-Carlo simulation

The Monte-Carlo method is used to solve the Boltzmann transport equation, using the transport properties calculated previously from the lattice dynamics simulation. This solving has been described in more detail in the review by Peraud *et al.* [39]. Taking a unit cell as depicted in Figure II.4, the temperature on both ends is fixed. On the hot side (heat generation side), it is fixed slightly higher than the equilibrium temperature, while on the cold side (heat sink), the temperature is put slightly lower than the equilibrium temperature. Since the MC method is a stochastic method, a great number of phonons are input and it is possible, after reaching equilibrium, to obtain the lifetimes for the different scattering mechanisms, but especially boundary scattering, as well as the MFP of phonons.

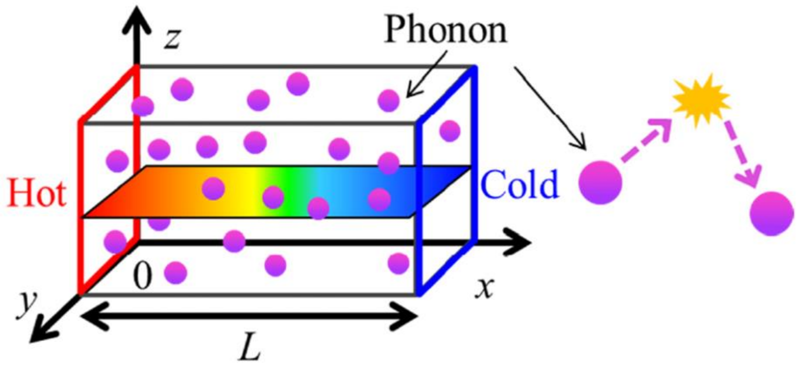

Figure II.4 Schematic diagram of the Monte-Carlo simulation unit cell. The heat flux is determined by the boundary conditions. Scattering events are calculated within the simulation domain.

The Boltzmann transport equation is solved under the RTA and since the computation in wavenumber would be computationally too heavy, it is done in terms of frequencies. The computation is performed in a unit cell as presented in Figure II.4, calculating the time evolution of phonons combining natural advection and scattering mechanisms. Then, it is possible to calculate the heat flux with:

$$\mathrm{q} = \frac{1}{\mathrm{V}\Delta\mathrm{t}} \sum_{all} \hbar\omega (x_{t+\Delta \mathrm{t}} - x_t) \tag{2.22}$$

with V the volume of the simulation cell and x_t the position of a phonon at time t. The summation is done over all phonons in the cell. Once the heat flux is calculated, it is possible to use a FEM model in COMSOL Multiphysics to get back to the thermal conductivity. The simulations are very similar to extracting the thermal conductivity from the thermal decay time, which is presented in detail in Chapter III, except that the parameter to be fitted is the heat flux and not the thermal decay time.

Boundary scattering in MC simulations

Boundary scattering is one of the most important scattering mechanisms in nanostructures, even at high temperatures. In this section, we introduce the notion of specularity in the boundary scattering process.

If the characteristic size of the surface roughness is small enough compared to the phonon wavelength, it is possible to see the appearance of specular reflection, which is a momentum-conserving reflection. Using the Debye theory, it is possible to calculate the total energy contained in the crystal, and extract the density of energy per unit volume and interval of frequency. The result is shown in Figure II.5 and described by the equation:

$$\mathrm{B(x)} = \frac{3\hbar}{2\pi^2 {v_D}^3} \frac{\omega^3}{e^x - 1} = \mathrm{A}\frac{x^3}{e^x - 1} \tag{2.23}$$

with the same notations as before and v_D the Debye sound velocity.

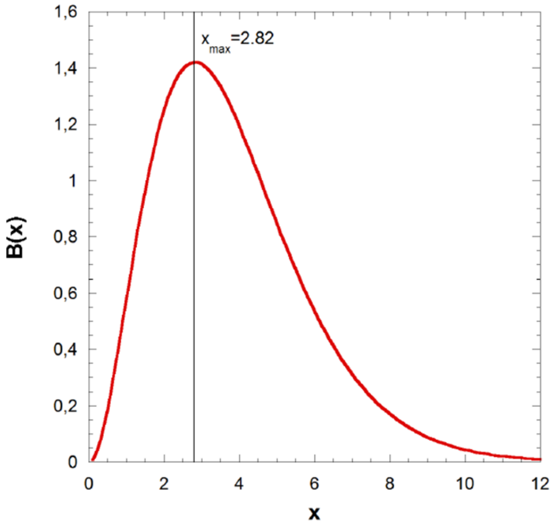

Figure II.5 Planck’s law for phonons

By performing a derivation of this function and nullify the resulting expression, it is possible to find a numerical approximation of its maximum, which we take as the dominant wavelength. It can be expressed as:

$$\lambda_d = \frac{h v_g}{\alpha k_B T} \tag{2.24}$$

where λ_d is the dominant phonon wavelength, h is the Planck constant and α is a parameter to account for the shape of the Planck distribution. The dominant wavelength can also be considered at other points on this curve, such as the average value of the distribution or the root mean square. Depending on this choice, the value of x associated with the dominant wavelength, and consequently the α parameter, will be different. Here we consider the value at the maximum of the distribution and thus, $\alpha = 2.82$.

The dominant wavelength calculated this way at 4 K is 25.5 nm, well above its value at room temperature. Figure II.6 provides a representation of the dominant wavelength at low temperature, showing its quick decrease with temperature.

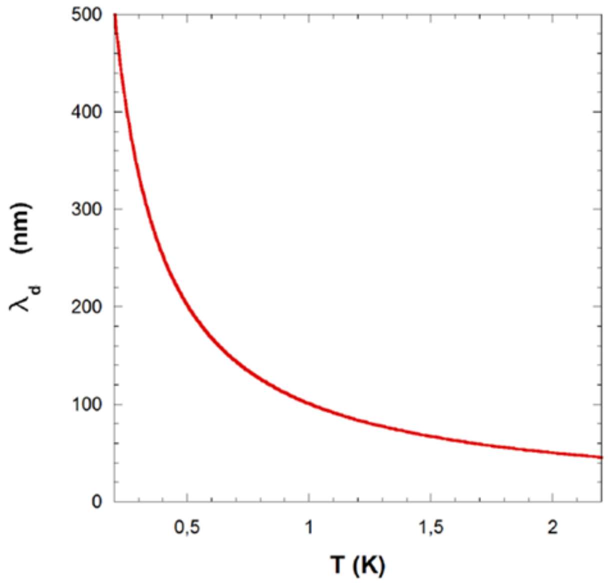

Figure II.6 Dominant wavelength as a function of temperature calculated from Eq. 2.24.

To estimate the proportion of specular reflection, we calculate the specularity parameter *p* which is given by Soffer's formula [40]:

$$p = e^{\frac{-16\pi^2\eta^2}{\lambda^2}cos^2(\psi)} \tag{2.25}$$

where η is the characteristic roughness, λ the phonon wavelength and ψ the incident angle. This equation is a generalization of Ziman's formula for different incident angles. For p = 0 scattering will be purely diffusive while for p = 1 it will be purely specular. Although in the models presented previously, the expression for boundary scattering was frequency-independent, it is clear from the formula of the specularity parameter that phonons with different frequencies will behave very differently when encountering an interface, thus the frequency-dependent approach used in the MC simulations. Since we already know the Planck distribution for phonons, it is possible to calculate this specularity parameter for various wavelengths at each temperature, as plotted in Figure II.7. In this case, the roughness is chosen to be ±2 nm, which is reasonable in terms of fabrication. At each temperature, the dominant wavelength is calculated, from which the specularity parameter is computed. The specularity calculation is repeated for 2 other wavelengths chosen to be half of the dominant wavelength and double this same dominant wavelength. Since the dominant wavelength is temperature dependent (see Eq. 2.24), so are the other two wavelengths selected. From this curve, it is evident that most phonons will be purely diffusive around room temperature, i.e. whatever the wavelength considered, the specularity parameter is nearly null. At 4 K however, a non-negligible part of the phonon distribution is partly specular. As shown in Figure II.7, the **s**pecularity parameter, while very small for a wavelength half that of the dominant wavelength of 25.53 nm, is equal to 0.38 at 4 K for the average value of $cos^2\theta$ over all possible incident angles. Still, the scattering is expected to be mainly diffusive for this wavelength. However, for slightly longer wavelengths the specularity parameter goes up exponentially and for a wavelength of 50 nm, which equals twice that of the dominant one, p=0.78 which denotes a highly specular scattering regime. This shows that although phonon transport is not purely specular over the whole spectrum, partially ballistic transport can be achieved at low temperatures, i.e. part of the phonon spectrum with long wavelengths will be ballistic.

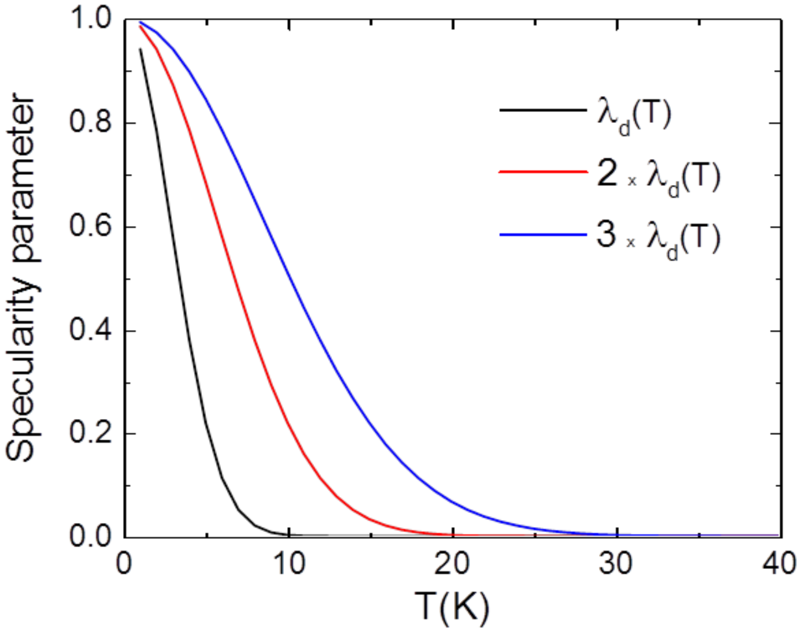

Figure II.7 Specularity parameter as a function of temperature for three different wavelengths: the dominant wavelength (black) and its double (red) and triple (blue).

II.4 Phonon wave properties

The previous section was dedicated to the Boltzmann approach to thermal transport. If this model proves efficient in explaining most experimental results, it is however not complete. Indeed, phonons are intrinsically lattice vibrations, i.e. waves. Although their wave behavior involves very short length scales on the order of nanometers, a model of their wave properties is required to depict some deviations from the particle model. Especially at low temperatures, it was proven that the wave properties of phonon could impact thermal transport substantially [41].

II.4.1 Phonon band diagram

In the low temperature limit, when the coherence length of phonons is sufficiently large compared to the characteristic length of the structure, i.e. the period, a phonon can be considered as an elastic wave, and it is relevant to describe the phonon transport with the classical theory of elasticity.

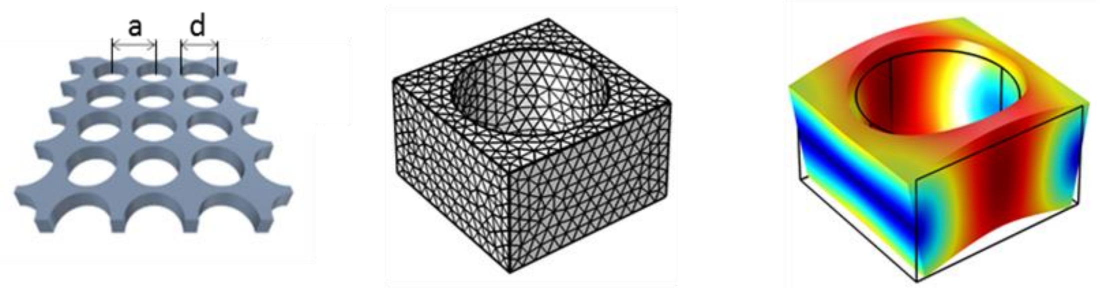

Figure II.8 Schematic of a simulated periodic structure (left) with its unit cells demonstrating the mesh (center) and displacement fields (right) in one of the solutions. a represents the period and d the diameter of the holes.

In the framework of this theory, the phonon dispersion relation (also called band diagram) can be obtained by means of the commercial software COMSOL Multiphysics®. The software solves the linear elastic wave equation:

$$\xi\nabla^2\boldsymbol{u} + (\xi+\gamma)\nabla(\nabla\cdot\boldsymbol{u}) = -\rho\omega^2\boldsymbol{u} \qquad (2.26)$$

where **u** is the displacement vector, ρ is the mass density and γ and ξ are the Lame parameters. Both these parameters appear in the stress-strain relationships or in the bulk modulus definition and are material-dependent. ξ is also being called the shear modulus while γ has no physical interpretation and is just used to simplify the stiffness matrix. It can be expressed as a function of the Young modulus E and Poisson coefficient ν with the relation: $\gamma = E\nu/(1+\nu)(1-2\nu)$. Solving the elastic wave equation in a unit cell (Figure II.8) with periodic Floquet boundary conditions, we can obtain the dispersion relation for the infinite periodic structure. Floquet boundary conditions are periodic of the form $\mathrm{u}(\mathrm{r}_0 + \mathrm{r}) = \mathrm{u}(\mathrm{r}_0)\exp\left(-\mathrm{i}\vec{\mathrm{k}}\,.\,\vec{\mathrm{r}}\right)$ with $\vec{\mathrm{k}}$ the wavevector, r_0 the initial position and r the distance between source and the point under consideration. This equation implies a phase shift depending on the distance and direction between two points under consideration. Once the solutions over the entire first Brillion zone (Figure II.9(a)) are obtained (Figure II.9(b,c)), we can calculate the spectra of phonon group velocity, density of states and the heat flux [42] as well as the thermal conductance.

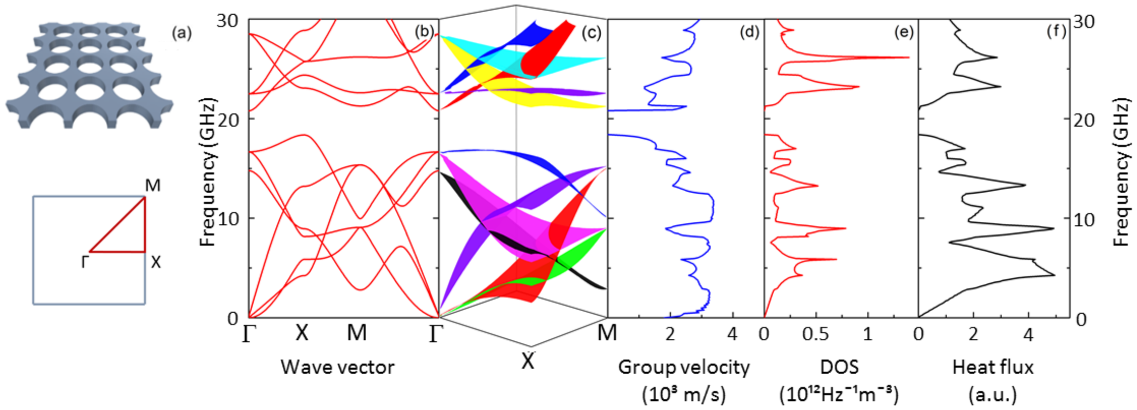

Figure II.9 (a) Scheme of the simulated structure together with its first Brillouin zone and the high symmetry points Γ (0, 0), X (π/*a*, 0), and M (π/*a*, π/*a*). Phonon dispersion on the boundaries (b) and inside (c) of the irreducible triangle with *a* = 160 nm, *r/a* = 0.45, and *h* = 80 nm. Spectra of the average group velocity (d), density of states (e) and heat flux (f) [43].

II.4.2 Group velocity and density of states

First we calculate the values of the group velocity $v_g(\omega) = \nabla_k(\omega)$ averaged between all values corresponding to the given frequency over the entire BZ. The obtained group velocity spectrum is shown in Figure II.9(d). The energy density of phonons is given by $\hbar\omega \cdot D(\omega)$, where $D(\omega)$ is the DOS at frequency ω given by:

$$D(\omega) = \sum_m \int_l \frac{dl}{v_{g_m}(\omega)} \qquad (2.27)$$

where the integral of *l* represent the length of constant frequency in *k*-space and *m* is the mode number, i.e. the mth eigenmode at any wavevector. thus the DOS is the summation over all modes available over the *k*-space at a given frequency [44].

II.4.3 Thermal conductance

The total heat transported in the structure of interest can be calculated in two ways. On one hand, it is possible to get the heat flux spectrum in the structure, given as the sum of the energy density over all modes present at a certain frequency, traveling with a certain velocity and weighted by the Bose-Einstein distribution $f(\omega, T)$:

$$\mathrm{Q}(\omega,\mathrm{T}) \;\propto \sum_{\boldsymbol{n}} \int_{0}^{FBZ} \hbar\omega_n \cdot \mathrm{D}_n(\mathrm{k}) \cdot \left|\overrightarrow{\mathrm{v}_g}_{n}(\mathrm{k})\right| \cdot f(\omega_n, T)\, d\vec{k} \qquad (2.28)$$

where v_n and D_n are the group velocity and the DOS calculated while paying close attention to the band intersections, and f is the Bose-Einstein distribution [45]. After each integral is calculated over the entire first Brillouin zone, their sum is taken and results in the heat flux. The spectrum of heat flux is shown in Figure II.9(f).

On the other hand, the thermal conductance is most often used. From the band diagram, it is calculated with the following equation:

$$\mathrm{G}(\mathrm{T}) = \frac{1}{2\pi^2} \sum_{\boldsymbol{n}} \int_{0}^{FBZ} \hbar\omega_n \cdot \left|\frac{d\omega_n}{d\vec{k}}\right| \cdot \frac{\partial f(\omega, T)}{\partial T}\, d\vec{k} \qquad (2.29)$$

It is worth noting that the two approaches to thermal conduction presented in this chapter, though quite different, are complementary. Indeed, the wave model presented in this section applies under quite strict conditions, i.e. structure size similar to the phonon MFP and very small surface roughness compared to their wavelengths. This is due to the fact that if no specular reflection occurs, no coherent interference can occur. Furthermore, the MFP of phonons, i.e. the distance travelled between two diffusive scattering events, needs to be large enough compared to the period that the phonons can “feel” this periodicity. As was shown by Zen *et al*. [41] this wave pictures explain experimental results quite well at very low temperature, while some other studies [46–48] show that the particle model is valid at high temperatures. Thus it is possible, at intermediate temperature, i.e. in the range 1-10 K roughly, that a combination of these models be needed to fully explain experimental observations, as will be shown experimentally at the end of Chapter V.

Chapter III

Fabrication and measurement methodologies

In this chapter, we will develop on the methodology to fabricate the samples, from the Si-on-insulator wafer to the measurable structures. The fabrication is presented in the order it is performed during the experiment. The following section deals with a brief overview of existing measurement techniques including the thermoreflectance, followed by a complete description of our thermal conductivity measurement system as well as the corresponding simulations used to extract the effective thermal conductivity.

III.1 Fabrication process

The fabrication process uses common Si micromachining techniques which will be described in detail in this section, following the order they appear in the fabrication of our sample. The process is performed on commercially available Si-on-Insulator (SOI) wafers. All pieces of equipment are available in clean room directly on-site at the Institute of Industrial Science, in the University of Tokyo, in clean rooms of class 1000 and accessible upon formation. There are three key parts to this fabrication procedure. The first one is the use of electron-beam (EB) lithography for the patterning of the nanostructures, which allows for state-of-the art designs with characteristic sizes of a few tens of nanometers. The second is the plasma etching technique used to transfer the pattern from the mask, composed of the electron-beam resist layer, to the Si layer. The last part is the oxide etching under vapor phase which allows for a stiction-free release of our structures. A global flowchart of the fabrication process is presented in Figure III.1.

In the following subsections, all the steps involved in the fabrication of the sample, from its design to its completion, are detailed. We also explain the choices made and the constraints, such as the integration of a heater/sensor with the structures and its consequences on further process steps.

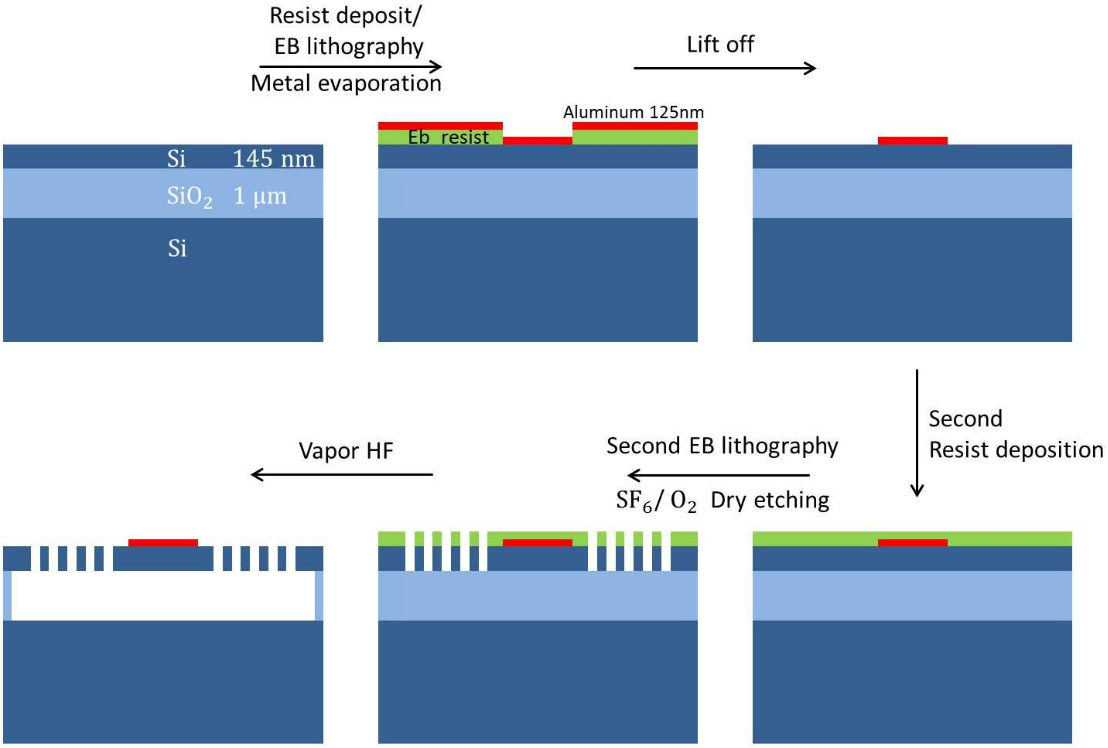

Figure III.1 Flowchart of the fabrication process. The flowchart represents all the major steps in the fabrication process from a cross-sectional point of view. Included are the initial sample, the metal deposition, the lift-off, the second resist deposition, the plasma etching and, lastly, the buried oxide removal steps.

III.1.1 Samples configuration

Samples were fabricated from a commercially available (100) Si-on-insulator (SOI) wafer purchased from ShinEtsu and are slightly p-doped. The top Si layer and the SiO_2 buried oxide (BOX) are 145 nm and 1 µm thick respectively for all structures presented in this manuscript, unless stated otherwise. Although a thinner top Si layer might prove beneficial, such wafers also come with a thinner BOX layer, which makes suspending the structures all the more challenging. The current compromise allows for a yield of nearly 100% and a good mechanical stability when removing the buried oxide. The original substrate is an 8 inch wafer that is separated into 16x16 mm chips for processing, further separated in 9 identical sub-chips to fit in the SEM holder. (Figure III.2 (left))

The number and positioning of the structures inside a sub-chip has been optimized both for measurement and fabrication purposes. The maximum number of structures on such a sub-chip is greater than 250, as shown in Figure III.2 (center), making successive measurements easy. The detailed pattern of a fishbone phononic crystal is shown for reference in Figure III.2 (right).

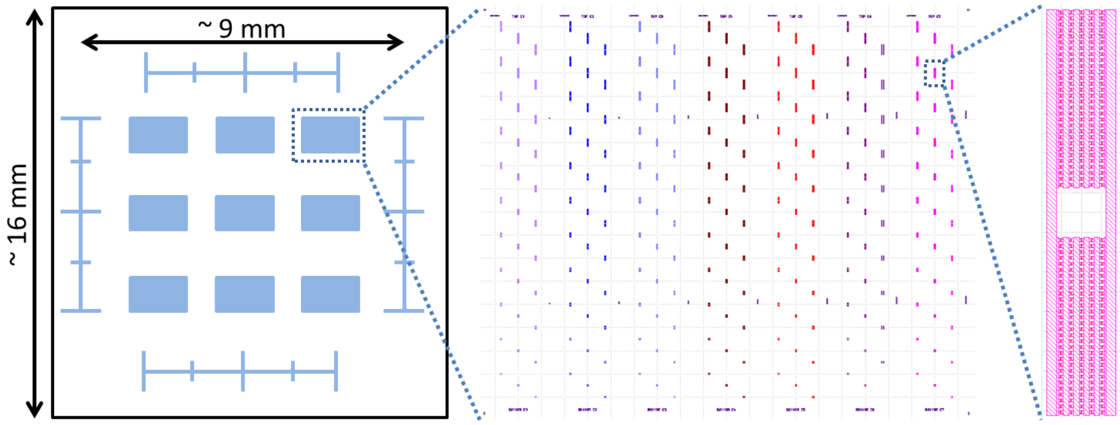

Figure III.2 Global design of a chip with (a) the complete chip as processed, (b) the global positioning of the structures in a sub-chip and (c) a close-up view on the pattern file of a fishbone structure as is used for EB lithography.

III.1.2 Cleaning of the substrate

The first step of the fabrication process is to clean the substrate. It is done by successively immersing the sample in Acetone, Isopropanol (IPA) and deionized water for 3 minutes each in order to remove the surface impurities. While acetone will remove the impurities, IPA will remove the acetone and water will serve as a last rinser.

Si possesses a 1-2 nm thick natural oxide layer. In order to succeed in the following fabrication steps, this layer needs to be removed. The previous cleaning is thus followed by a dipping of the sample for 5 seconds in a buffered hydrofluoric (BHF) acid solution. Since the native oxide layer appears quite rapidly under normal atmosphere, in a matters of a few tens of minutes [49], it is necessary to immediately proceed to the next fabrication step.

III.1.3 Resist spin-coating

Once the Si surface is clean, we spin electron-beam resist on the 16x16mm sample. We have mainly two types of resist at our disposal: ZEP520A and ZEP520A-7. The only difference is that the second possesses a lower viscosity, allowing for thinner resist thickness [50]. Both resist possess a good resistance towards plasma etching and allow for high aspect-ratio designs. The latter will still be privileged for designs which require more precision.

A typical spin-process recipe proceeds as follows:

1. 5 s at 500 rpm → Serves to uniformly distribute the resist
2. Slow acceleration up to 4500 rpm (5 s)
3. 60 s at 4500 rpm → Thin down the resist to the desired thickness

The rotation speed of the spin-coating process determines the thickness of the resist, with a faster rotation speed resulting in a thinner resist film [50]. Once the resist is applied, it is hardened by doing a pre-bake on a hot plate for 2 minutes at 180℃.

III.1.4 First Electron-beam Lithography step

After the deposition of the resist, a first step of Electron-beam (EB) Lithography is necessary. At that point, only the global marks, necessary for subsequent alignments, and the aluminum metal pads are drawn. The global marks can be seen in Figure III.2 (left) and are millimeter-long ladder-like patterns. The shape of a metal pad is that of a 4x4 μm^2 square.

The preparation for an EB lithography step requires a pattern file. Our files are prepared using a home-made Python code based on the IPKISS library, which contains basic elements for geometrical patterning, including a system of layers. Since it is possible to differentiate each element of the pattern and attribute it a layer, it is then possible to tune the electron-beam conditions separately. To each layer, it is indeed possible to attribute a specific dose, which in turn has an impact on the shape of a given pattern, with a higher dose meaning that proximity effects have more chances to impact the shape between close patterns [51,52]. Taking a circular hole as an example, a higher dose will increase the diameter of the hole. While this parameter is irrelevant for large patterns such as the Al pads, it is crucial to successfully pattern, for example, the rectangular shapes used in the fishbone periodic structures, in which the dose can be increased in the corners to avoid their rounding.

Even after all the shapes have been fixed, be it for the Al pads or the nanostructures, it is thus still possible to slightly alter their shape and size by tuning the dose and the resist thickness. In the case of metal pads, the dimensions are large enough that a classical resist thickness of 350 nm with a dose of 200 $\mu C/cm^2$ is used, which usually correspond to the clear dose for this resist.

III.1.5 Development

Once the lithography is done, the pattern will be revealed by chemical processing. Since the ZEP520A is a positive resist, the irradiated parts, transformed into small blocks from their original state as a long polymer chain, will be removed by the developer.

The typical development process is as follows:

1. 3 min in ZED-N50 at 13℃
2. 1 min in ZMD-B
3. Drying under N2 flow
4. 3 min post-bake on a hot plate at 140℃

ZED-N50 is the proprietary developer composed of n-Amylacetate while the rinser, ZMD-B, is made of Methyl isobutylketone. Together they constitute a set which is specially adapted to this resist. When developing the resist, it is important to pay attention that no thin layer remains in the parts that have been removed, otherwise impeding the following process, be it metal deposition or plasma etching. On the other hand if the development is done too strongly, it is possible that high aspect-ratio parts of the resist be destroyed, such as for very thin nanowire patterns.

ZMD-B is used to stop the development by removing the remnants of ZED-N50. Although the development speed becomes negligible after its application, this step is followed by drying the sample. Lastly, a post-bake completes the process, both fixating and hardening the remaining resist.

III.1.6 Metal deposition

To deposit the Aluminum forming the pads, we use a ULVAC EX-300 electron-beam assisted metal evaporator. We found that using quite slow deposition rates gave a relatively smooth surface, albeit the roughness is still visible on SEM images. The conditions used for the deposition are an acceleration voltage of 10kV and a current of approximately 60 mA for an effective deposition rate of 0.5 to 1 Å/s. Deposition is done under vacuum with background pressure lower than $5.0 * 10^{-4}$ Pa to avoid impurities. The source contains 5N Al, which means the purity reaches 99.999 % at least.

While developing the fabrication process, the Al pads thickness has been adjusted to the current value of 125 nm. Although it holds no specific physical reason, we continued with 125 nm for the sake of comparing the new structures to the ones already fabricated.

III.1.7 Lift-off

After the metal deposition process, the whole sample is covered by aluminum. In order to keep only the global marks and the metal pads useful for the measurement we proceed to lift-off the aluminum layer by removing the remaining resist with the following process:

1. Dip the sample in ZDMAC (proprietary resist remover) at 80℃ until visual disappearance of aluminum.
2. Clean the surface with Acetone for >3 min.
3. Remove the acetone with IPA for > 3 min.
4. Dry the sample

ZDMAC is constituted of Dimethylacetamide. Dipping the sample in a beaker of this solution will remove most of the resist but the aluminum sheet still remains attached to the sample. Thus, it is necessary to use sonication to detach the unnecessary aluminum. However, if this step is not done cautiously, i.e. if the strength of the sonication is excessive, the aluminum pads or global marks will be removed as well, so that the fabrication process must be done again from the beginning. The following cleaning steps proceed in the same manner as the first time.

This lift-off/cleaning step is followed by a second resist spin-coating, identical to the first one, in preparation for the second EB lithography step.

III.1.8 Second EB Lithography step

The main difference between this step and the previous one is the necessity of alignment, i.e. to look for the coordinates of the exact center of the chip. Since the Al pads have already been deposited, the phononic crystals are drawn around them.

The alignment process consists in finding the coordinates of the centers of the global marks in the X-Y basis of the lithography machine. An automatic finding process is available but unusable in our case due to the poor contrast between Si and Al in SEM. A manual check of the positions in the embedded SEM is thus necessary. The Al pad, here 4 µm in width, needs to be aligned in the center of the suspended structure, here 5 µm in width, thus requiring a precision for the alignment below 500 nm. Although this is easily achievable, some drift can occur as the lithography progresses, reducing the yield. Following this step, a second development of the resist is conducted exactly in the same way as the first one, which result is shown in Figure III.3 .

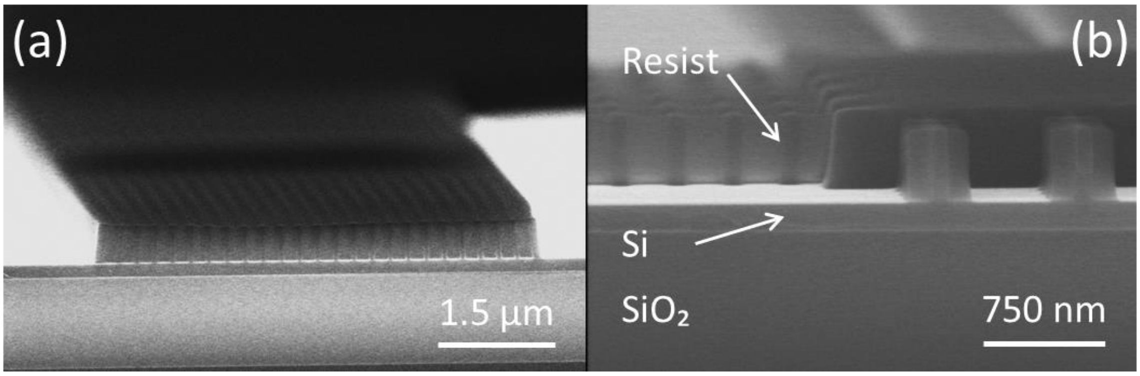

Figure III.3 Samples after the second development step. (a) Cross section of a 2D PnC after the development of the resist. (b) Cross section of a fishbone structure after the development of the resist.

III.1.9 Inductively coupled plasma reactive-ion etching (ICP RIE)

The pattern drawn by lithography in the resist is then transferred to the Si layer by means of a cryogenic ICP RIE process [53]. We use a mixture of SF_6 and 0_2 to etch our Si layer in an Oxford PlasmaLab 100 RIE system.

We have several adjustment parameters at our disposal [54]:

- The absolute and relative flux of SF_6 and O_2. These will impact the ratio of physical and chemical etching as well as the roughness of the surfaces. Indirectly, it will also affect the verticality of the walls.
- The plasma power. This will determine the overall etching speed
- The etching time
- The etching temperature. A lower temperature will increase the selectivity of the etching in silicon versus the resist and will prevent undercuts [55].

Although the pressure is expected to be an important parameter as well, it was found later that a leak was present in the chamber, which made any evaluation of the pressure irrelevant.

Given the gases at our disposal, a cryogenic etching was preferred for better verticality of the walls and surface roughness [56]. Our etching system is commonly used for deep RIE which means than the etching speed is very fast in general. By tuning the recipe it was possible to reduce significantly the etching speed, which has been brought down to around 600 nm/min. However, given the small thickness of our sample, it still poses the problem of the stability of the plasma.

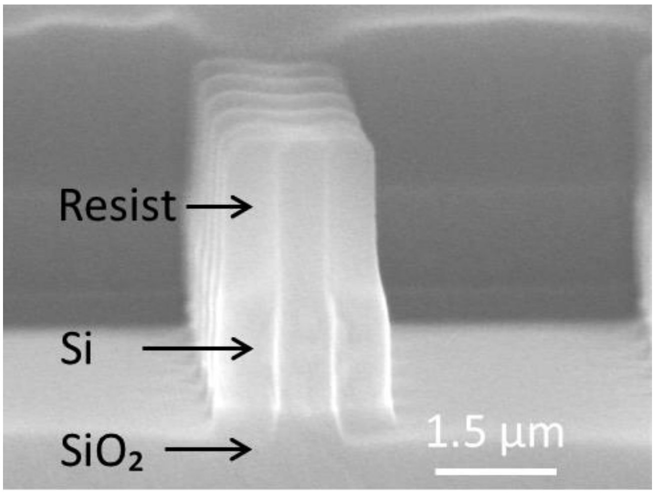

Figure III.4 Cross-sectional SEM image of a fishbone structure after the ICP RIE step. The three visible layers from top to bottom correspond to the resist, the Si layer and the SiO_2 box respectively.

The final recipe parameters used are:

- RF Forward power : 50 W
- ICP Forward Power : 500 W
- Etching time : ~20 s
- SF_6/O_2 : 60/17.5 sccm

An example of the result is shown in Figure III.4 in the case of a fishbone. The cross section shows the three visible layers. The bottom layer is the BOX layer still present. The middle part is the top Si layer and the top part is the remaining resist after the end of the plasma. A few observations can be made from this image. First, the pattern in the resist is getting slightly larger at the base of the resist, which cause the Si pattern to be a bit larger. Then, the

SiO2 layer is etched over a few (tens of) nanometers. While this is required for further processing of the sample, it is necessary to be careful that the resist is not completely etched during this time.

III.1.10 Removal of the resist

This step is usually quite straightforward and proceeds exactly as the lift-off step. The main difference is that to be sure of the disappearance of the resist, we let the sample in ZDMAC for around 1.5 hour on a hot plate at 80℃ and 0.5 hour in a sonic bath. A fishbone structure at this stage of the fabrication process is shown in Figure III.5:

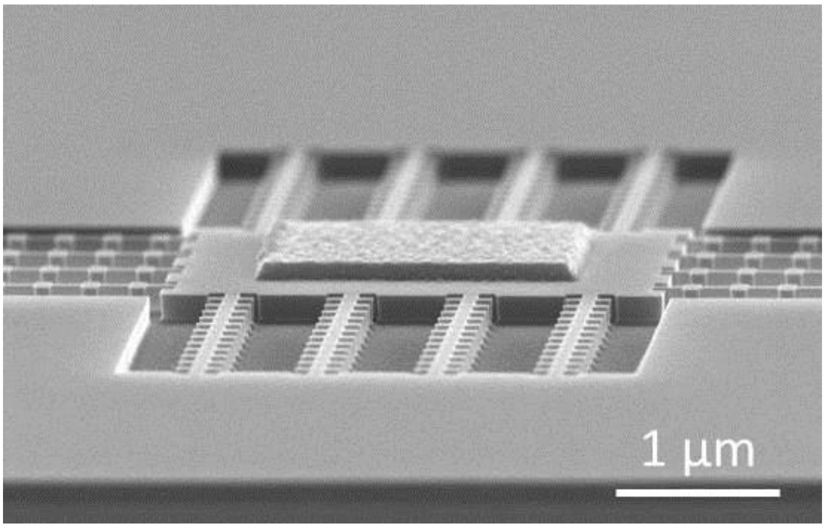

Figure III.5 SEM image of a structure after the last of the resist has been removed. Are visible the Al pad, the underlying Si island and the fishbone beams.

III.1.11 Removal of the buried oxide layer

This last step of the fabrication process is one of its key points. Hydrofluoric (HF) acid is classically used to release such structures. However, in order to avoid the stiction of the structures on the underlying substrate, this wet etching step must be preceded by a back etching. We chose not to perform this for two reasons. The first reason is that back-etching can only be performed over a large area at once, thus weakening the sample. The second reason is that the Al etch rate in liquid HF is very high, thus requiring two additional steps to protect the pads. Eventually, vapor HF etching has been preferred over critical point drying due to its simplicity and controllability. After we developed a home-made etching system based on a principle developed by Fukuta *et al.* [23], we switched to a commercial one for more stability. The chemical reaction can be described by the following equations:

$$\mathrm{HF(g)} \leftrightarrow \mathrm{HF(ads)} \text{ and } \mathrm{H_2O(g)} \leftrightarrow \mathrm{H_2O(ads)} \tag{1}$$

$$\mathrm{2HF(ads)} + \mathrm{H_2O(ads)} \leftrightarrow HF_2^-\mathrm{(ads)} + \mathrm{H_2OH^+(ads)} \tag{2}$$

$$\mathrm{SiO_2(s)} + 2HF_2^-\mathrm{(ads)} + \mathrm{2H_2OH^+(ads)} \rightarrow \mathrm{SiF_4(ads)} + \mathrm{4H_2O(ads)} \tag{3}$$

$$\mathrm{SiF_4(ads)} \leftrightarrow \mathrm{SiF_4(g)} \text{ and } \mathrm{H_2O(ads)} \leftrightarrow \mathrm{H_2O(g)} \tag{4}$$

with (s) standing for solid, (g) for gas and (ads) for adsorbed on the surface.

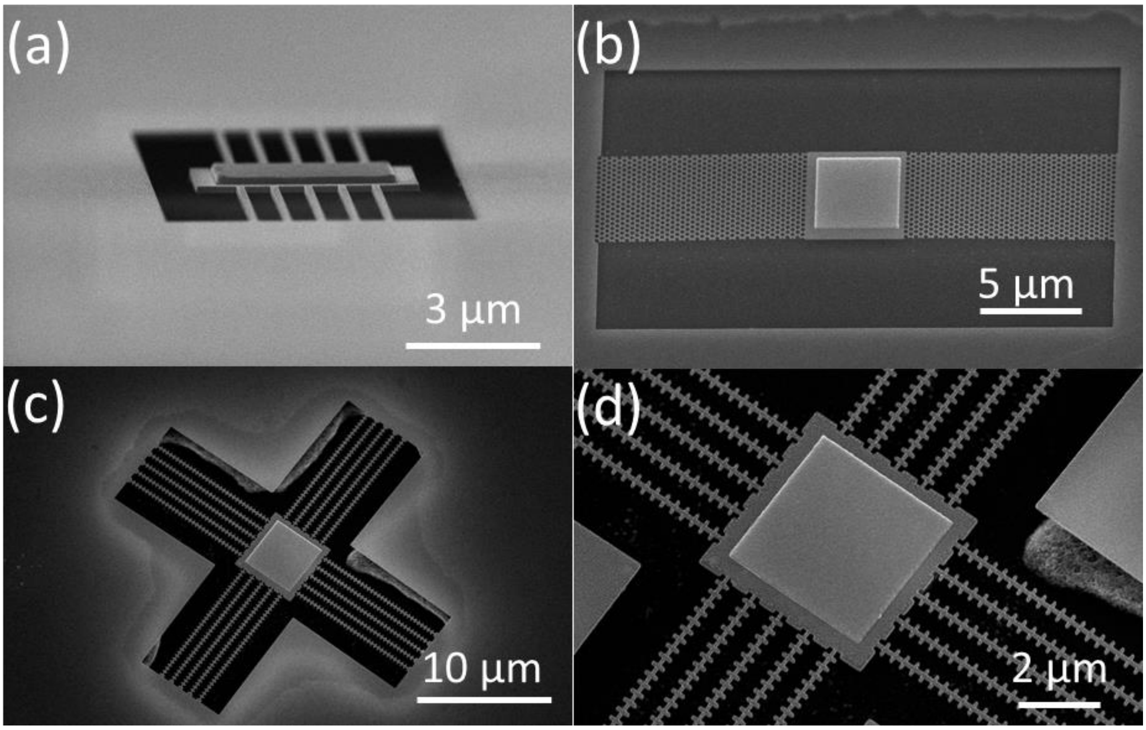

Figure III.6 SEM images of completed structures of each type. (a) SEM image of a nanowire structure. (b) 2D PnC with a hexagonal lattice. (c) 1D fishbone structure and (d) close-up on the fishbone structure central part.

Given the small amount of chemicals adsorbed on the surface, which is regulated by the temperature of the sample to be etched, the etching speed will be much lower than a completely wet etching. Thus, it is possible to more precisely control the amount of buried oxide etched. The amount of oxide to be etched depends on the largest distance between two entry points for the etchant, i.e., the central Si island. For safety, at least 3 µm need to be etched. The approximate amount of oxide etched can either be verified by a top SEM image or in a classical optical microscope. If the etching is found to be insufficient, the sample can easily be placed in the etching system once again and the process completed.

Overall, this method provide a relatively quick and easy-to-implement etching method, provided that the environment in clean room, such as the temperature and humidity, is well regulated, which gives good results as can be seen in Figure III.6.

III.2 Micro time-domain thermoreflectance system

Measuring electrical or thermal properties of nanostructures is often a challenge which requires a specific preparation of the sample itself, meaning that the fabrication process is conducted to accommodate the subsequent measurement. When it comes to thermal measurements, there are a few widely used techniques, which will be briefly introduced hereafter, with their own advantages and inconvenients. These techniques can usually be divided into 2 categories, which are electrical and optical.

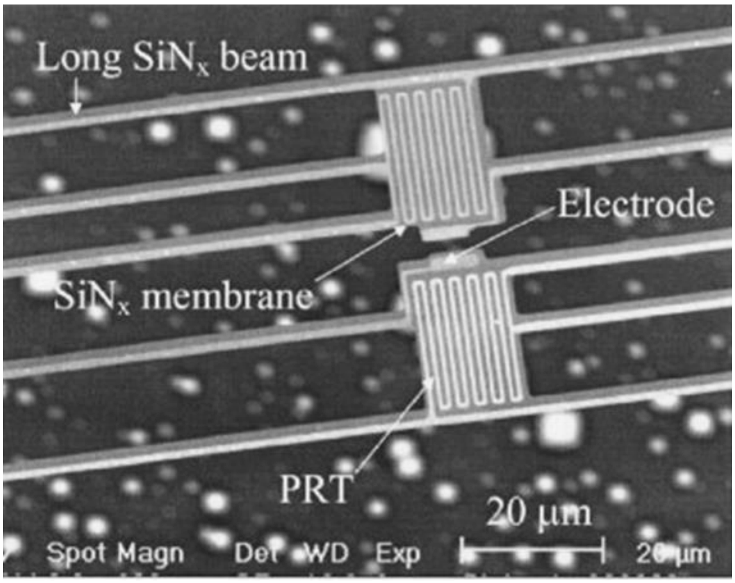

Figure III.7 SEM image of an electrical measurement platform showing all the electrical wires [57]. The structure under study is placed between the 2 central electrodes. PRT stands for Platinum resistive heater, which can act both as a heater and a sensor.

The electrical measurement scheme usually consists of the structure to be studied with a heater on one end and a sensor on the other end. Both are usually conductive metal wires through which a current passes. The heater has its temperature raised by Joule effect while the sensor will have its resistivity modified after the heat pass through the structure under study and increase its own temperature (sensor). A common implementation of such a method is depicted in Figure III.7. This electrical measurement scheme can then make use of either the fundamental component of the electrical signal, its 2nd or 3rd harmonic [58] or the steady state [59,60].

The advantage of the electrical techniques resides in the small increase in temperature that is necessary to make a reliable measurement, which is on the order or less than a mK. This enables the measurement to really probe thermal properties at the desired temperature, which is critical for thermal measurement at very low temperatures, i.e. below 4 K. At these temperatures, the serpentine thermometers are replaced by SINIS junctions. Two such junctions are placed on a suspended thin film. The temperature in one of the junction is measured as a function of the voltage in the other. The temperature will depend on the dissipation rate in the suspended structure surrounding the two junctions, be it a membrane or PnC. This technique was used by Zen *et al*. [41]. Since electrical measurements are indirect measurements, it requires careful analysis to extract any thermal property. Furthermore, it also requires the measurement system, i.e. the heater and sensor and suspension beams, to be directly integrated with the structure under study, which require a large area on the chip. The necessity of physical contact at the electrodes also makes it impractical to measure a large number of structures. It is however the best option for measurement over various temperatures, as long as the thermometers are designed accordingly, and has been used extensively for measurements of various nanostructures [61–64] including nanowire arrays [65].

The second category of measurements systems for thermal properties of nanostructures are to be put in the optical category. Brillouin light scattering (BLS) [66] or Raman spectroscopy [67–69] are two examples of such optical measurement systems. However, the most well-established optical scheme is called the thermoreflectance method, which has been chosen for this work. The main challenge in our case was to be able to measure an important number of suspended structures in a short time, with satisfying accuracy. This was not possible with electrical methods as each structure requires a specific sample, including the electrodes and connections, thus only one sample can be measured at a time.

III.2.1 Introduction to TDTR

The time-domain thermoreflectance has been independently proposed in 1986 by the groups of Maris [70] and Eesley [71]. Thermoreflectance measurements are based on the temperature dependence of a material’s reflectivity [72–74]. The classical scheme uses a metal thin film transducer heated by an optical pulse (pump) and which reflectivity is probed by another optical beam (probe). The simplified equation linking temperature and reflectivity can be written as: $\frac{\Delta R}{R} = C_{th}.\Delta T$, where R and ΔR are the reflectivity and reflectivity change respectively, C_{th} is the thermoreflectance coefficient, and ΔT is the change in temperature at the probing location.

The thermoreflectance coefficient C_{th} of metals is typically in the 10^{-4}-10^{-6} K^{-1} range for an illumination in the visible spectrum. The room temperature spectra of thermoreflectance coefficient for several metals are shown [75] in Figure III.8.

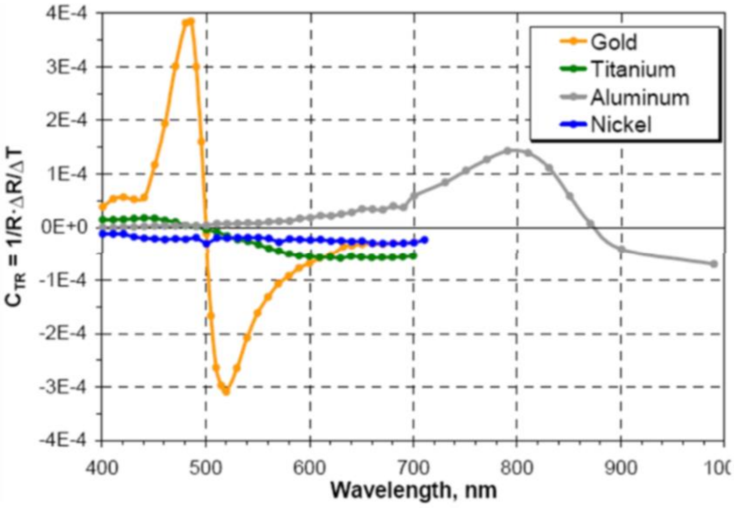

Figure III.8 Spectra of thermoreflectance coefficients for different metals [75].

The most commonly used thermoreflectance heaters/sensors consist of a pairing of gold with an illumination wavelength of 470 or 532 nm [76], or aluminum with an illumination wavelength of 800 nm [75]. These materials combine good efficiency with a versatile fabrication process. The latter combination is used in the most common TDTR setup involving a Ti:sapphire laser with picosecond [71] or femtoseconds [77–80] pulses, which schematics is shown in Figure III.9. The delay between the pump and probe pulses is introduced via a mechanical delay stage. The Ti:sapphire laser used for illumination has a repetition rate close to 80 MHz, which limit the maximum pump-probe delay to around 10 ns. The use of a modulator can decrease this repetition rate and enable for longer acquisition times. However, this TDTR technique is usually reserved for systems with a rather large diffusivity, and most often for cross-plane measurements. It also enables to measure the interface thermal conductance between layered structures [81,82] as well as the heat capacity of materials. When using such an optical measurement method, the sample can be simply put into any type of optical cryostat and submitted to various environmental conditions, although it is even possible to perform measurement directly at atmospheric pressure.

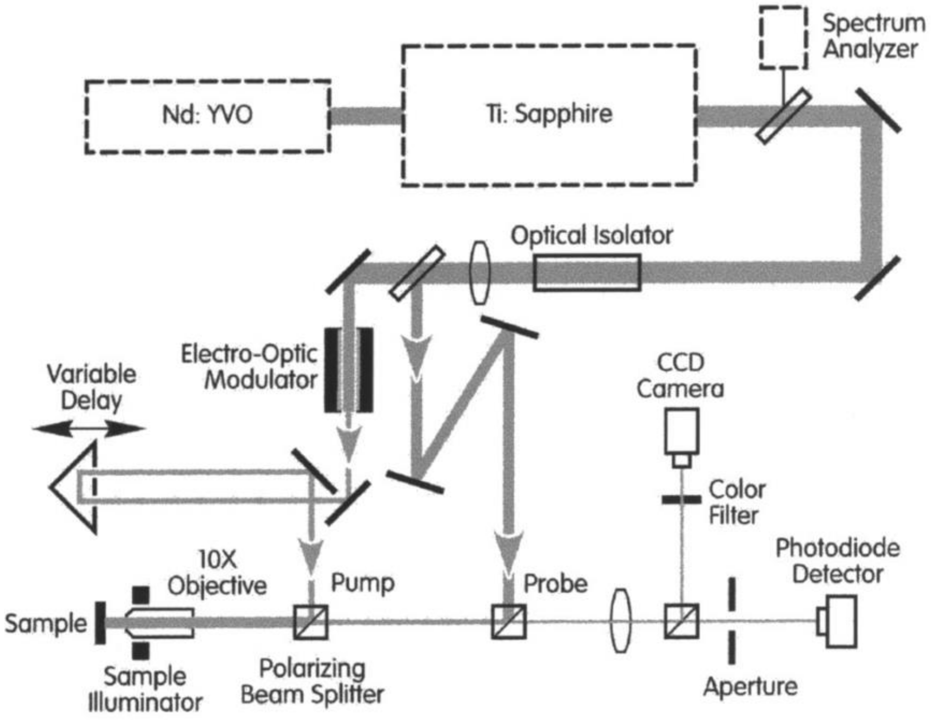

Figure III.9 Schematic of the most commonly used time domain thermoreflectance scheme [83].

With the limitations of this implementation, this setup is not suitable for in-plane measurements of low diffusivity nanostructures as is. Our goal was to combine the advantages of both the electrical measurement system as well as the thermoreflectance one. With electrical measurements, the heat flows through a single structure of interest and it is possible to probe the in-plane thermal conductivity. Optical measurements on the other hand, and in particular TDTR, bring an easier and faster measurement, with minimal sample preparation. By taking into consideration some evolution around the thermoreflectance system as well as thermal mapping measurements schemes [73,74,84,85], we determined that the transducer film could be reduced in size towards a micrometer-sized square and thus each structure could possess its own transducer, allowing for separate probing of structures on a same chip. In order to eliminate all parasitic heat channels, similarly to the electrical schemes, it was necessary to suspend the structure and position the transducer surrounded by the structures of interest, which resulted in the positioning displayed in the previous fabrication section. From this situation, the main scheme stays similar to that of the above-mentioned literature, with a pump and a probe beam, a microscope objective to focus the lasers on the samples and a detector to measure the signal. To assess if using a lock-in amplifier was adequate, the main prerequisite was to determine the time-scales necessary for our measurements. COMSOL Multiphysics was used to simulate the heat propagation in a typical structure, i.e., a simple suspended Si thin film for example, when a heat pulse is applied in its center. These simulations are detailed later in section II.2.3. To efficiently measure heat transport in our suspended structures, we needed both a long time-scale acquisition up to around 1 ms and a good resolution around 10 to 100 ns. Thus, neither the high repetition rate of Ti:Sapphire laser based systems, nor the acquisition time of a lock-in amplifier fit our desired specifications. We then decided on a scheme using laser diodes that can be modulated at low frequencies, with tunable pulse durations to determine optimal measurements conditions. The choice of a pump/probe couple with different wavelengths has been done to simplify the acquisition, which is further sped up by the continuous nature of the probe beam. Indeed, compared to the use of a lock-in amplifier, with which each delay needs to be acquired separately, using a continuous probe allows for near-simultaneous acquisition of all the delays. In the following section is detailed the implementation of our thermoreflectance system, which then belongs to the category of so-called photothermal reflectance method [86]. Although our system enters this category, no previous instance has been designed for and applied to measurements of suspended nanostructures similar to what can be done with an electrical method.

The thermoreflectance measurement is done as follows: A laser pulse heats the surface periodically, which translates into a peak in reflectivity. After the end of the pulse, the temperature inside the sensor will progressively decrease, as the heat flows through the structure. The reflectivity of the sensor, which is continuously measured by a probe laser, will follow exactly the same trend as the temperature decay. This decay characterizes the heat transport properties of the structure surrounding the heater/sensor and we refer to it as thermal decay time or simply decay time (τ). It follows an exponential decay that can be written as:

$$\frac{\Delta \mathrm{R(t)}}{\mathrm{R}} = \mathrm{A}e^{-\alpha t} = \mathrm{A}e^{-t/\tau} \qquad (3.1)$$

with R the base reflectivity, $\Delta \mathrm{R(t)}$ the variation of reflectivity due to heating, A a constant, α the thermal decay rate and τ the thermal decay time.

The first advantage of our method, common with other thermoreflectance techniques, is the small footprint of the integrated structure. Since, unlike electrical measurements, there is no need for any contact for the measurement, each structure takes only minimal space on the chip. In our implementation, a typical structure occupies an area less than 50x50 μm^2. As a consequence, a single sub-chip can accommodate several hundred structures, as shown in the first part of the fabrication section. This method minimizes fabrication bias on the measured thermal conductivities.

The second advantage of our method is its overall speed. The measurement itself is done in a matter of minutes (<5 min).This time includes both the acquisition of the 10000 frames (~30 seconds depending on the number of points in the signal) and observing the variations of the signal, i.e. decay time, over a few minutes to account for variations on macroscopic time scales. Combined with the small footprint, this allows for more than 100 structures to be measured in a single day, far outpacing similar measurement techniques.

The last point is the accuracy of the measurement, which is estimated to be around ±6% for typical structures, in the norm for this type of measurement. This estimation is based on the measurements of a large numbers of structures and corresponds to the range in which measurements of identical structures are. The accuracy depends largely on the decay time, with very short decay times more subject to uncertainties.

III.2.2 Details of the experimental setup

The heater/sensor was chosen to be the well-established Al layer accompanied by an illumination wavelength around 800 nm. Rather than sampling the signal at different pump-probe delays, we chose to use a continuous probe laser. Following the above-mentioned requirements, we selected a 785 nm laser diode which we paired with the Al heaters/sensors. Another advantage of using aluminum in combination with a 785 nm probe laser is that when measuring at low temperatures, the spectrum is slightly blue-shifted [87,88], which causes only minor variations in the thermoreflectance signal.

To speed up the acquisition, the lock-in amplifier in the classical system is replaced by an oscilloscope acquiring a continuous signal over and over. The pump laser is also a laser diode, but with a wavelength below 700 nm so that it can easily be optically separated from the probe beam. Both lasers present a good optical stability which is important for measurements over an extended period of time. The pump is pulsed thanks to a delay generator. Both the repetition rate and the pulse duration can be varied. The repetition rate is usually kept at 1 kHz because it provides a satisfying balance between acquisition speed and time for the heated structure to cool down before the next laser pulse. Both these lasers are aligned together. After this point, they follow the same optical path to the sample. The reflection from the sample goes then either to a camera, from which we can observe the surface, or are focused onto the detector. The complete optical path is detailed in Figure III.10 and a photo of the system in Figure III.11.

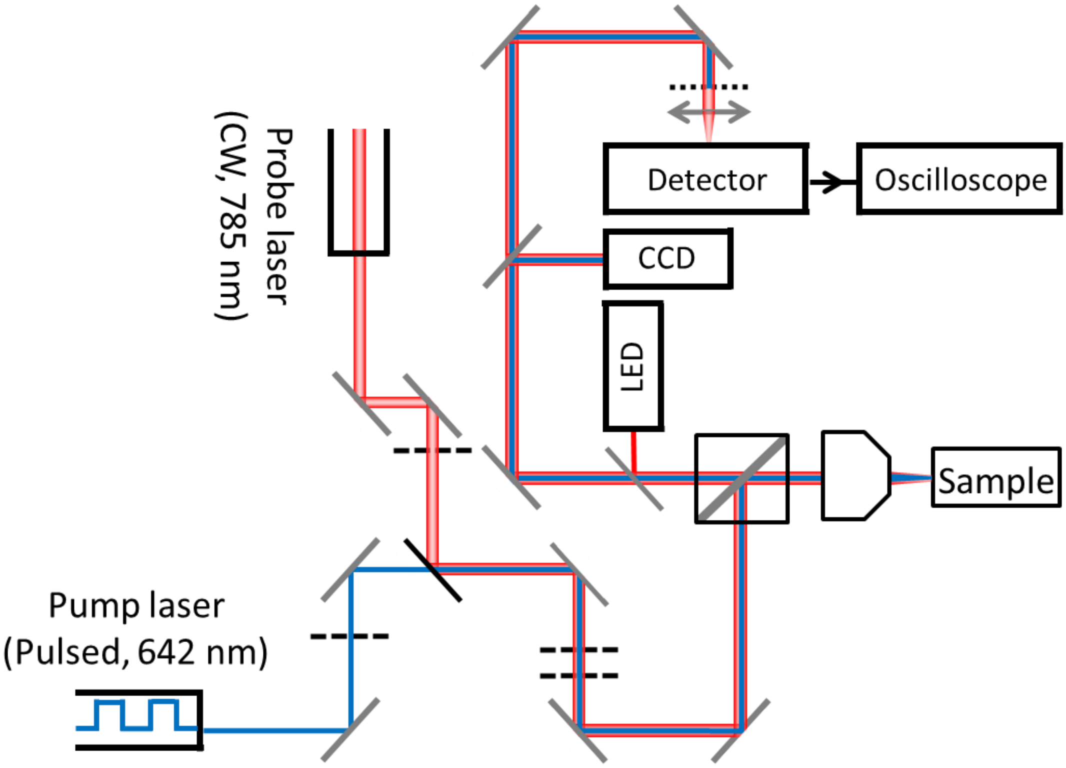

Figure III.10 Schematics of the TDTR setup. Gray lines are mirrors. Black dashed lines are ND filters. The small dashes and the double-arrow in front of the detector are the band-pass filter and lens, respectively.

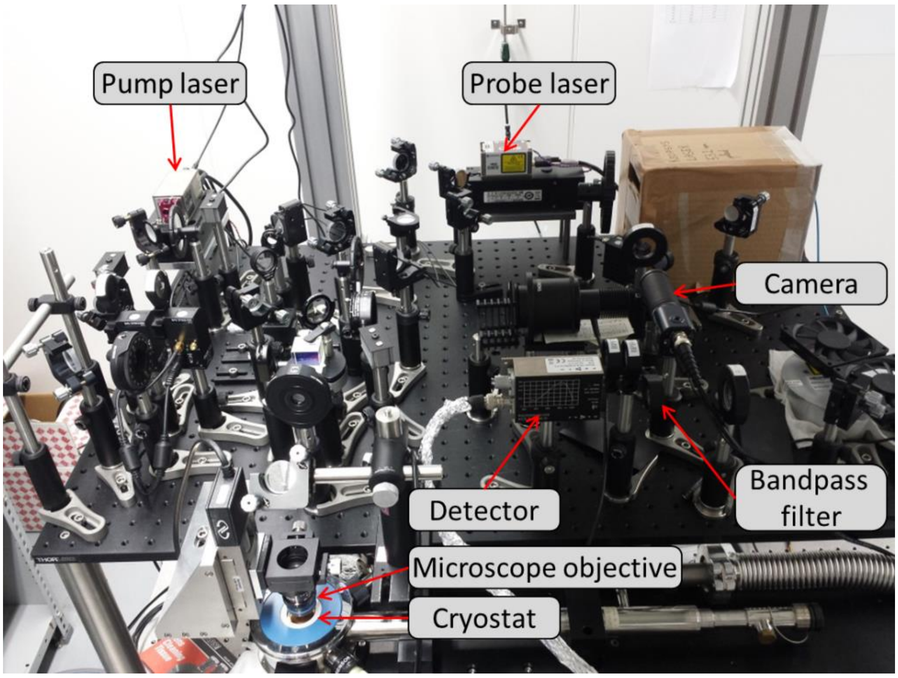

Figure III.11 Global view of the optical measurement system.

From their respective emission point, the laser beams are joined together by means of mirrors and a half-mirror. Similarly to what is shown in Figure III.10, they follow the same path onto a polarized beam splitter on which they are reflected to a microscope objective that focuses them on the sample, as can be seen on Figure III.12. We use a 40X objective with a numerical aperture of 0.60. The sample itself is mounted inside an Oxford Instruments Microstat HiRes II-N cryostat. Measurements are done under vacuum with a pressure $<1.10^{-2}$ Pa to avoid any convection problem. The temperature inside the cryostat can be controlled between 3.5 K and 400 K by means of a liquid helium cooling system and a heating copper plate. The cryostat itself is mounted on a XY-translation stage which allows for a positioning of the sample under the laser beams with a minimum step size of 50 nm, well under our optical detection capabilities.

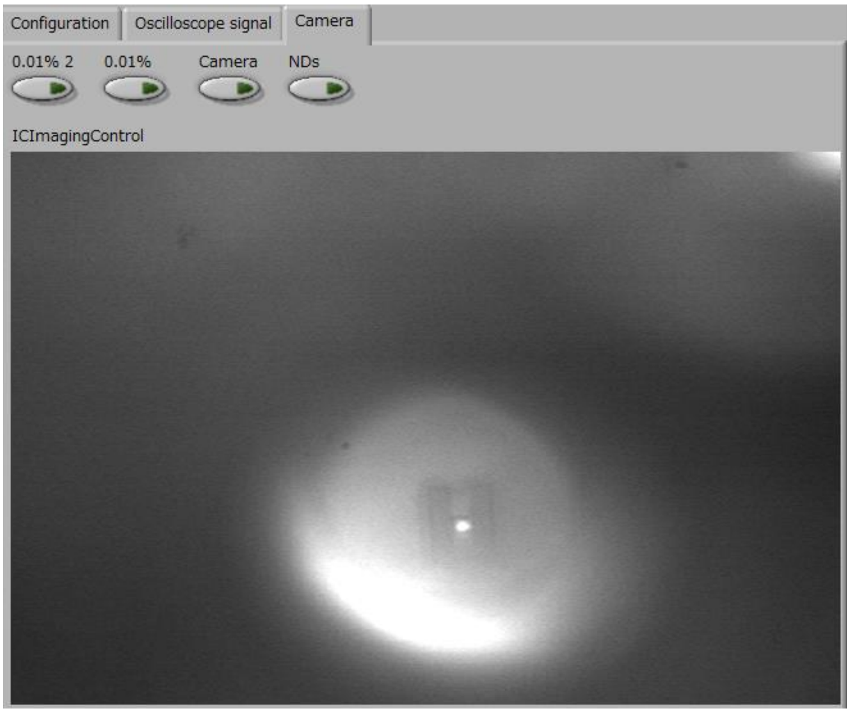

Figure III.12 Optical microscope image of a sample mounted in the cryostat, with the laser beams hitting the central metal pad.

After reflection, the polarization is changed and the beams pass through the beam splitter. After some more mirrors for beam alignment, they are directed to a focusing lens and onto the detector. Since the exponential decay of the signal is usually above 1 µs, and the heating pulse is also usually set to 1 µs, the detector has been chosen with a frequency of 200 MHz that ensure there will be no distortion to the acquired signal.

The signal is then transmitted to a Tektronix DPO7105 1 GHz oscilloscope by means of a BNC cable. The bandwidth of the oscilloscope has been chosen above that of the detector to avoid any unnecessary distortion and the 8 bit resolution is in the norm. This model is also able to superpose up to 10000 acquired waveforms and perform an average, which provides a signal with a much better S/N ratio providing the signal is stable. The resulting signal is sent to a Labview program controlling all automatized parts of the optical measurement system (red curve in Figure III.13).

III.2.3 Data acquisition

The Labview program was developed to facilitate to data acquisition as well as improve both the precision and the speed of the analysis. Its main function is to provide simple and automatic control over the instrumentation, further clean the signal by box-averaging (white curve in Figure III.13) and perform a real-time exponential fit of the decay (respectively the green line and blue curve in Figure III.13). The box averaging reduces the signal to 1000 points. This means that if the initial signal has 10000 points as is usually the case, an arithmetic average will be taken for every ten adjacent points. Here also, the recorded length is kept at 10000 because it provides a good balance between the quality of the signal and the acquisition time. Acquiring one curve with 10000 points averaged 10000 times takes around 3-5 minutes. The averaging itself takes only a fraction of that time. However, while measuring it is sometimes possible to observe fluctuations in the decay time for several seconds. It is thus important to take into account these variations and, if necessary, average over a few minutes.

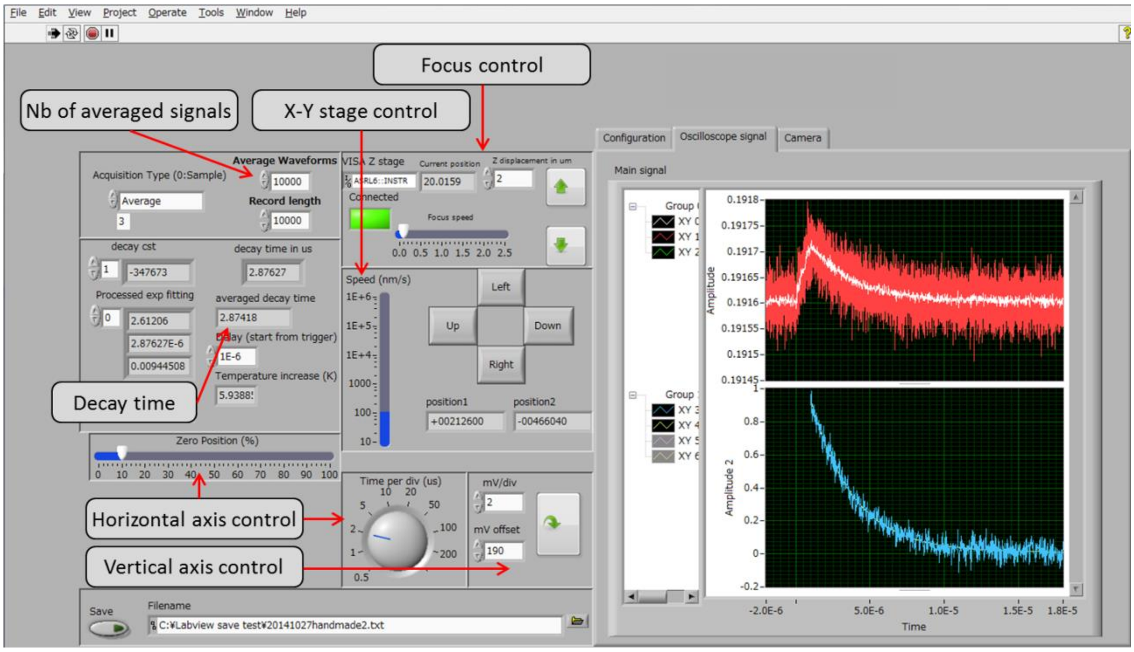

Acquisition Type (0:Sample): Average, 3
Average Waveforms: 10000
Record length: 10000
VISA Z stage: ASRL6::INSTR
Connected
Current position: 20.0159
Z displacement in um: 2
Focus speed
decay cst: 1, -347673
decay time in us: 2.87627
Processed exp fitting: 0, 2.61206, 2.87627E-6, 0.00944508
averaged decay time: 2.87418
Delay (start from trigger): 1E-6
Temperature increase (K): 5.9388
Zero Position (%)
Speed (nm/s)
position1: +00212600
position2: -00466040
Time per div (us)
mV/div: 2
mV offset: 190
Save
Filename: C:¥Labview save test¥20141027handmade2.txt

Figure III.13 Main screen of the Labview program during measurement. All the commands are on the left. In the right part are displayed all the relevant curves: the base curve as output by the oscilloscope (red), the box-averaged curve (white), the decay of the box-averaged curve (blue) and the exponential decay fit (green line) superposed on the blue decay curve.

All the graphs, including the exponential fit, are displayed in real-time, as is the decay time. The value of the baseline, the shape of the decay and the intensity of the thermoreflectance peak are good benchmarks to test the quality of the laser beam positioning and focus on the Al pad.

To achieve an optimal measurement, components are chosen specifically for the wavelengths used. Beam splitters and quarter-wavelength plate are designed for the probe wavelength of 785 nm. A band-pass filter is placed just in front of the detector and centered on 780 nm with a FWHM of 10 nm. It filters out the incoming pump light. The Si detector's 200 MHz bandwidth guarantees a response time fast enough for the measurement not to be distorted. The setup allows for estimated temperature changes ΔT of a few kelvins with sufficient signal to noise ratio for analysis. With the above-mentioned expression for the thermoreflectance coefficient, we can estimate the temperature change. We know the reflectivity change directly from the measured signal and the thermoreflectance coefficient is estimated to be 1.2 x 10^{-4} K^{-1} [75]. While earlier measurements were performed with an increase in temperature inferior to 10 K, the addition of an electric low pass filter reduced this to below 5 K, in order to avoid changes in material properties during the experiment. The air-bridge configuration, illustrated in Figure III.14(left), allows us to obtain the thermal conductivity with high reliability, because all the given heat supplied by the heating pulse diffuses via the structure of interest. Convection is negligible in vacuum. Similarly, radiation from the system has been calculated at room temperature. For an increase in temperature of 5 K, the radiation losses are estimated to be 4 nW at most, calculated with:

$$\dot{\mathrm{Q}}_{tf\rightarrow s} = \sigma \mathrm{A}_{tf} \mathrm{F}_{tf\rightarrow s}(\mathrm{T}_{tf} - \mathrm{T}_{s}) \qquad (3.2)$$

with $\dot{\mathrm{Q}}_{tf\rightarrow s}$ the radiation flux from the membrane to the substrate, σ the Stefan-Boltzmann constant, A_{tf} the surface of the membrane, $\mathrm{F}_{tf\rightarrow s}$ the view factor between the two radiating plates, here taken to be 1, T_{tf} and T_{s} the temperatures of the thin film and substrate respectively. This over-estimate still only accounts for ~2% of the input power. At low temperature, radiation losses are negligible.

III.2.4 3D FEM simulations: Extracting the thermal conductivity

The optical measurement system only provides exponential decays that can be compared to that of similar structures. In a similar way, we perform simulations that provide a decay time, with the thermal conductivity as parameter. By fitting these two values, we can extract the correct thermal conductivity.

To do that, we use the commercial software COMSOL Multiphysics®, with its heat transfer module. To be able to accurately reproduce in the software the structures we just measured, we perform SEM measurements to get the desired dimensions. We are then able to precisely recreate a 3D model of the structure of interest, as shown in Figure III.14(right) for the case of nanowires. The heating laser pulse is simulated by an inward heat flux on the surface of the metal pad which temporal shape is a rectangle function of 1 µs reproducing the shape of the real laser beam. Its spatial distribution is a Gaussian beam centered on the Al metal pad. The temperature is monitored in the center of the metal pad, in which it is uniform in the considered time scales and reproduces the trend observed experimentally (see Figure III.14(lower)).

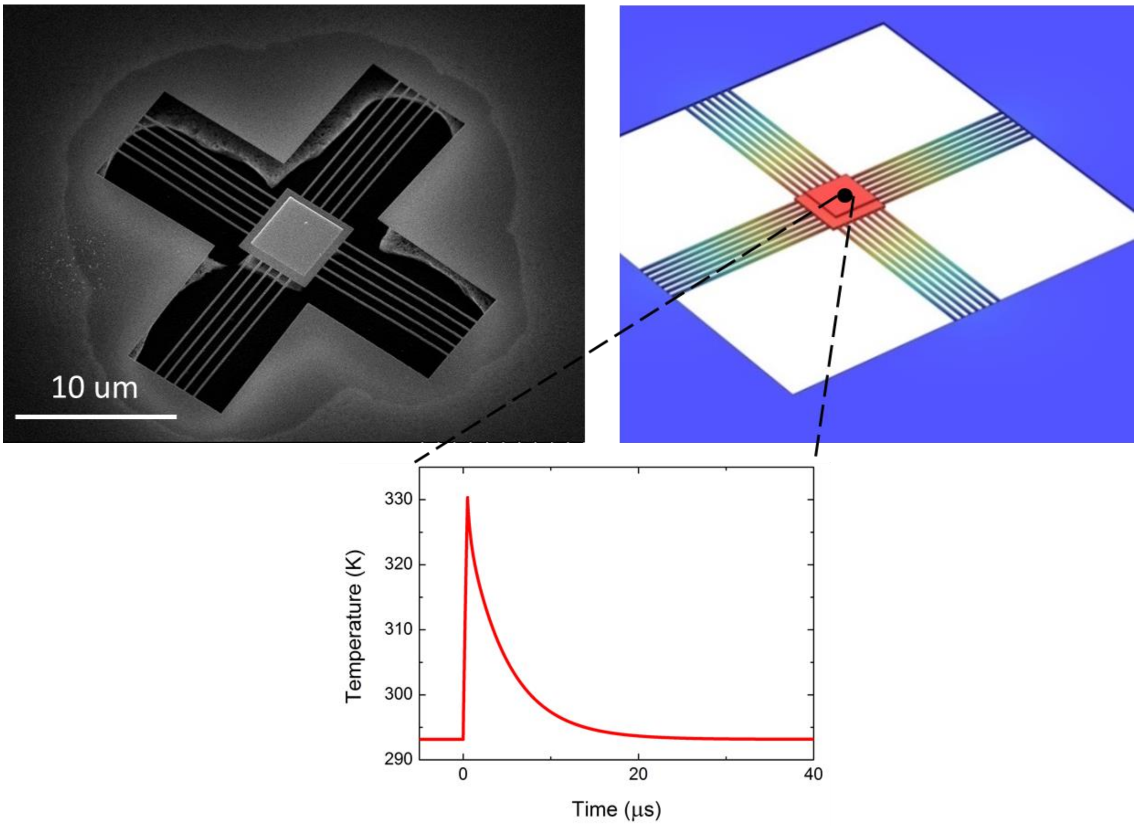

Figure III.14 (left) SEM image of a nanowire nanostructure. (right) 3D model of the measured structure. All size parameters are faithfully taken from SEM images. The picture has been taken during the decay, when heat has started to spread across the structure. (lower) Time dependence of the temperature taken in the center of the metal pad.

The heat transfer model is based on the classical heat transport equation given by:

$$\rho C_p \frac{\partial T}{\partial t} + \nabla . \left(-k \nabla T + \rho C_p T \boldsymbol{u} \right) = Q \tag{3.3}$$

where ρ is the density, C_p the specific heat capacity at constant pressure, k the thermal conductivity and Q contains the heat sources. Considering the diffusivity of the deposited Al and its dimensions, the temperature is considered homogeneous in the pad. Both the measured values and the simulated curves are normalized for convenient comparison.

In these FEM simulations, the only variable parameter is the thermal conductivity of the structure. For the other regions, the κ of the membrane, which value has been measured separately, has been used.

All other parameters need to be set for the temperature of interest. Outside the structure, a Si membrane is simulated, at which borders a fixed temperature is set as a boundary condition. Convection effects, as well as radiation, are neglected.

It is important, in a similar manner as the experiment, that the time steps be small enough to accurately capture the time evolution so it is usually set to 50 to 100 ns. A shorter time step renders the calculation too time-consuming.

Similarly, it is crucial to make the mesh fine enough that it correctly reproduces the shape. A too rough mesh would underestimate the thermal conductivity of the structure. As for a too fine mesh, just like the time step, it makes the calculation too time-consuming.

The simulation, just like the experiment, consists in taking the temporal trace of the temperature inside the Al metal pad. By sweeping over a series of thermal conductivities, it is possible to obtain a batch of decay curves. All these curves are fitted with an exponential decay. The decay times are then plotted versus the thermal conductivity entered as a parameter and an extrapolation curve is drawn between these points.

The experimental value of the decay time is then inserted in this curve and we can extract the value of the corresponding thermal conductivity. This process is illustrated in Figure III.15. The whole fitting process and thermal conductivity extraction is performed thanks to a Matlab program I specifically developed for this purpose.

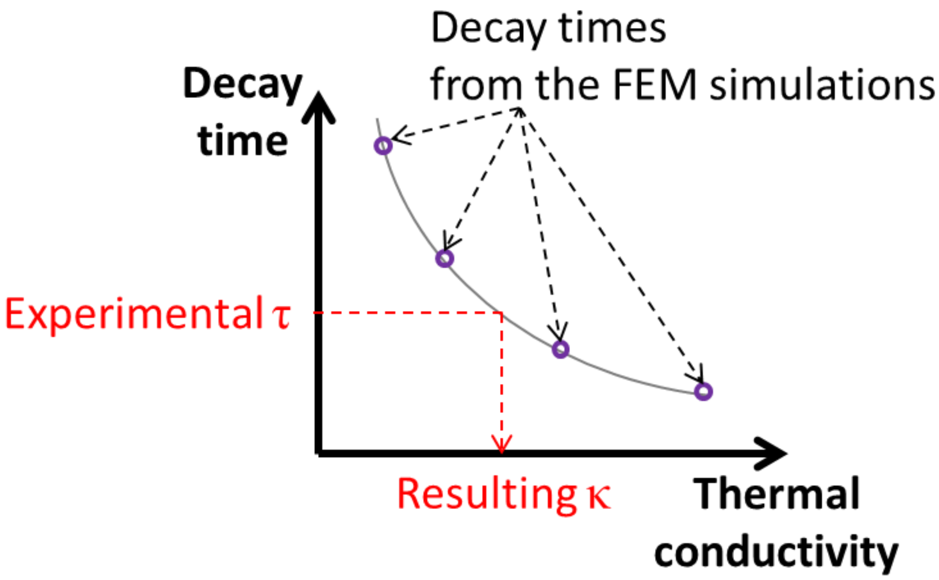

Figure III.15 Thermal conductivity estimation process: Decay times are extracted from the FEM simulations and then linked by an exponential function. The decay time τ obtained experimentally is plugged into this function, giving the corresponding thermal conductivity κ as output.

Chapter IV

Thermal transport in one-dimensional Si nanostructures

In this chapter, we apply our measurement method to two types of nanostructures: first, the simplest suspended nanostructures, i.e., unpatterned thin films, and second, various 1D nanostructures, such as nanowires and fishbone nanostructures. In order to test the measurement system, it is essential to start with simple structures that already have an equivalent in the literature. That is why we chose to use the simple suspended unpatterned thin films [89–93]. Although some more detailed phonons properties than the thermal conductivity have been studied in these structures [46,94–98], measuring the latter not only provides insights about the precision of our measurement; it is also critical for further measurements on more complex structures. Indeed, when measuring other types of structures, it is necessary to include in the model the thermal conductivity of the central Si island as well as the surrounding heat sinks. Thereafter, the nanowires are also compared to the literature, from cryogenic temperature to room temperature, followed by the study of their shape dependence. Lastly, we study thermal conduction in our fishbone nanostructures in a similar manner. This allowed us to point out the differences between nanowires and fishbone nanostructures.

Consistently, the structures have been built as small as possible while maintaining a relatively simple top-down fabrication process. Accordingly, the width of the nanowires was reduced, the smallest width reaching 60 nm. Similarly for fishbone structures, the neck has been minimized, when not adjusted for comparison with nanowires. The dimensions were also chosen for coherent transport purposes (detailed in section IV.3).

IV.1 Suspended Si thin films

The thin films consist of the 145 nm-thick top layer of the SOI wafer, which is etched in a rectangular pattern having a width of 5 µm and a tunable length. Figure IV.1 shows an SEM image of a typical suspended thin film, with the Al pad in its center and the under-etching area visible all around the thin film. Thermal conductivity of such suspended thin films, also called membranes, is known to decrease as its limiting dimension – the thickness – becomes smaller. Indeed, thermal transport in the thin film at room temperature is expected to be purely diffusive, with surface and Umklapp scattering being the main scattering mechanisms (see Chapter II). Surface scattering will occur mostly at the top and bottom surfaces of the thin films, due to its reduced thickness compared to the bulk. The geometry of the surface will have an important impact on the thermal conductivity reduction, all the more so for thinner thin films [99]. Moreover, although the phonons wavelengths are much shorter than the thin film thickness, their MFP in the bulk might well exceed the thicknesses. Thus, the thinner the membrane, the more phonons will be affected by boundary scattering. Our thin films of 145 and 80 nm in thickness have respective thermal conductivities of 75 and 55 Wm^{-1}K^{-1}. These values correspond well to other thin films reported in the literature [59,100–104] as shown in Figure IV.2(a) and corroborate the assumption about the thickness dependence.

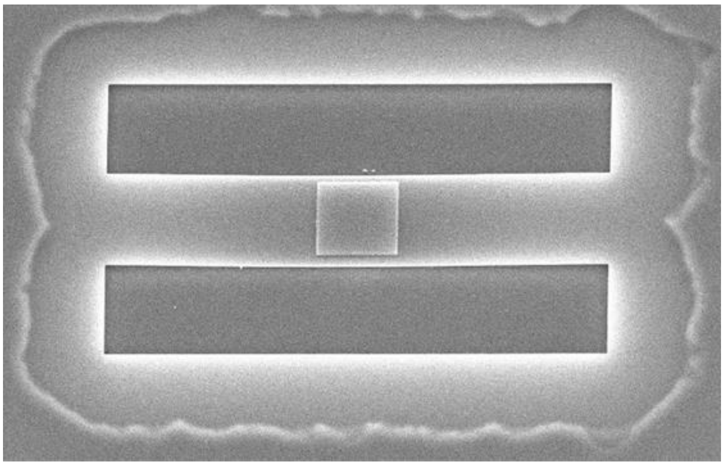

Figure IV.1 SEM image of a suspended unpatterned Si thin film.

In order to further confirm the validity of the measurements, suspended thin films with varying length were measured. According to the above-mentioned diffusive regime, the thermal conductivity must be constant with the length [46]. This corresponds convincingly with the measurements performed on the thin film of thickness 145 nm, shown in Figure IV.2(b). In this case, it can be seen that the thermal conductivities are all contained within the 70-80 Wm^{-1}K^{-1} range. Each of the two samples measured lies within the +/- 6 % error mentioned in the description of the optical measurement system. It is important to note that due to their small decay time, thin films present the largest uncertainty among the structures measured.

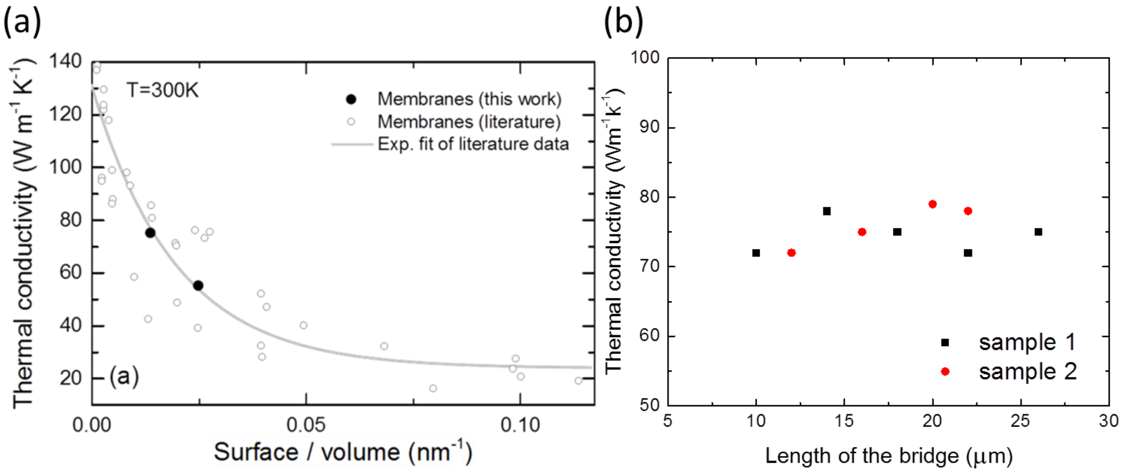

Figure IV.2 (a) Measured thermal conductivity of suspended thin films of various thicknesses, from this work (80 nm and 145 nm thickness) and from the literature. The gray line is a fit of the literature data. (b) Length dependence of the thermal conductivity for a thickness of 145 nm.

In order to further test the experimental setup, the temperature dependence of the thin film thermal conductivity has been taken, and is presented in Figure IV.3 alongside the value from the bulk and other thin films extracted from the literature [105]. Although a full experimental dataset is not available in the literature for thin films of identical dimensions, our values are well between the experimental points of the 100 nm and 420 nm-thick thin films over the whole temperature range. Furthermore, predictions based on calculations provide a very good fit [59,106] to the corresponding experiments in the literature. These results provide solid evidence for the validity of our measurements, even at low temperatures.

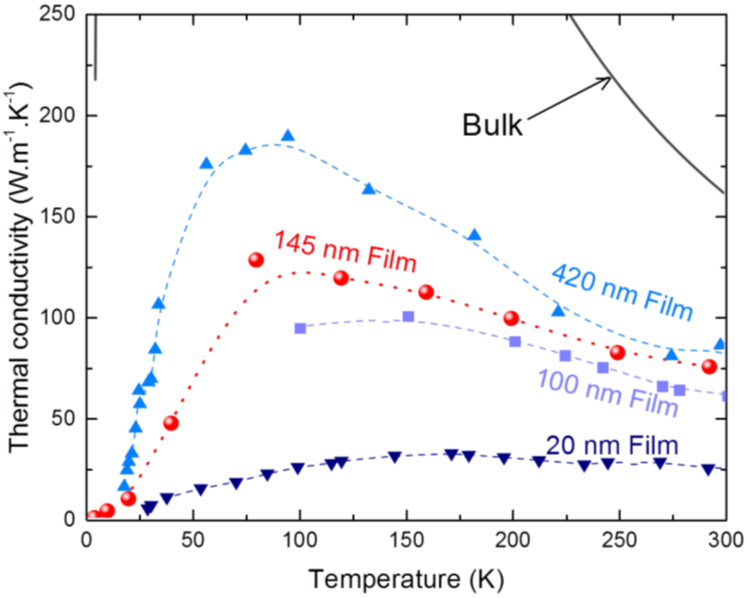

Figure IV.3 Thermal conductivity of the bulk (black line) and the suspended thin film 145 nm in thickness (red) from 4 to 300 K. Other experimental points on 20 nm (down triangle), 100 nm (square) and 420 nm thick thin film (upper triangle) are extracted from the literature[105]. The dashed lines are B-splines and are displayed for clarity.

From this graph, it is possible to observe the different regimes of scattering. The range of predominance of each regime is dependent on the structure under study. The following discussion is developed based on the experimental data on the 145 nm-thick thin film. At high temperatures, i.e. above 80 K, κ decreases as the temperature increases. This is due to a higher rate of Umklapp scattering at higher temperatures. The limit between the low and high temperature regimes, i.e., between the boundary and impurity scattering regime at low temperatures and phonon-phonon scattering at high temperatures is around 80 K for our thin films, while it is around 30 K for the bulk. Below these values, the conductivity of the corresponding material decreases sharply. According to equation 2.6, the thermal conductivity is directly linked to the heat capacity, which in turn decreases with decreasing temperature [107]. Taken together, they represent one of the mechanisms responsible for the diminution of bulk thermal conductivity at low temperatures. However, even for macroscopic samples, boundary scattering is the main cause for the reduction of thermal conductivity. In thin films, the additional reduction observed as compared to bulk is also due to enhanced boundary scattering. It is also expected that with the shift in phonon distribution, the effect of boundary scattering becomes more pronounced as temperature decreases [100], which is supported by our data. At the same time, Umklapp processes become negligible due to the temperature itself. Overall, the experimental data for membranes follow the same trend as presented in Figure II.2.

IV.2 Si nanowires

Succeeding to the extensive study of thin films' thickness dependence, the reduction of a second dimension leads to the study of nanowires, which have also been widely studied in the literature. Si nanowires have been studied for their electrical [108,109], optical [110,111], and thermal [69,112,113] properties and they proved to be good candidates for thermoelectric applications [65,69,114]. Nanowires are most commonly fabricated with a bottom-up rather than a top-down approach and thus present a circular cross-section. Figure IV.4 shows the thermal conductivity of various sets of nanowires from the literature at room temperature as a function of the S/V ratio.

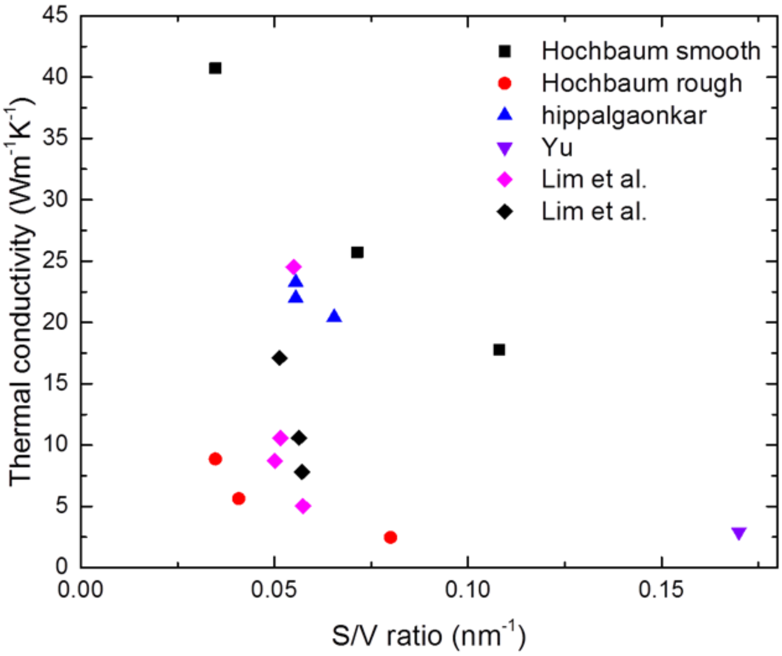

Figure IV.4 Thermal conductivity of various Si nanowires at room temperature extracted from the literature [64,115–117] as a function of the S/V ratio.

The limiting dimension of a nanowire, i.e. the smallest dimension available, is either the diameter of the wire, or its thickness or width in case of a rectangular shaped wire. The values reported here from the literature correspond to nanowires whose limiting dimensions are below 100 nm, but still above 20 nm. The values of thermal conductivity for these nanowires are greatly reduced not only compared to bulk Si, but also to thin films of similar limiting dimension. For nanowires and thin films of similar S/V ratio, although the observation is not as strong as for the limiting dimension, nanowires still display a lower thermal conductivity. The second observation that can be made from this figure is that the values of thermal conductivity vary greatly, i.e. more than one order of magnitude, for nanowires with similar S/V ratio or limiting dimension. Even for nanowires taken from a single study in the literature, the thermal conductivities are hardly similar from one nanowire to another. This suggests that the amount of surface per unit volume is not the sole parameter to cause the reduced thermal conductivity. Both sets of data from Hochbaum *et al*. [115] and Lim *et al*. [117] show that the surface roughness is a determining parameter. As the RMS roughness increases, the thermal conductivity decreases. However, from the measurements done by Lim *et al*. it is clear that when considering surface roughness, both its amplitude and the correlation length are of importance. The conductivity of such nanowires has also been measured down to 20 K and separately as low as a few hundreds of mK [61–63].

In this work, the nanowires have been etched from the top layer of an SOI wafer and consequently, have a rectangular cross-section with a fixed thickness of 145 nm. Figure IV.5 shows an SEM image of a suspended nanostructure with 10 nanowires (left) and a 3D representation of the same structure (right) used in the FEM simulations to extract the thermal conductivity, with the colors representing the temperature map during the cooling process.

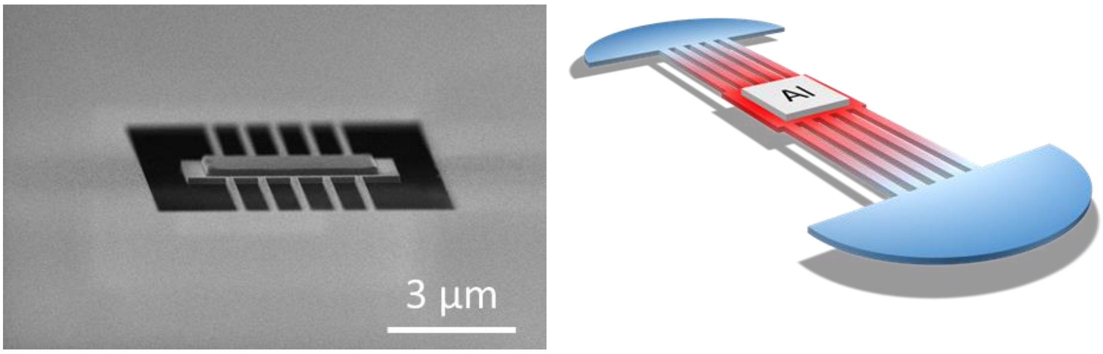

Figure IV.5 (a) SEM image of a nanowire nanostructure. (b) Schematic of the suspended nanowires structure with the Al pad heater in its center. The color gradient represents the temperature during the thermal dissipation process. The temperature in the square Si island under the Al pad is considered uniform.

The study about nanowires in this work can be divided in two parts. First, the focus is placed on the thermal conductivity as a function of the width of the wires, starting from room temperature and going down to 10 K. Then, we tune the other possible dimension, i.e. the length of the wire, at room temperature at first, and then at 4 K, in order to observe a change in the phonons' transport, from purely diffusive, in which regime the thermal conductivity is independent of the length, to partially specular.

IV.2.1 Si nanowires of different width at room temperature

While it is not possible in our case to reduce the thickness, it is nonetheless possible to study the width dependence of the thermal conductivity which has been done at first at room temperature. Similarly to reducing the thickness of a thin film, reducing the second dimension, i.e. the width, should display a comparable trend in the diffusive regime. Indeed, as observed from Figure IV.6, thermal conductivity decreases with decreasing width. The measurement not only indicates that κ decreases with decreasing width; it also reveals that this diminution intensifies as the width is reduced. This trend is further supported by some theoretical investigations [118].

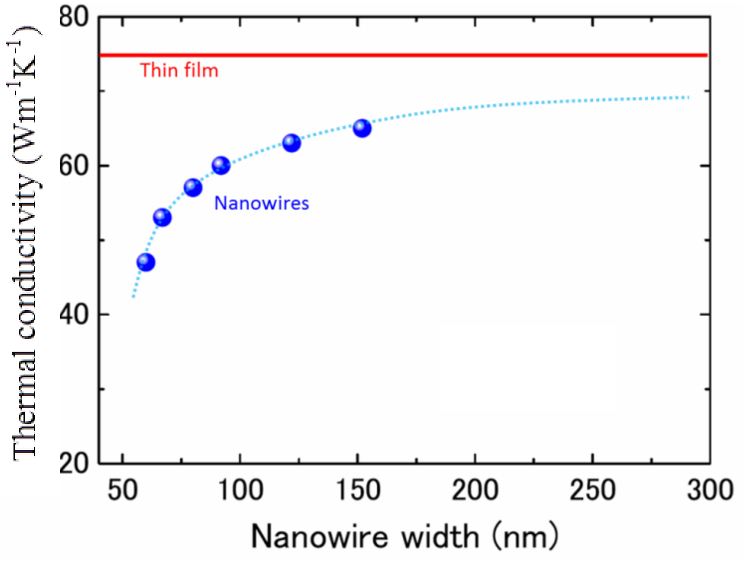

Figure IV.6 Nanowire thermal conductivity for different widths at room temperature (blue) with a polynomial fit (blue dashed line) and the value of the thin film thermal conductivity (red).

IV.2.2 Si nanowires of different width below room temperature

Following the previous room temperature measurements, the temperature dependence of the thermal conductivity has been measured from 20 K to room temperature. Since the phonon MFPs are modified with temperature, i.e. become longer at low temperatures, it is expected again that boundary scattering will take an increasingly important role in the thermal conductivity reduction.

Similarly to the membrane, the temperature-dependent thermal conductivity of nanowires is consistent with the literature, as can be observed from Figure IV.7(a). Although a direct comparison is difficult since our nanowires have a rectangular cross section, the measured conductivities prove highly consistent with the literature data over the whole range of temperatures. The maximum of thermal conductivity is reached at a higher temperature than for the thin film, around 150 K. This temperature at the maximum of thermal conductivity further increases with decreasing width of the wire. Moreover, as can be seen from the figure, this peak is virtually negligible for large nanowires and even nonexistent for the thinnest one. This is due to the fact that even at room temperature, boundary scattering plays an important role, which gets bigger as phonons are confined in a smaller cross section. If we compare the thermal conductivities of nanowires to that of the thin film, we can observe (Figure IV.7(b)) that the relative conductivity, i.e. the conductivity of a given wire divided by that of the thin-film of same thickness, decreases, even below 80 K. The maximum reduction can exceed 80% in most of the nanowires from our study and occurs below 50 K. A similar trend can be observed when comparing the thermal conductivities of nanowires to that of the widest one.

These results show that as the temperature decreases, an increasing amount of thermal phonons, i.e. phonons carrying heat, are impacted by the reduced width, whether the relative thermal conductivity is taken as compared to the thin film or to a larger nanowire. Although this result gives an indication about the length scales that affect phonons, it is not sufficient to determine the contribution of phonons depending on their MFP. To achieve this, there are two possible solutions. The first one is to use the grating method on a suspended thin film. This method consists in changing the length through which phonons can freely travel in a material by creating a periodic interference pattern within this same material. Varying the grating length, as has been done by Johnson *et al*. [46] at room temperature, allows one to cut specific ranges of phonons MFPs and thus get back to the accumulated conductivity. The other method consists in directly fabricating circular nanowires with a great range of radii. Both of these solutions are currently not applicable; thus the precise phonon distribution cannot be experimentally deduced by using nanowires or a membrane in this work.

Interestingly, it seems that at very low temperature, i.e. below 40 K, the relative thermal conductivity to the membrane is increasing again. No explanation for this phenomenon has been found so far.

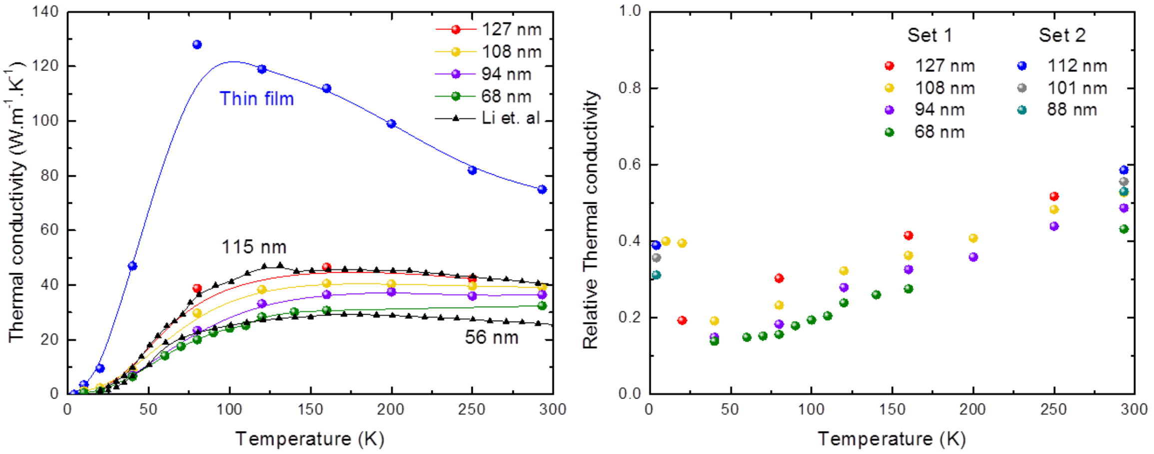

Figure IV.7 (a) Temperature dependence of the thermal conductivity for the unpatterned thin film and nanowires of different widths between 10 and 300 K. (b) Calculated relative thermal conductivities of the nanowires as compared to the thin film. The missing values of the thin film thermal conductivities have been interpolated.

IV.2.3 Si nanowires of different length at room temperature

Apart from the width, the only other modifiable geometrical parameter is the overall length of the nanowires. As for the membranes, this also allows to verify the diffusive nature of heat transfer at room temperature. A set of nanowires with constant width but lengths ranging from 1 to 20 µm was thus fabricated. In the diffusive regime, it is expected that the thermal conductivity (the thermal decay time) should be constant (respectively linearly increasing) with the length of the wire [119].

The measurements were performed on nanowires with width of 88 and 101 nm and length ranging from 1 to 20 µm. Figure IV.8(a) shows the temperature decay time as obtained directly from the experimental measurement system as well as a linear fit. It is clear that this decay time follows a linear trend. To confirm the diffusive nature of thermal transport at room temperature, we calculated the effective thermal conductivities, which are plotted in Figure IV.8(b). For the nanowires of width 88 nm, the thermal conductivity is clearly constant with length within the uncertainty region. The variations observed for the other nanowires, i.e., with widths of 101 nm, are due to several factors related to the fabrication. First, the neck of the nanowires might not be perfectly constant along the length of the wire, albeit still not clearly noticeable by SEM. Additionally, from one nanowire structure to another, small variations in the width or regularity of the side walls, i.e. how straight the walls are over the entire wire length, can appear, even though they were fabricated on the same chip. Nonetheless, even in the case of the nanowire of width 101 nm, the thermal conductivities remain within a +/- 6% region.

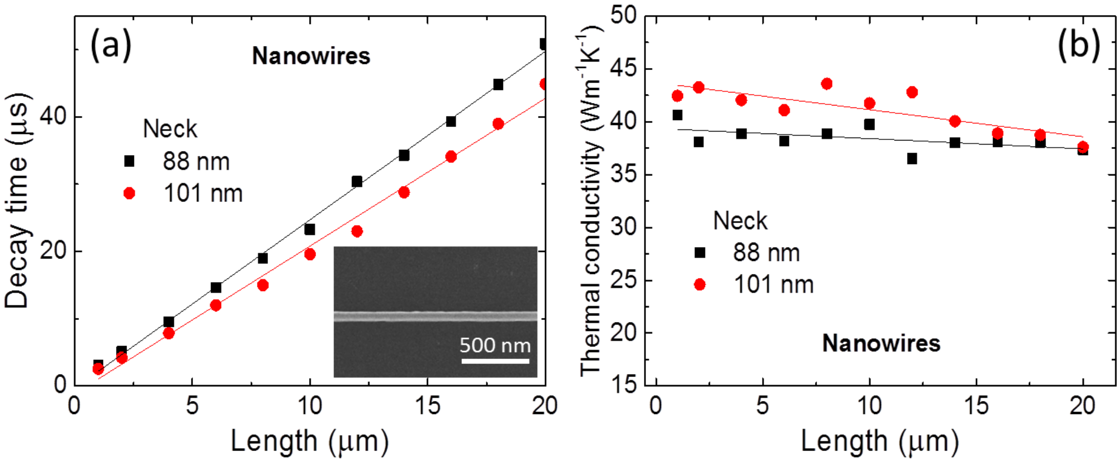

Figure IV.8 Room temperature measurement of 2 nanowire sets with varying length. Points are experimental data while lines are linear fits. (a) Decay times as obtained from the optical measurement system. (Inset) SEM image of a single nanowire. (b) Effective thermal conductivity obtained from 3D FEM simulations.

These results suggest that thermal transport in rectangular shaped nanowires is indeed diffusive at room temperature, since there is no visible dependence of thermal conductivity on the length of the wires. It also shows that in the case of 1D structures, a linear increase in decay time does indeed correspond to a constant conductivity.

IV.2.4 Si nanowires of different length at 4 K

Since we know that phonon MFPs, as well as phonon wavelength, become longer for lower temperatures, it is possible that heat transport in nanowires at very low temperatures deviate from the diffusive transport regime that was just confirmed at room temperature. In order to ascertain this with our experiment, the previous set of nanowires with different lengths was then measured at 4 K in a similar way to room temperature. At room temperature, the thermal conductivity was independent of the length, which is characteristic of the diffusive heat transport regime. In Figure IV.9, the thermal conductivity of these same nanowires is plotted at 4 K. The same trend, i.e., constant thermal conductivity, can be seen for nanowires which length is bigger than 4 µm. However, as the length of the nanowires is decreased below 4 µm, it seems that the thermal conductivity starts to decrease. This is an indication that thermal transport in these nanowires is partially ballistic [119].

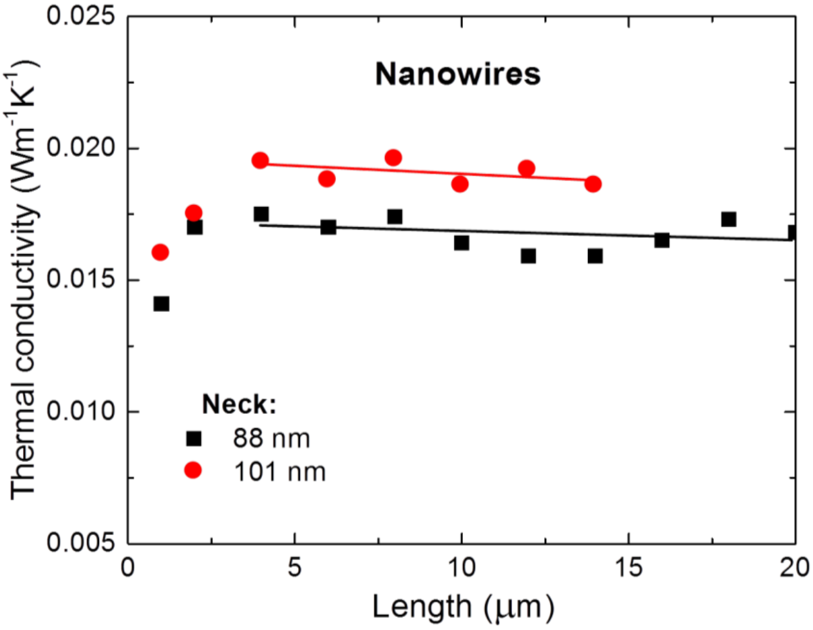

Figure IV.9 Low temperature measurements of nanowires with different lengths for two sets of nanowires of width 88 (black) and 101 nm (red).

This result suggests that some phonons MFP might be longer than the overall length of the wire. Such ballistic transport has been observed before [119,120], although, in rectangular Si nanowires at 5 K, the thermal conductance was much lower than the expected fully ballistic conductance [61,62], suggesting that diffusive transport still play an important role [121]. Our results corroborate these observations. Therefore, we can conclude that in nanowires shorter than 4 μm, thermal transport might be partially ballistic in rectangular Si nanowires with width on the order of 100 nm at 4 K.

IV.3 Fishbone periodic nanostructures

Both thin films and nanowires had previously been studied in the literature. However, 1D periodic nanostructures are quasi-nonexistent in published research. With the aim of highlighting the appearance of a coherent contribution to heat transport, we studied periodic structures displaying small feature sizes, hereafter called fishbone nanostructures.

For photonic crystals, the periodicity is introduced in the refractive index of the material. In case of phononic crystals, the corresponding parameter for phonons would be the mass, and the impact of coherent phonon scattering can be expected in structures with a periodically changed mass. Figure IV.10(a) shows an annotated SEM image of a fishbone nanostructure with its dispersion relation displayed alongside that of a nanowire in Figure IV.10(b). From the band diagram, it is clear that the group velocity $(d\omega/dk)$ of phonons will be reduced in this type of structures. Although the band diagrams have been plotted only up to 30 GHz for clarity, the reduction is still valid for higher frequencies. This should result in a decrease of the heat flux in this structure as explained in Chapter II. The dimensions have been reduced as much as possible, which has had the effect of enhancing incoherent scattering. Some structures have also been designed to be compared to nanowires of similar neck width. However, the main reason for the choice of the dimensions lays in the wave properties of these fishbone structures.

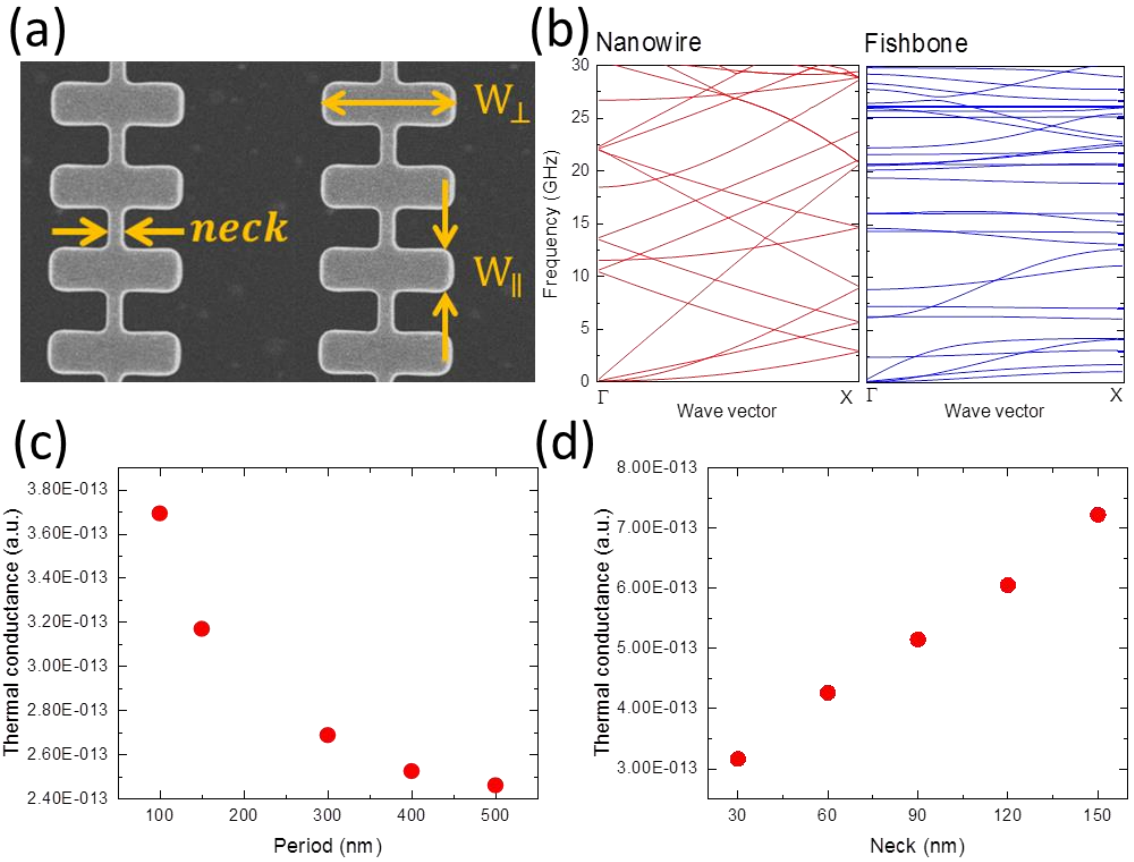

Figure IV.10 Fishbone nanostructure as compared to a nanowire. (a) SEM image of a fishbone nanostructure with relevant parameter names. (b) Band diagram of a nanowire (red) and a fishbone structure of identical neck width (blue) The width of the neck is 30 nm while for the fishbone structure, the period is 150 nm and $W_\perp$ is equal to 300 nm. (c) Power flux as a function of the period in the coherent regime. As the period increases, the total heat flux decreases. The neck is 30 nm wide, $W_\perp$ is equal to 300 nm and $W_{//}$ equals half the period. (d) Heat flux as a function of the neck width for fishbone structures of period 150 nm and $W_\perp$ is equal to 300 nm.

From a coherent point of view, a balance is to be found. It was shown for 2D PnCs that the bigger the period, the bigger the reduction in thermal conductance [41]. This also applies to fishbone structures as shown in Figure IV.10(c). However, smaller periods are expected to display coherent effects at higher temperatures, as phonons do not need to travel as long a distance to feel the periodicity as if the period was larger. This last factor was decisive in the choice of the period. In the case of fishbone nanostructures, the lowest period achieved with satisfying fin shapes was 150 nm, after optimization of the fabrication process. From Figure IV.10(d) it is also clear that the smaller the neck width, the lower the thermal conductance. From an incoherent point of view, reduced dimensions imply a lower thermal conductivity via surface scattering. Thus both the neck width, reduced as much as possible, provides both enhanced coherent and incoherent scattering.

While these fishbone nanostructures are interesting from the point of view of coherent reduction of thermal conductivity, their interest also lies in the tunable thermal properties by adapting the shape [118,122]. To assess the precise impact of the shape on the thermal conductivity, we designed various structures whose properties will be discussed in the next subsections.

First, the focus is put on the neck width, which leads to a comparison with a nanowire of similar neck, both at room temperature and 4 K. Then the other shape parameters, i.e., $W_{//}$ and $W_{\perp}$, are studied at room temperature. Next, the study progresses towards lower temperatures, between 10 and 300 K, in order to investigate any change in the heat transport behavior below room temperature. Following this, the impact of the total length of the fishbone nanostructures on thermal conductivity is studied at room temperature first, and then at 4 K, followed by a comparison between the behaviors at these two temperatures. Lastly, this chapter provides a general conclusion on heat transport in fishbone nanostructures.

IV.3.1 Fishbone PnCs of different neck at room temperature

From a geometrical point of view, fishbone PnCs are nanowires on which side fins have been periodically added. Thus, it can be expected that the central part, i.e., the neck, will play a key role in thermal transport in these PnCs, just as it does for the nanowires. Although no coherent effect of the periodicity is expected at room temperature, its appearance would only enhance the role of the neck, as was shown in Figure IV.10(d). Figure IV.11 shows the thermal conductivity of fishbone PnCs of varying neck widths at room temperature. It demonstrates an increase in thermal conductivity as a function of the neck width, very similar to that of nanowires (see Figure IV.6). This variation in thermal conductivity also becomes steeper as the neck is reduced. This was already observed in nanowires and, thus, the side fins might have no impact on it. However, it is interesting to observe that the conductivity is slightly lower for the structures with a larger value of $W_{//}$, which indicates that the fins do have an impact on the absolute value of the thermal conductivity. This tendency is further developed in the following IV.3.3 subsection.

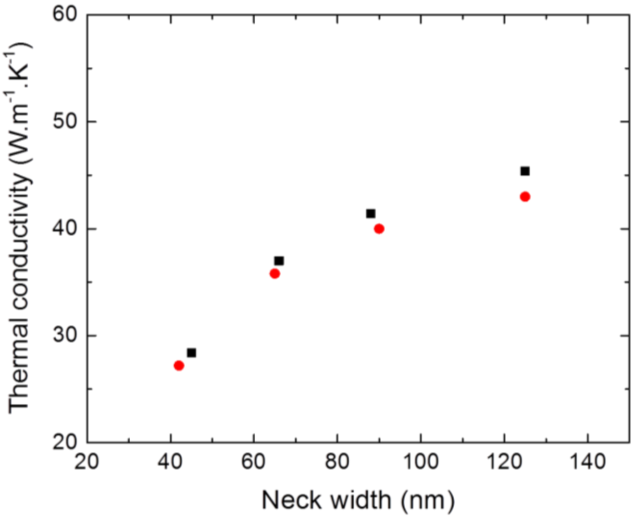

Figure IV.11 Thermal conductivity of fishbone nanostructures at room temperature. The two sets of data are for $W_{//}$ ~ 130 nm (black) and 180 nm (red). The period is fixed to 300 nm.

IV.3.2 Fishbone PnCs versus nanowires

To clearly demonstrate the impact of the periodic additions on the thermal transport in one-dimensional structures, we compare the data obtained on the nanowires and fishbone PnCs with the same neck width. However, in order to properly compare fishbone structures to nanowires, it is necessary to fabricate them on the same chip as the absolute thermal conductivity might fluctuate from one chip to another. Such structures have been fabricated and their thermal properties are shown in Figure IV.12. We can see from Figure IV.12(a) that the decay time is shorter in fishbone structures than in nanowires of similar neck at room temperature. Since decay time and heat flux are inversely proportional, the overall heat flux is stronger in fishbone structures. This can easily be explained by the side fins. Indeed, due to their initial temperature, these side fins will act as small heat sink, thus “absorbing” part of the heat that has been dissipated from the heater and hastening the central island temperature decay.

However, the thermal conductivity is similar to that of the nanowires. While for shorter lengths fishbone structures display a slightly higher thermal conductivity, the trend is inverted when the structures are longer than 15 μm. This phenomenon will be explained in a subsequent subsection. The observation made for shorter structures, i.e., a slightly higher conductivity for the fishbone structures, has been confirmed on another sample with different dimensions at room temperature.

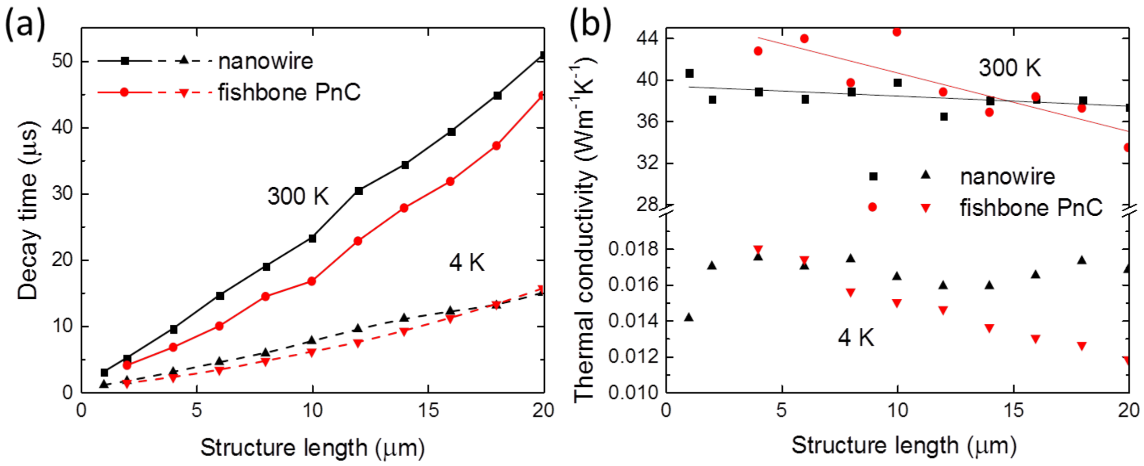

Figure IV.12 Comparison between nanowires and fishbone structures of same width. (a) Decay times of both structures at room- and low-temperature and (b) corresponding thermal conductivities at the same temperatures.

At low temperatures, the observations are similar to room temperature for most of the lengths considered here: we observe a higher thermal conductance for the fishbone structures and a thermal conductivity at the same level as that of nanowires. However, for long structures, i.e., close to 20 μm, two main differences appear. The first one is that the thermal conductance of fishbone structures becomes similar, and even slightly smaller than that of nanowires. The second is that the thermal conductivity reduction in fishbone structures becomes more distinct at low temperature, i.e. the thermal conductivity is reduced by as much as 30%. It is interesting to note that despite the identical neck and increase in the total volume of matter in fishbone structures, the total conductance does not stay higher than for the nanowires. The decrease in thermal conductivity associated with this trend will be explained in the subsequent sections.

However, it is possible to explain the differences in thermal conductivity at room- and low-temperature partially by the specularity of boundary scattering. We asked Dr. T. Hori to simulate both nanowires and fishbone PnCs of similar neck. In Figure IV.13 are displayed the thermal conductivities of these two structures for different values of the specularity parameter p. Although the simulations have been performed at room temperature, since the only parameter varying is the specularity parameter, it is still possible to compare these two types of structures even at low temperature. When p=0, i.e., where boundary scattering is purely diffusive, there is virtually no difference between the thermal conductivity of nanowires or fishbone structures.

This result is consistent with the experimental results at room temperature, where phonon transport is mostly diffusive. From the MC simulations, we can see that the higher the specularity parameter, i.e., the more specular the boundary scattering, the bigger the difference in thermal conductivity between the two types of structures. For purely specular scattering, the thermal conductivity is reduced by as much as 40% in the fishbone structures compared to the nanowires. Since the simulation is performed in a unit cell, the result is given for an infinitely long structure and thus can more easily be compared to our longer structures than the short ones. In that case, we can see that at low temperatures the thermal conductivity is lower in fishbone structures in the experiment, thus further confirming the partially specular nature of boundary scattering at 4K. At room temperature on the other hand, the experimental difference is very small, again going along with the simulation results.

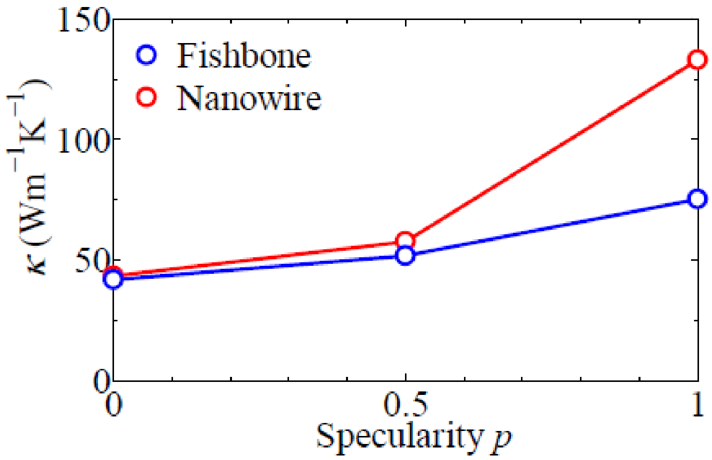

Figure IV.13 Effect of the specularity parameter p on the thermal conductivity of rectangular cross-section nanowires (red) as well as fishbone PnCs (blue) calculated by MC simulations at room temperature. The period is 300 nm, the neck width 100 nm for both the nanowires and the fishbone structures. $W_{//}$ = 100 nm and $W_{\perp}$ = 300 nm.

IV.3.3 Shape of the side fins: $W_{//}$ and $W_{\perp}$ dependence

In the previous subsection, we proved that fishbone structures behave in a similar fashion to nanowires, with the neck width being a crucial parameter in the transported heat flux and the fins causing a decrease in thermal conductivity at low temperature. Even at room temperature, the conductivity is very marginally lower in the fishbone PnCs according to the MC simulations. To elucidate in more details the impact of the fins, we changed their sizes independently of each other, both in the heat flux direction and perpendicular to it, i.e., $W_{//}$ and $W_{\perp}$ respectively, and independently of the neck width.

First, let us focus on the dimension in the direction of the heat flux, i.e., $W_{//}$. In the limit where it is equal to 0, we should reach the heat flux, and thus the thermal conductivity, provided by the nanowire of width equal to the neck. On the other hand, when it is equal to the period, we have a nanowire of width equal to $W_{\perp}$ and thus a much higher heat flux. However, if there is even a small constriction, i.e., $W_{//}$ < period, then we can expect that most of the heat flux will be dominated by this constriction [123–125]. Indeed, when measuring the values of the thermal conductivity for different values of $W_{//}$, and that for 2 set of structures with different neck width, we observe (see

Figure IV.14(a)) that the thermal conductivity is decreasing with the increase in $W_{//}$. In a similar way, when performing MC simulations (detailed in chapter II), we encounter the same trend. The decrease observed between the nanowire and the largest available $W_{//}$ exceeds 5%.

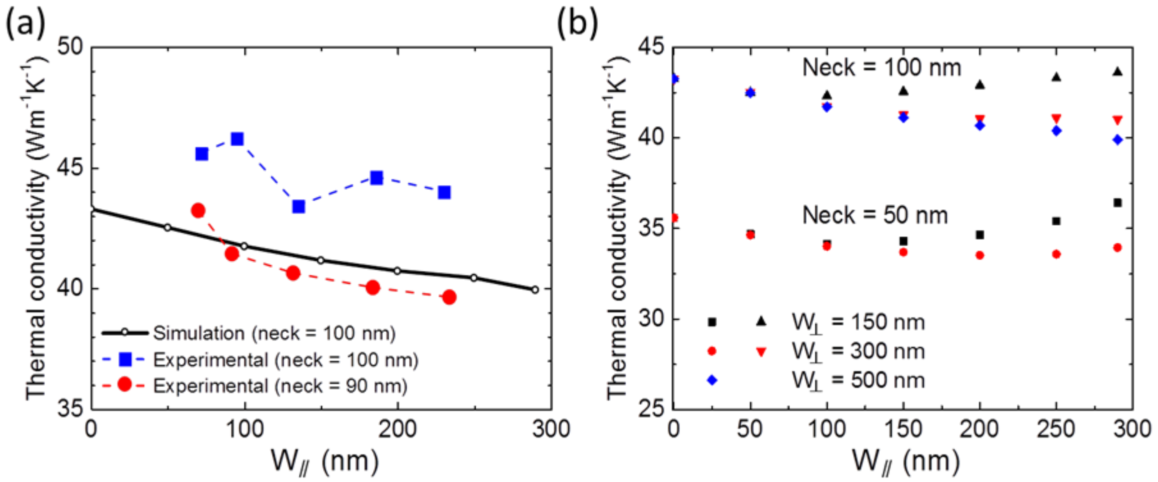

Figure IV.14 Dependence of the thermal conductivity in fishbone structures. (a) Experimental (blue and red) measurement versus MC simulations (black). (b) MC simulations at room temperature for structures of period 300 nm as a function of the different geometrical parameters.

Some further information can be extracted from the MC simulations. Indeed,

Figure IV.**14**(b) shows that there is an interdependence between the parameters $W_{//}$ and $W_{\perp}$. In the experimental results displayed, the value of $W_{\perp}$ is large enough, i.e., > 450 nm, so that the thermal conductivity continues decreasing when $W_{//}$ increases. However, the simulations shows that if $W_{\perp}$ is small enough, the thermal conductivity will increase again for large values of $W_{//}$. Although the experiment has not been conducted for the dependence on $W_{\perp}$, it is still possible to observe variations in the results provided by the MC simulations. Figure IV.15 shows the changes in thermal conductivity for a fixed $W_{//}$ and variable $W_{\perp}$ in two sets of different neck. There are two points worth noting from these simulations:

First, whatever the geometry of the fins, when the neck is greatly varied, the thermal conductivity is totally dominated by this parameter. This corroborates our observations presented above.

Secondly, the thermal conductivity decreases with $W_\perp$ without getting higher for large values. Indeed, when $W_\perp$ gets larger, more phonons are "trapped" inside. Above a certain depth value, the conductivity stabilizes. At that point, all the phonons that could enter into the side fins have done so and increasing the depth just adds useless material which will not be reached by incoming phonons.

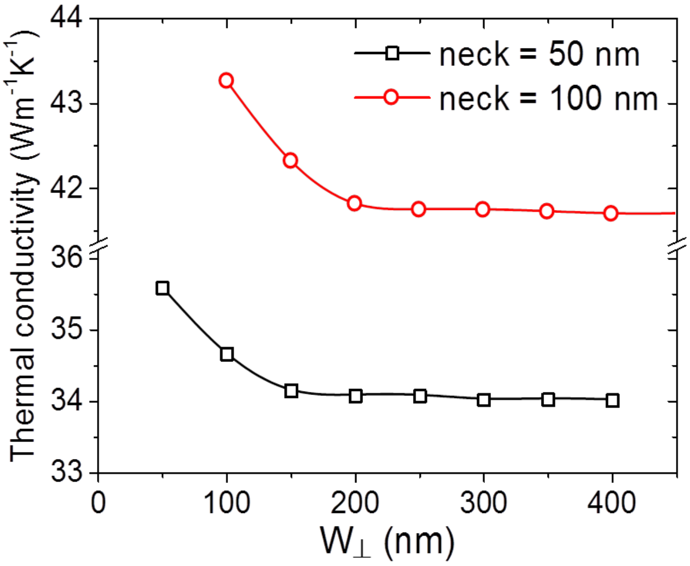

Figure IV.15 MC simulations of thermal conductivity in two sets of structures with periods of 300 nm, necks of 50 and 100 nm, $W_{//}$ of 150 nm and varying $W_\perp$.

IV.3.4 Fishbone PnCs between 10 and 300 K

Using a similar procedure to the one we used with nanowires, we now study the impact of the neck width between 10 K and room temperature, followed by the impact of $W_{//}$ in the same temperature range. We define the relative thermal conductivity of a structure by its conductivity divided by that of the structure with the highest conductivity in the set.

Figure IV.16(a) shows the temperature dependence of the thermal conductivity for various neck widths. The dashed line denotes the limit between the "low" and "high" temperatures, with Umklapp scattering impacting the conductivity in the high temperature region. The trend observed is similar to that of nanowires. We can also observe that the relative thermal conductivities decrease as the temperature decreases, as can be seen from Figure IV.16(b).

Within this set of data, the difference between the structures increases by approximately 10% of the largest fishbone structure conductivity. The conductivity can be reduced by 30% when the neck width is divided by 2, from 122 nm to 65 nm, while for the same structures this reduction is only 20% at room temperature. Similar observations from the other structures yield the same conclusion. Decreasing the neck width strongly impacts thermal conductivity whatever the temperature. In this series of structures, it seems again that the relative thermal conductivity reaches a minimum around 40 K and starts to converge below that. The reason for this observation is still unclear.

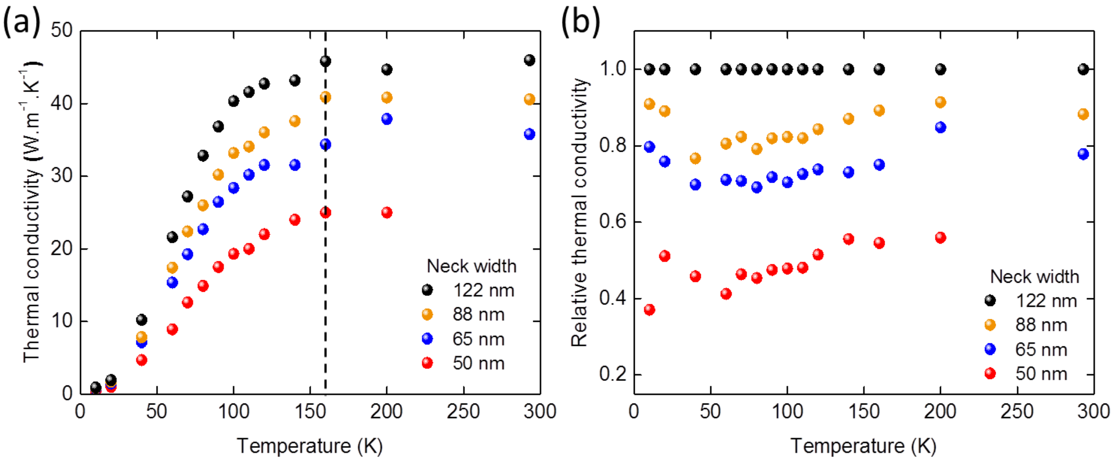

Figure IV.16 Fishbone structures with varying neck width at temperatures ranging from 10 to 300 K. (a) Thermal conductivity for 4 sets of fishbone structures with period of 300 nm and $W_{//}$ of 140 nm and ($W_{\perp}$- neck width) = 388 ±5 nm, versus temperature. (b) Thermal conductivity of the same structures relative to that of the largest neck width.

Next, we investigate the impact of $W_{//}$ in the same range of temperatures. The observation is also very similar: The difference between different values of $W_{//}$ is increasing when the temperature is decreasing (Figure IV.17(b)). For a two-fold increase in $W_{//}$ from 70 to 234 nm, the difference increases from approximately 5% to 15% and for a threefold increase in $W_{//}$ from 8% to more than 20%. While it might be that this decrease is inverted below 40 K, which might be due to the shift in phonon spectrum, with long wavelength phonons not feeling the fins, while they play an ever increasing role in thermal conduction, the lack of experimental points makes any conclusion unclear.

For such structures, the temperature dependence of thermal conductivity on the different geometrical parameters did not yield any significant conclusion on thermal transport, given that the same trends seem to be applicable across the whole range studied here. Still, it should be noticed that as the temperature decreases, the differences that arise due to geometrical differences get more pronounced. Further experiments have thus focused on other parameters at 4 K, where different physics, with an increase in specular scattering and possible coherent scattering, might apply.

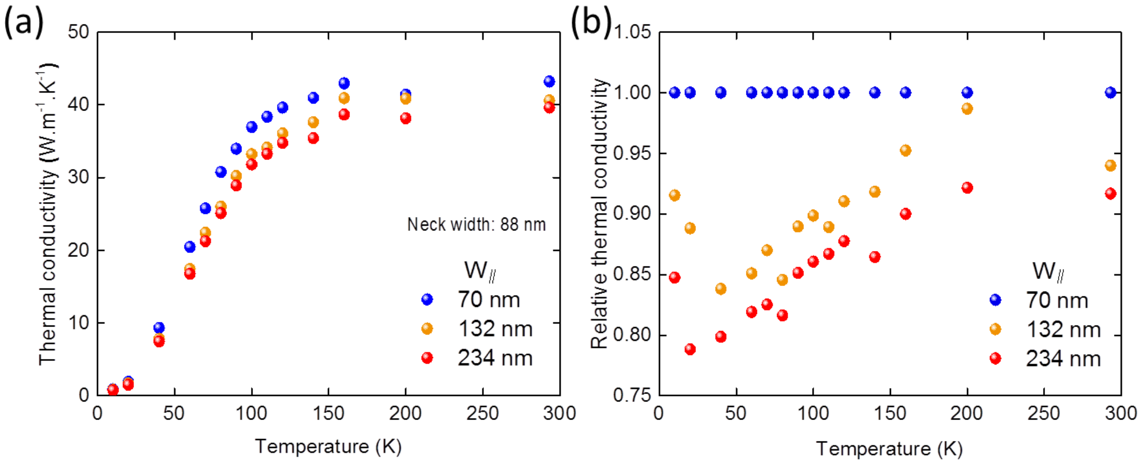

Figure IV.17 Fishbone structures with varying $W_{//}$ at temperatures ranging from 10 to 300 K. The period is 300 nm and $W_{\perp} = 474 \pm 4$ nm. (a) Thermal conductivity for 3 sets of fishbone structures versus temperature. (b) Thermal conductivity of the same structures relative to that of the smallest $W_{//}$.

IV.3.5 Fishbone PnCs of different length at room temperature

In the previous subsections, we have demonstrated that heat transport is indeed diffusive at room temperature in our various suspended structures. Since the fabrication process does not change, the surface roughness of fishbone structures is similar to that of nanowires, which suggests that if no coherent scattering is observed, then incoherent diffuse scattering should be able to explain the thermal conductivity of fishbone structures. This was the case at room temperature for the fin shape dependence. However, when varying the length of the structures, i.e., increasing the number of periods, decay times increase, faster as length increases and thermal conductivity decreases with length, as can be seen from Figure IV.18(a) and (b,c), respectively. The decrease in thermal conductivity can exceed 30% when comparing short structures, i.e., below 5 µm, and long ones of 20 µm. A possible explanation for this phenomenon is that the side fins provide additional scattering surfaces, which are estimated to reflect part of the phonons backwards, thus creating a transmission function. When the structures are long enough, phonon might be somewhat trapped by these successive reflections, far away from either heat sink. In the literature, similar structures that have also been presented as constrictions in nanowires yield an unchanged conclusion.

Moreover, it seems that, from the measurements of various sets of structures with varying neck widths, regardless of the side fins geometry, the smaller the neck, the bigger the decrease in thermal conductivity with length. This suggests that a bigger portion of phonons enters the fins as the neck width is reduced. Or inversely, if the neck is large enough, the side fins will have a negligible impact on thermal conduction. This suggests once again that the neck width is one of the main parameters affecting the thermal conductivity.

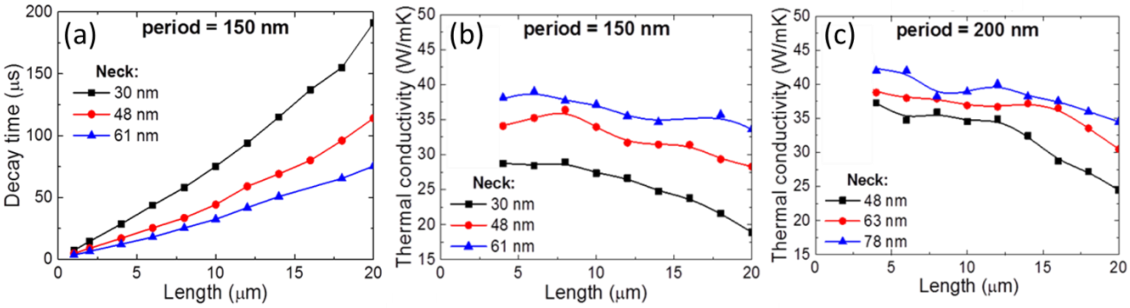

Figure IV.18 Length dependence of the thermal properties of fishbone nanostructures. $W_{//}$ is equal to half the period while $W_{\perp}$ is 455 and 470 nm for the structures of period 150 and 200 n respectively. (a) Decay times for 3 sets of structures with period 150 nm and varying neck and length. (b) Corresponding thermal conductivities for the same structures and (c) similar structures with period 200 nm.

IV.3.6 Fishbone PnCs: 4 K versus room temperature

At room temperature, there is no visible correlation between the thermal conductivities of fishbone structures with identical neck widths but different periods as a function of the length. However, at 4 K, the tendency is identical for all periods as long as the other geometrical parameters remain identical, as shown in Figure IV.19(a), i.e., the decrease in thermal conductivity as the length increases is similar for the three sets of structures, regardless of the period. The differences in absolute value might stem from the small differences in the neck width and total volumes ($W_{\perp}$ is slightly larger for larger periods but the difference is inferior to 6%), as shown for nanowires at room or low temperatures. If the thermal conductivities relative to that of the longest period were plotted, we could see that the difference between periods slightly increases as the total length increases. This suggests that the heat transmitted per unit length is suppressed more efficiently by increasing the number of periods rather than by decreasing the transmission in a single period. However, the differences that appear in the thermal conductivities at any given length are still smaller than the differences in the decay times as shown in Figure IV.19(b).

Indeed, even though on Figure IV.19(b) it appears clearly that the tendencies are also the same for the different periods, the values of the decay times, and thus the total conductance, differ by as much as 50%. Since $W_{//}$ is equal to half the period, the total volume of matter for the different periods, especially for long PnCs, should not be able to account for the difference in decay times, which calls for a more thorough investigation. Similar tendencies for the thermal conductivities and decay times, are observed for different periods with slightly larger neck, i.e., 60 nm.

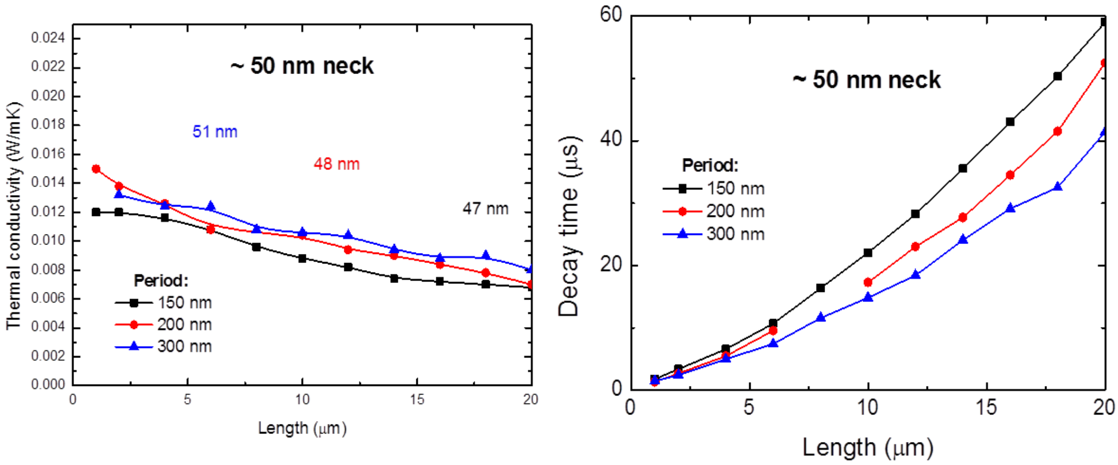

Figure IV.19 Thermal properties of fishbone PnCs with a neck width about 50 nm at 4 K. (a) Thermal conductivity of fishbone structures with three different periods and (b) thermal decay times of these same structures.

Since there seems to be a noticeable difference between the behaviors at room temperature versus 4 K, we compare the conductivities of two periods at these temperatures. In Figure IV.20, we plot the relative thermal conductivity at these two temperatures for two sets of structures with periods of 150 and 300 nm. The relative conductivity is calculated by:

$$\text{Relative conductivity} = \frac{\kappa_{150} - \kappa_{300}}{\kappa_{300}} \qquad (4.1)$$

with κ_{150} the conductivity for the period of 150 nm and κ_{300} that of the 300 nm period. At room temperature, this ratio increases with length, suggesting that the transmission per period is lower in the structure with the longer period. Again this can be explained by the difference in the width of the fins, which is equal to half the period in any structure. Thus, the longer period has a lower transmission function due to its larger fins. Although in the structure with a period of 150 nm, the number of periods is larger, it does not compensate the thermal conductivity dependence observed over $W_{//}$, i.e., a decrease in thermal conductivity as $W_{//}$ increases.

At 4 K however, the tendency is inverted. This means that possessing a greater number of periods is more advantageous than presenting a single period with a lower transmission function.

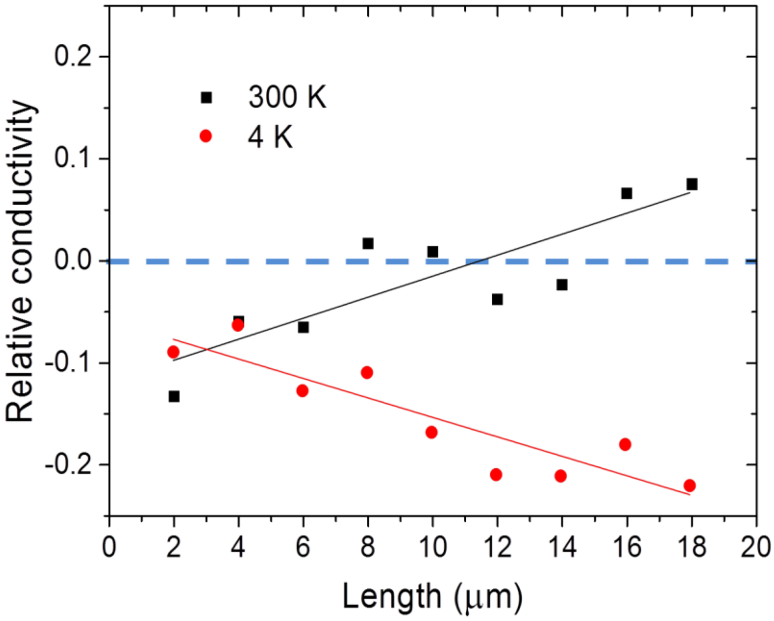

Figure IV.20 Relative thermal conductivities of two sets of fishbone PnCs with a period of 150 and 300 nm. Measurements were performed both at room (black) and low temperature (red).

IV.3.7 Conclusion on observed fishbone heat transport

In this chapter, we have investigated thermal transport in various simple structures, ranging from unpatterned suspended thin films to rectangular cross-section nanowires and fishbone-like periodic PnCs.

In membranes and nanowires, heat transport is purely diffusive at room temperature. While the impact of ballistic phonon transport could not be observed in the thin films even at low temperature, short nanowires (< 4 µm) displayed semi-ballistic transport characteristics at 4 K. This ballisticity results from the long wavelength phonons insensitive to the small surface roughness. Since the specularity is high for these phonons, it is possible that they do not diffusively scatter at all along the wire. Furthermore, the relative impact of surface scattering is enhanced when the lateral dimensions are reduced, an observation that holds at both low and room temperatures.

Although no clear evidence of coherent reduction of the thermal conductivity could be shown in the fishbone PnCs, the effect of surface scattering is, in that case, slightly more complex due to the geometry. Whether at room temperature or below, the main parameter influencing thermal conduction is the width of the neck, i.e., the smallest part through which heat will flow. Its impact is very similar to what is observed in nanowires. However, it is also clear that a further reduction in the thermal conductance, but mostly thermal conductivity, is possible through the tuning of the side fins geometry or their number, that is, the period or the total length of the structure. The comparison between fishbone structures and nanowires at 4 K further demonstrates the partially ballistic nature of phonon transport at this temperature.

Chapter V

Heat conduction tuning in 2D PnCs

V.1 State of the art in 2D PnCs

Although nanowires are the most common type of Si nanostructures that has been investigated, as far as phononic crystals go, fishbone-type structures remain largely unexplored compared to air-hole type structures. Some groups have published results about cross-plane and in-plane thermal conductivities in such periodic air-holes structures; however, the total number of measured structures remains very small. Most data are either considered in terms of the surface-to-volume ratio or the inter-hole spacing, which is equivalent to the neck width in our fishbone nanostructures and is called later on the neck size in the case of 2D structures. These periodic structures range from periodic arrays of nanowires, 2D PnCs of various sizes to nanomesh structures [126,127]. With the aim of reducing the thermal conductivity to the extreme, thus increasing the thermoelectric figure of merit, some porous Si was also engineered with somewhat less periodic configurations [128]. Figure V.1 shows a few SEM images extracted from these major publications in the literature.

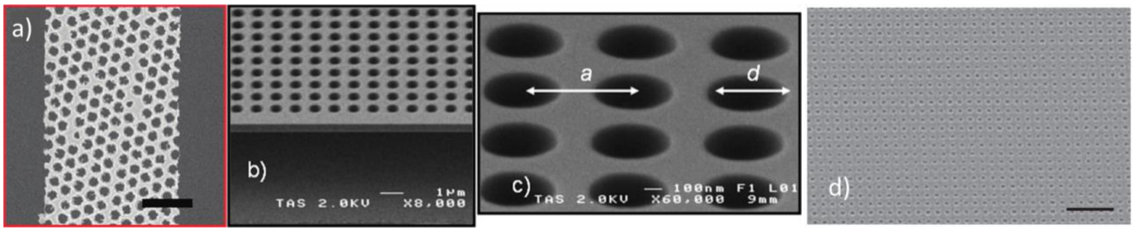

Figure V.1 SEM images of various Si 2D phononic crystals extracted from the literature. a) Holey Si by Tang *et al*. [128]. b) and c) Suspended Si phononic crystal by Hopkins *et al*. [127]. d) Si nanomesh structure by Yu *et al*. [64].

While all these structures are designed to display periodic circular air-holes, it appears that the holes in Figure V.1(a, d) are neither perfectly circular, nor regular, and the roughness in (a) is high (> 5 nm). On the other hand, the circular holes in Figure V.1(b, c) have a well-defined shape, but the characteristic sizes of the structure are above 100 nm. Thus, the easiest way to compare their thermal conductivities is to plot them as a function of the S/V ratio, which is done in Figure V.2 for experimental data at room temperature. The values show an important decrease in thermal conductivity as compared to the bulk, even reaching below 10 W.m^{-1}.K^{-1} for most of them. However, values reported by different groups do not present any clear evolution as a function of the S/V ratio, nor other geometrical parameter. Furthermore, thermal conductivities of 2D PnCs are regularly shown to be much smaller than that of nanowires with similar dimensions. Black open circles represent nanowires by Hochbaum *et al*. [115].

VLS-grown nanowires have an extremely small roughness and their thermal conductivity, above 17 W.m^{-1}.K^{-1}, is well above the 2D PnCs even for a diameter of 37 nm. Rough nanowires, on the other hand, have conductivities below 9 W.m^{-1}.K^{-1}, a result that is more in agreement with the periodic air-hole structures. Although due to the reduced dimensions, in the works of Yu *et al.* and Tang *et al.* for example, the S/V ratios are quite high and the inter-hole distance is very small (< 30 nm), the characteristic dimensions are still similar to that of nanowires. The very low thermal conductivity, which seems hardly explainable by surface scattering, is often partially attributed to the periodicity itself even at room temperature. However, it can be argued that the very high surface roughness, as well as the very small inter-hole distance, can account for most of the reduction in thermal conductivity, as shown by the data on nanowires and further measurements presented in this chapter.

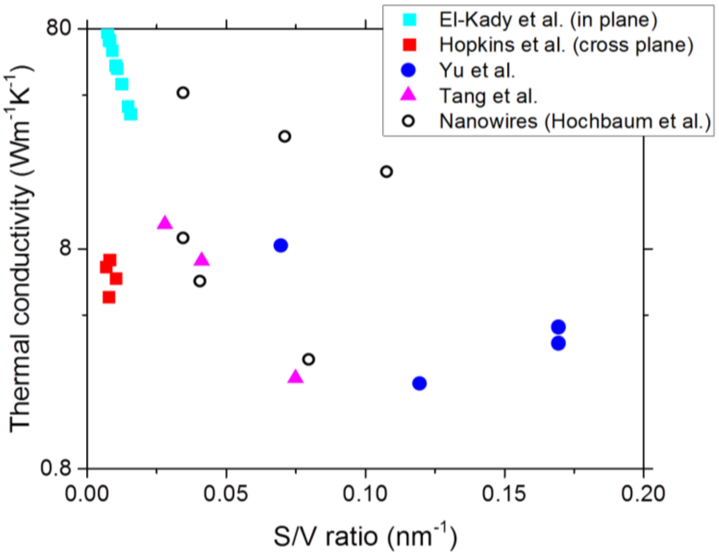

Figure V.2 Thermal conductivity measurements extracted from the literature for 2D PnCs. Squares correspond to in-plane and cross-plane measurements done on similar structures [127,129]; circles correspond to different types of nanostructures with very small dimensions [64] and triangles are holes arranged in an hexagonal lattice [128]. Nanowires [115] are displayed for reference (open circles).

The first clear evidence of coherent thermal transport was presented by Zen *et al.* [41] at very low temperatures (< 1 K). They showed that these structures could be designed to have lower group velocities and reduced density-of-states which lead to a reduced thermal conductance. The measured values agreed very well with the estimations from calculations. SEM images of their structures as well as the transmitted power below 1 K, measured in a dilution fridge, are presented in Figure V.3.

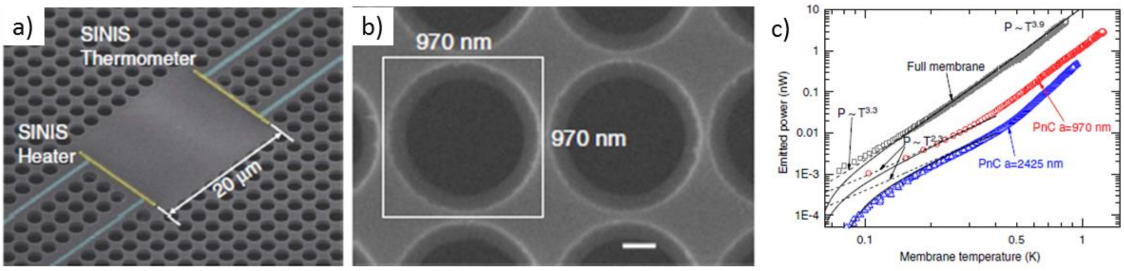

Figure V.3 Engineered thermal conduction in periodic Si nitride membranes. a) SEM image of the phononic crystal with the heater and thermometer used for thermal conduction measurement. b) Close-up view of the PnC. The white square represents the zone covered by a unit cell and the scale bar has a length of 200 nm. c) Transmitted power for an unpatterned membrane as well as two PnCs designed to have lower coherent heat transport properties [41].

Following the lack of systematic data in the literature, as well as the absence of proved coherent thermal conduction until recently, and acknowledging that our measurement system allows us to compare a great number of structures, we designed and fabricated air-hole phononic crystals from the same SOI wafers as the nanowires and fishbone structures. The study of these structures was conducted over two transport regimes, namely incoherent scattering and coherent transport. The goal was to clarify the shape dependence of thermal conductivity while ultimately showing some convincing evidence of coherent thermal transport in Si periodic nanostructures.

V.2 Detail of the fabricated structures

The objective of this study is to comprehensively understand the transport mechanisms of such phononic crystals and the influence of their geometry on their thermal conductivity, since no comprehensive experimental study of this type has been conducted at once. Figure V.4 represents a typical air-hole structure, subsequently called a 2D Phononic crystal (2D PnC) or thermocrystal.

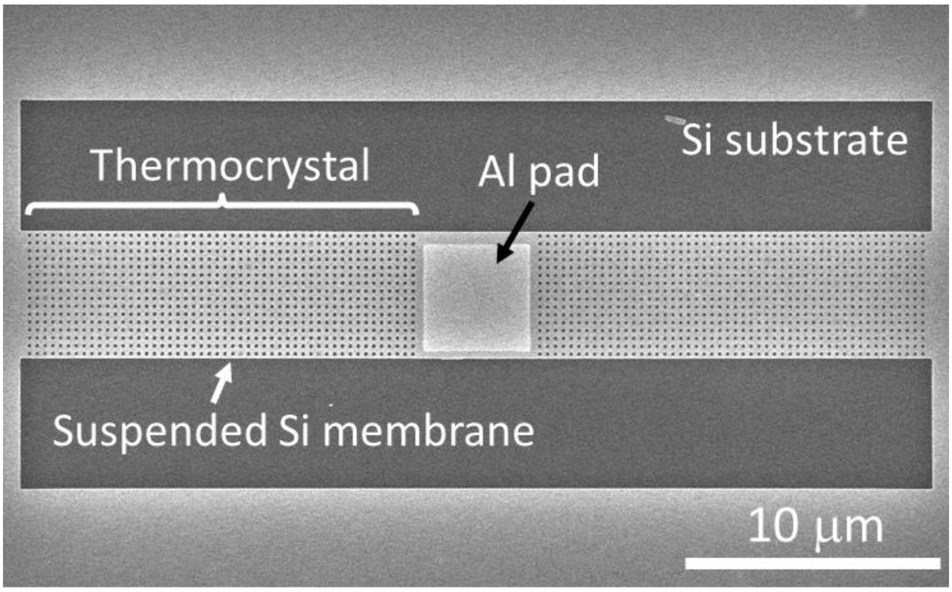

Figure V.4 SEM image of a whole suspended 2D PnC nanostructure. The darker part denotes the underlying substrate.

It has been demonstrated in nanowires and fishbone structures that heat transport at room temperature was purely diffusive. In 2D PnCs, the debate is still ongoing as many groups report anomalous reduction in the thermal conductivity that is hardly explainable by simple incoherent mechanisms. At room temperature, the period of such a PnC cannot compare to the wavelengths of phonons, on the order of a nanometer, while at 4 K the dominant wavelength of 25.5 nm is much closer to the dimensions of the patterned structure. In addition to the wavelengths, a similar problem occurs with the MFPs. While MFPs in the Bulk can be as long as several hundreds of nanometers at room temperature and up to several millimeters at 4 K, the diffusive nature of surface scattering at room temperature is expected to destroy the phase information on much shorter scales than that, as will be shown in section V.3.1.

In this chapter, we will develop our argument about 2D PnCs at room- and low-temperature, first discussing the impact of the geometry on the thermal conductivity and then showing clear evidence of coherent scattering at low temperatures.

As mentioned in section II.2, the principal scattering mechanisms in nanostructures is boundary scattering, which is highly dependent on the surface to volume ratio (S/V ratio). In the case of 2D PnCs with a square lattice, it is possible to calculate the S/V ratio with the following equation:

$$\frac{\mathrm{S}}{\mathrm{V}} = \frac{2 \times \pi \times r \times h + 2 \times (a^2 - \pi r^2)}{(a^2 - \pi r^2) \times h} \tag{5.1}$$

where r is the radius of the holes, a is the period, and h is the thickness of the structure. We can see from this formula that if we want to increase the S/V ratio for a square lattice, it is necessary to increase the radii of the holes. Similar formulas are applicable to hexagonal and triangle lattices, as well as honeycomb. Thus, a radius dependence study on the thermal conductivity was performed for different lattice types and 2 thicknesses, i.e., 145 nm and 80 nm. A similar reasoning can be applied to the neck size, which we have shown has a major influence on thermal conductivity in fishbone nanostructures.

V.3 Thermal properties: lattice type/period/hole sizes

V.3.1 Thicker structures – 145 nm

The first set of experiments was conducted on 145 nm-thick structures with a fixed period of 300 nm and a square arrangement of the holes. The thermal conductivity decreases substantially when the hole size increases, as can be seen in Figure V.5 at room temperature. If the structures with the largest holes, i.e., 270 nm in diameter, are compared to those with the smallest holes, i.e. 110 nm in diameter, the reduction in thermal conductivity exceeds 50%. It is also worth noting that considering a 2D PnC with an average hole size, namely around 200 nm in diameter, yields a decrease of more than 50% compared to the unpatterned thin film of the same thickness.

Above a critical hole size, here around 240 nm in diameter, there seems to be an intensification of the thermal conductivity reduction, which is the counterpart of what is observed in nanowires when the width decreases. To verify the tendency, Monte-Carlo simulations were performed on these configurations. As displayed in Figure V.5, the MC simulations, while slightly overestimating the thermal conductivity, reproduce the tendency reasonably well. The difference in absolute values is mostly attributed to the imperfections in the fabricated structures, such as the surface roughness, as well as the difference in parameters between the FEM and MC simulations.

Furthermore, the MC simulations were used to retrieve the thermal conductivity accumulation as a function of the MFP. In this instance, purely diffusive boundary scattering was assumed. Figure V.5 displays this accumulation for the unpatterned thin film as well as three different hole sizes. In the diffusive regime, it is clear that the maximum attainable MFP is reduced as the hole diameter is increased, i.e., the longest transmitted MFP follows the same trend as the neck size, regardless of the phonons' frequency. Moreover, the smaller the neck, the more short MFPs become important, since long MFPs are cut off and do not participate in thermal transport anymore.

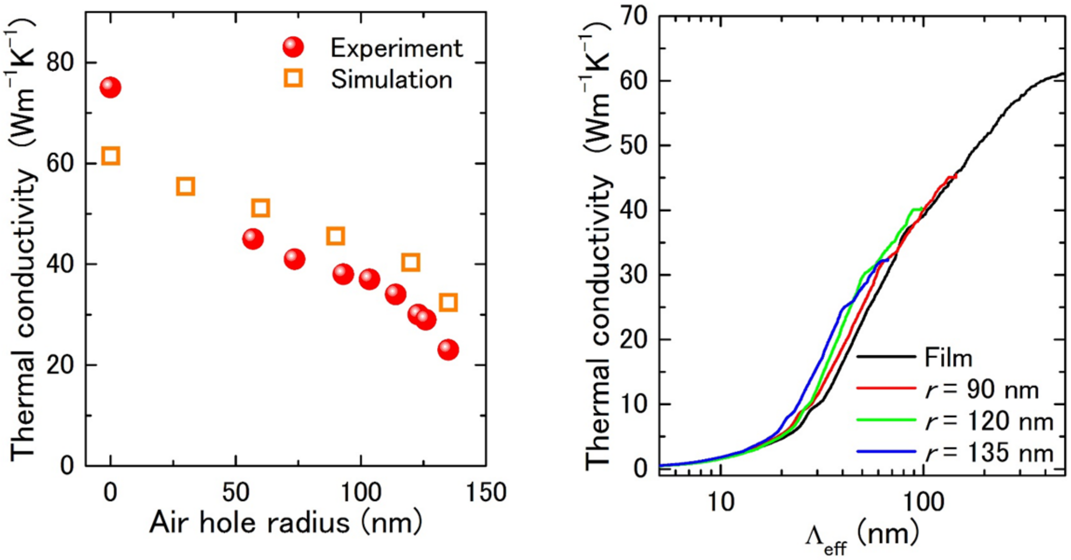

Figure V.5 (a) Thermal conductivity of 2D PnCs with holes of various sizes arranged in a periodic square lattice of period 300 nm. (b) Accumulated thermal conductivity for similar structures calculated by MC simulations. The accumulated thermal conductivity is plotted as a function of the MFPs of phonons [130].

With the shift in the phonon distribution at low temperatures, interplay between diffuse and ballistic scattering is expected to occur. To assess any difference between room- and low-temperature, the same set of data was measured, at 4 K this time. The hole size dependences at both temperatures are plotted on the same graph (Figure V.6), along the membrane. There are two interesting points to notice. The first one is that in this sample, the hole size has a similar impact at 4 K as it has at room temperature. The second is that the thermal conductivity is more strongly reduced at 4 K than at room temperature when compared to the unpatterned thin film. A possible explanation for this reduction can be found by looking at the phonon MFP distribution. It is clear from Figure V.5(b) that the effective phonon MFP will be limited by the size of the holes, independently of temperature. However, the phonon distribution is shifted to longer wavelengths, thus longer MFPs, at lower temperature, following the Planck distribution. Since the MFP will be limited by the geometry in accordance with the MC simulations, it means that at lower temperature, by cutting phonons with long wavelengths, the conductivity is more drastically reduced since these phonons represent a larger part of the heat transport. By performing a temperature dependent study, it should appear that the ratio between the 2D PnC conductivity and that of the thin film is decreasing with temperature monotonously, as was observed for nanowires.

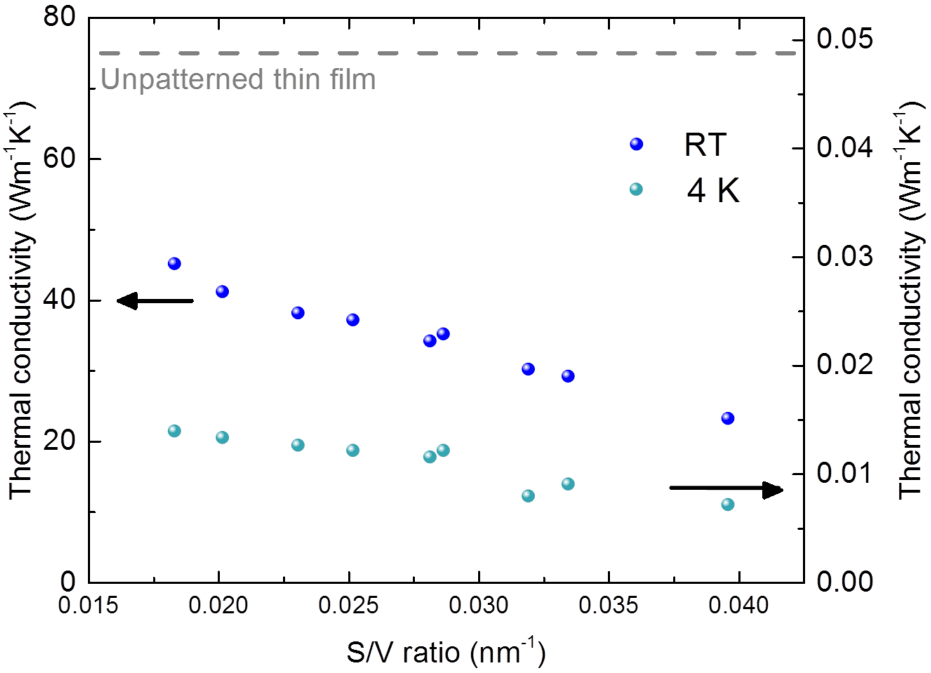

Figure V.6 Comparison between the hole diameter dependence on the thermal conductivity of a periodic square 2D PnC of period 300 nm at room temperature and 4 K [131].

As will be shown in a subsequent section, this additional reduction might also be partially attributed to a coherent decrease in the thermal conductivity due to Bragg reflections. Low temperature MC simulations with partially specular boundary scattering could clarify this phenomenon, as well as the relative impact of the increase in hole diameter.

V.3.2 Thinner structures – 80 nm

The remaining structures were fabricated on an 80 nm-thick SOI wafer and three different lattices were considered: hexagonal, square and honeycomb. Each lattice type is divided in periods of 120, 160, 200, 240, and 280 nm. Moreover, for each of these periods, the diameter of the holes has been varied within the limits of our fabrication capabilities. A total of approximately 30 structures were fabricated for each lattice type. Scanning electron microscopy (SEM) images of the aforementioned lattices with periods of 160 nm (Figure V.7(a), (c), and (e)) and 280 nm (Figure V.7(b), (d), and (f)) show successful patterning with roughness not exceeding a couple nanometers, as it is undistinguishable from the SEM images.

The thermal conductivities of all these structures are displayed in Figure V.7(g-i) at room temperature (upper) and 4 K (lower). The scale bar is common to the three lattice types. The first observation to be made is that, for a given lattice type, reducing the period reduces thermal conductivity, even at a given hole diameter. The difference arises both from the increase in the S/V ratio as the period decreases, and from the neck size, decreasing with the period. A detailed explanation is given at the end of this section. In addition to the change in thermal conductivity with the period, the thermal conductivity decreases as the hole diameter increases for any period and given lattice type, just as was observed for the square structures of period 300 nm fabricated on the 145 nm-thick thin film. The dashed lines in panels g-i are linear fitting of these decreasing trends. The slope is fixed for each lattice type. It consistently follows a similar pattern, whatever the period and temperature, i.e., it increases from hexagonal to square and to honeycomb, respectively. This also corresponds to the order from the most densely packed lattice type to the least densely packed one, i.e., from the highest to the lowest S/V ratio.

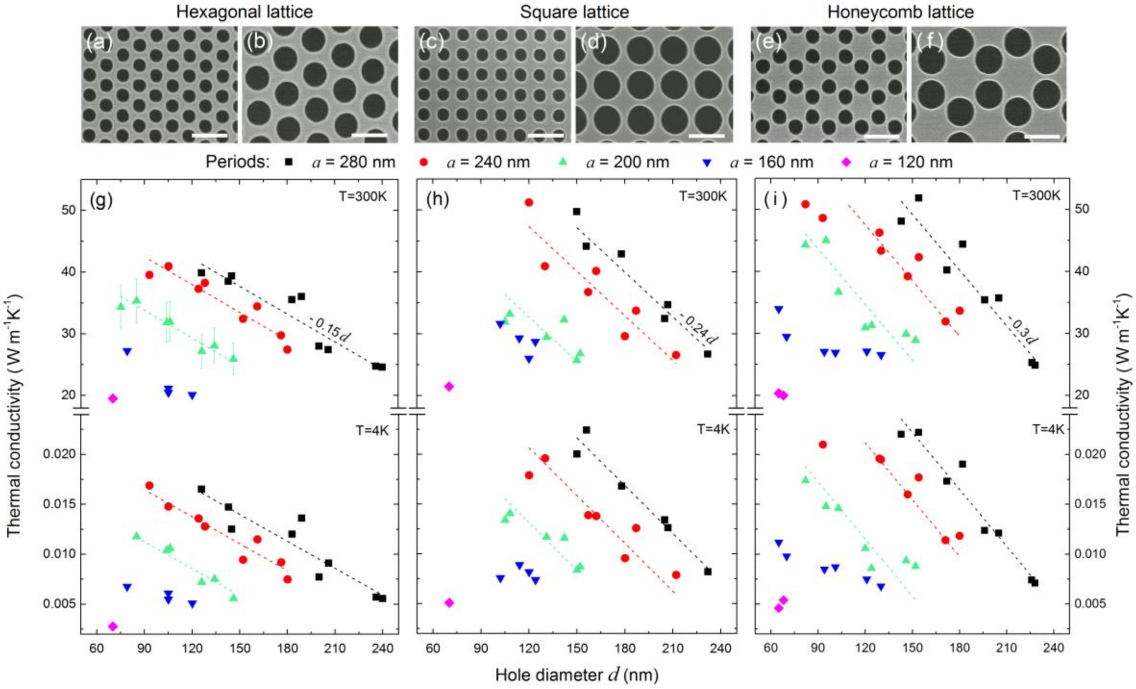

Figure V.7 Thermal conductivity of various 2D PnCs. (a-f) SEM images of 2D PnCs with various arrangements of holes, such as hexagonal (a,b), square (c,d) and honeycomb (e,f) lattice types. Their respective thermal conductivities are plotted in panels g-I at room temperature (upper) and 4 K (lower) for periods of 120 nm (pink), 160 nm (blue), 200 nm (green), 240 nm (red) and 280 nm (black). Dashed lines are linear fits of the results with a fixed inclination per lattice type.

It also appears that the tendencies at room- and low-temperature are very similar, with the exception of their relation to the unpatterned thin film. For a given structure, the thermal conductivity is reduced much more at low temperature than room temperature when compared to the unpatterned thin film. Recently, theoretical investigations on the impact of phonon dispersion modifications on the heat transfer, due to coherent scattering, have been performed on the same structures [43]. It was found that, at low temperatures only, coherent scattering reduces thermal conductivity as compared to the thin film. Moreover, this reduction is independent of the lattice type and is stronger the larger the diameter-to-period ratio. To verify this claim, the ratio (κ_{PnC} / $\kappa_{Membrane}$) is plotted in Figure V.8 at room- and cryogenic temperature.

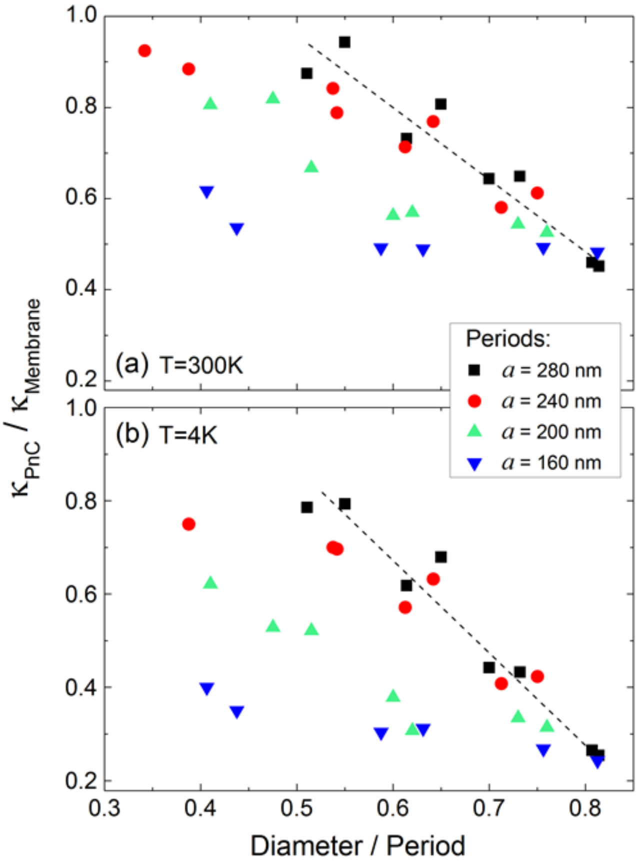

Figure V.8 Thermal conductivity of the 2D PnCs relative to that of the unpatterned suspended thin film of same thickness at (a) room temperature and (b) 4 K for a variety of hole diameters. Colors represent different periods as indicated in the onset. Dashed line are linear fits of the data on structures with *a* = 280 nm.

It is clear, as previously explained, that the thermal conductivity is much more significantly reduced at 4 K than at room temperature, to approximately 20%, whatever the diameter of the holes. Following the fit for the largest period, this relative conductivity decreases with the increase in diameter. It also appears that this reduction is steeper at 4 K than at room temperature. Coherent phonon scattering can thus be a possible interpretation of these observations, combined with the fact that its intensity also corresponds to the expected impact of coherent scattering at 4 K [43]. Indeed, if we consider incoherent scattering mechanisms, three-phonon processes and impurity scattering should not vary from one structure to another and only the amount of boundary scattering should vary. Furthermore, a reduced thermal conductivity for a larger diameter-to-period ratio corroborates the hypothesis of coherent scattering, as was shown theoretically for the exact same structures by Anufriev *et al*. [132].

However, other observations dismiss the fully coherent transport model. First, the coherent simulations point towards a decreased thermal conductivity for larger periods, if it is considered that all phonons are purely coherent, which is the opposite of the trend that is observed here. Nonetheless, it can be argued that, at a given temperature, longer periods affect a smaller portion of the phonon spectrum. This might provide a partial explanation for the trend observed. Secondly, it is observed that, whatever the temperature, period, or lattice type, the thermal conductivity tends towards a similar value, which cannot be explained by coherent scattering. Moreover, similar trends are found at both room- and low-temperature, whereas coherent scattering is expected to affect heat transport mostly at low temperatures only [129]. Thus, the only remaining explanation is to be found with surface boundary scattering. From the previous observation, as well as the period dependence, we can deduct that the boundary scattering probability is linked to the amount of surface that can scatter phonons. Consequently, thermal conductivity should display some form of proportionality to the surface-to-volume (S/V) ratio defined earlier, which was indeed the case for the 145 nm-thick structures of period 300 nm. It can also be said that structures with different periods or lattice types but similar S/V ratios are expected to display a similar thermal conductivity. Figure V.9(a) shows all data grouped by lattice type as a function of their S/V ratio at room temperature. Gray open dots are unpatterned thin films extracted from the literature [100–102,104,133,134] and grey filled points are thin films measured during this work (see Figure IV.2 and Figure V.9)

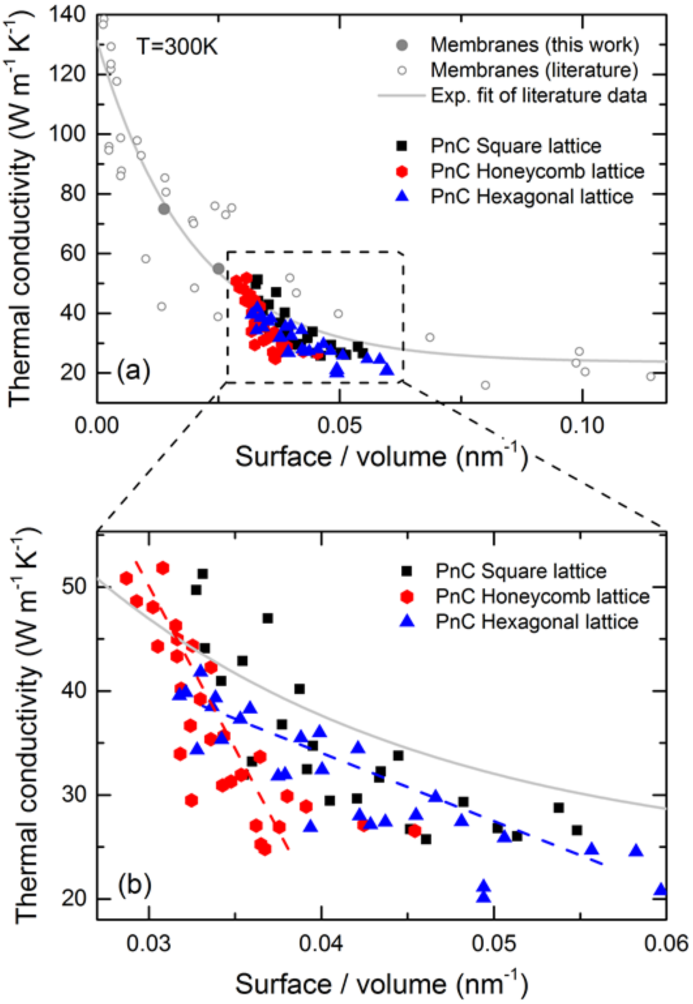

Figure V.9 Thermal conductivity of 2D PnCs plotted as function of their S/V ratio at room temperature. The three different lattice types are represented by red circles for the honeycomb, blue triangles for the hexagonal and black squares for the square lattice type. In grey are plotted various unpatterned thin films from the literature, as well as our own work.

All structures show a reduction in thermal conductivity from the bulk value of 148 W.m^{-1}.K^{-1} which increases with the increase in S/V ratio. The fit (grey line) drawn in Figure V.9(a) depicts the general trend. While it was shown in Chapter IV that our thin films corroborate existing results in the literature, we can see here that it is also generally the case for the 2D PnCs. This suggests that most of the reduction in thermal conductivity compared to the unpatterned thin film is due to boundary scattering. Looking at it in further details (Figure V.9 (b)), we can see however that the three lattice types behave differently. For honeycomb structures, in which holes are the least densely packed, thermal conductivity decreases much faster as a function of the S/V ratio than for the other lattice types. On the other hand, hexagonal structures, which have the most densely packed holes, decay the slowest. In this case, again, it is clear that the minimum value of thermal conductivity reached by each lattice type is seemingly identical and equal to 25 $W.m^{-1}.K^{-1}$. Therefore, the limiting factor in thermal conductivity reduction when the hole diameter approaches the period needs to be found elsewhere. The only remaining dimension that could act as a bottleneck for phonons is the neck size. It has been suggested that this parameter could be used to explain the reduction in porous nanostructures as the hole dimension increases, thanks to what is called the “necking effect” [128,131]. Following this reasoning, it is said that the MFP of phonons is limited by the distance between two holes, i.e. the smallest channel through which phonons can pass. In this work, we clearly demonstrate the impact of the neck size separately from simple surface scattering on the surface of the holes. In Figure V.10, we plot the thermal conductivity of all structures with the honeycomb (red) and hexagonal (blue) lattices at room- and low-temperature as a function of the neck size.

However, as the neck size decreases, the values of thermal conductivity seem to converge, independently of the lattice type or temperature, which means that the observed effect is not directly dependent on the phonon wavelength. Nonetheless, it affects the phonons MFP and thus the thermal conductivity, as was stated in the literature [129].

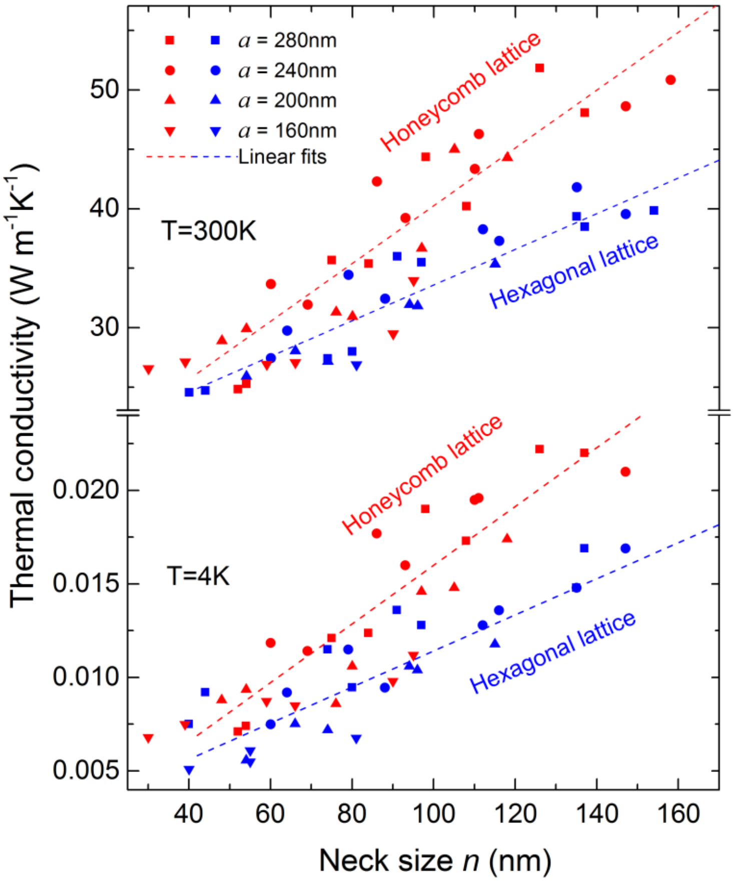

Figure V.10 Thermal conductivity of the structures with hexagonal (blue) and honeycomb (red) lattices as a function of the neck size at 300 and 4 K. Dashed lines are linear fits of the data.

From this figure, we can see that, for large neck sizes, i.e., small holes, the honeycomb lattice structures consistently display a higher thermal conductivity that their hexagonal counterpart, due to the different amount of scatterers. In the honeycomb lattice, every third hole is absent, so the S/V ratio is quite smaller than that of the hexagonal lattice with the same hole/neck size.

V.4 Thermal conductivity tuning by disorder

In the incoherent scattering regime, i.e., mainly boundary scattering for 2D PnCs, the main parameter of interest concerning phonon is their MFP. From a few hundreds of nanometers at room temperature, it increases up to a few millimeters at 4 K in the bulk. However, when switching to coherent scattering via periodic nanostructures, it is crucial to consider the wavelength of phonons, as was demonstrated with the band diagrams displayed in Chapter II. At room temperature, the dominant wavelength is too small for the periodicity of a PnC to be on the same order in size. At 4 K however, this dominant wavelength is around 25 nm. While it is still smaller than the smallest achievable period, this increase, combined with the longer natural MFPs, brings forth the possibility of coherent scattering at 4 K. The samples designed to display this coherent scattering have thus been fabricated as close as possible to the phonon wavelengths dimensions without degradation of the quality. To separate the effect of coherent scattering from the surface scattering, we fabricated structures with the same S/V ratio and similar average neck size, but with different wave properties. The circular holes are periodically aligned in a square lattice of period 300 nm. Suspended microstructures with two different lengths, 10 μm and 15 μm, were designed and, for each length, holes diameters have been changed, ranging from 105 nm to 180 nm. To vary the wave properties of these structures, we introduced disorder in the position of the holes by shifting their position in both planar axes. The quantity of disorder is specified in percent of the period. Each hole is shifted from its original position by a random value in the two in-plane axis, prescribed by:

$$\mathrm{p}(\mathrm{n}\%) = \mathrm{p}_0 \pm \varepsilon * \mathrm{n} * {}^{\mathrm{a}}\!/_{100} \qquad (5.1)$$

where p corresponds to the displaced position, p_0 to the position in the perfectly ordered thermocrystal and ε refers to a random number between 0 and 1. n defines the maximum deviation in percentage of the period a. For each structure type, the disorder has been increased from 0%, i.e., the periodic case, to 21% for long membranes, and to 20% for the short ones. Figure V.11 shows SEM images of the full structure (a) as well as close-up views or different amounts of disorder between the fully periodic one (0%) and the one with 15% disorder (b).

The effective thermal conductivities of all samples were first measured at room temperature as reported in Figure V.12(a). The order of obtained thermal conductivities is consistent with the values previously reported. Furthermore, neither the heat flux nor the thermal conductivity are impacted by the disorder, whatever the magnitude. All the thermal conductivity values remain equal to the average value within a +/- 4% accuracy range.

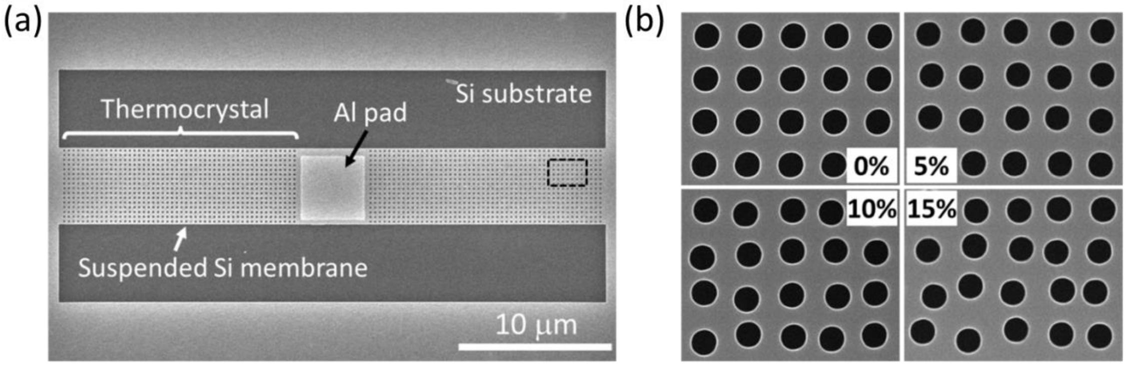

Figure V.11 Fabricated structures and thermal conductivity measurement method for microstructures. (a) SEM image of a fabricated suspended Si thin film with holes arranged in a square lattice. (b) Close-up view of phononic nanostructures with different amount of disorders of 0, 5, 10, and 15%. The scale bar is 300 nm.

As was observed in previously measured structures, increasing the size of the holes decreases (increases) the overall conductance (decay time) by increasing the dimensions of the scattering object, yielding a reduced thermal conductivity [43,128,135]. This trend is further confirmed by the experimental results presented in Figure V.12(a) and (b). It is also possible to observe from these data that structures with similar hole sizes have a lower conductivity as their length increases, in a similar fashion to what happens with fishbone structures at room temperature.

At low temperatures, in Figure V.12(b), we observe that for disorder rates above ~10% (10 μm-long thin films) and 5% (15 μm-long thin films), the decay times are constant within the previously defined +/- 4% inaccuracy region. For longer thermocrystals (15 μm), the plateau of constant conductance is reached for lower disorder amounts than it is for short thermocrystals (10 μm). This particular mechanism will be studied in a further experiment as it is not yet fully understood. However, when the holes' positions are converging towards the ones of the perfect periodic thermocrystal, the decay times increase and the corresponding thermal conductivities decrease. The tuning in transmitted power can then be transposed as a tuning in thermal conductivity, as observed in Figure V.12(d). Whether the structure is 10 or 15 μm long, this tuning occurs exclusively below 10% of disorder.

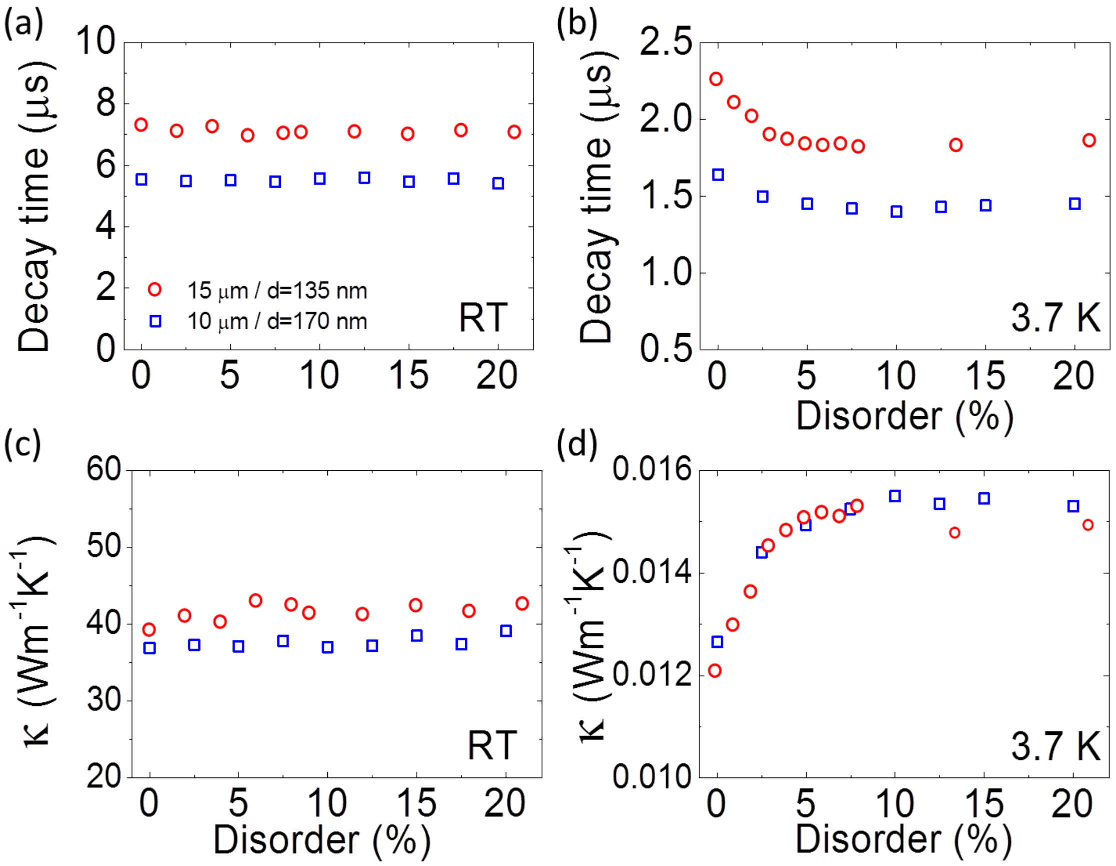

Figure V.12 Decay times and thermal conductivity of the thermocrystals (a) Measured decay times for two different thermocrystals with hole diameters d = 135 nm (red) and d = 170 nm (blue) at room temperature. 10 and 15 µm represent the respective length of the thermocrystals as described in the fabrication section. (b) Decay times for the same structures at 3.7 K. (c) Corresponding effective thermal conductivities for the same set of structures at RT and (d) at 3.7K.

In this experiment, the prescribed low temperature guarantees that some long wavelength phonons will be specularly scattered, i.e. that coherent scattering may happen. This has been further confirmed by experimental results on nanowires and fishbone PnCs, in which specular scattering has been observed. Since the fabrication process has been conducted on the same chip, simultaneously for all the 2D PnCs used in this study, it is possible to assume that all structures possess the same surface roughness. Variations in the inter-hole junctions due to disorder do not explain this trend either, as their size is randomly distributed. Furthermore, it has been shown that a structure with misaligned holes [136] should have a lower thermal conductivity that its aligned counterpart, that is, if phonons are to be treated purely as particles scattered at surfaces. Additionally, during the fabrication, it is possible that the holes diameter slightly varies (< 5%). This cannot explain what is observed here either. Lastly, the impact of a disorder, not in the position, but in the hole size, on the band diagram of phononic structures has been shown by Gomis-Bresco *et al*. [137] to have little impact.

Following the discussions from the structures measured in the previous sections, incoherent scattering mechanisms should not be affected by the presence of disorder. Thus the part of thermal conductivity that is due to incoherent scattering is constant. However, disorder can have a certain effect on the coherent mechanisms at play. Indeed, the dispersion of phonons is formed by both local resonances and Bragg interferences [138]. Bragg diffraction exists mainly for completely periodic structures and reduces thermal conduction, by the intermediary of reduced group velocities in particular, which has been shown by Zen *et al*. [41] and Anufriev *et al*. [43]. However, for Bragg diffraction to occur, it is necessary that the phonons feel the periodicity. This implies that Bragg diffraction will only apply to long-wavelength/long-MFP phonons. The long wavelength can ensure the specularity of scattering and the long MFP, which is related to the wavelength, ensure that these phonons will indeed feel a certain number of periods. Contrary to Bragg diffraction, local resonances are still present even in highly disordered structures, although the behaviors of these resonances will be specific to each structure. Taken separately, these localized modes are not efficient energy carriers. However, it has been shown that a coupling between such modes could happen in disordered systems and thus contribute to a more efficient energy transport. In this experiment, it is plausible that a combination of these two effects is responsible for the trend observed in the thermal conductivity. Considering the Bragg diffraction to be partly responsible is also consistent with our observations at slightly higher temperatures, up to 10 K, as well as with what has been demonstrated for smaller holes by molecular dynamics simulations [139].

Temperature dependence:

In chapter II, we discussed the phonon distribution, i.e. Bose-Einstein distribution, and how increasing the temperature leads to higher frequency modes being populated. Therefore, long-wavelength phonons contribute even less to heat conduction as temperature increases. However, Bragg diffraction can affect only these long wavelength phonons. Since their contribution to heat conduction becomes negligible, so does coherent heat transport. We thus expect that coherent transport mechanisms are highly dependent on temperature and become negligible above a certain temperature.

We measured both periodic and 10% disordered structures for a range of temperatures above the initial 3.7 K until the disappearance of coherence was confirmed. Figure V.13 represents this band folding effect, calculated as follows:

$$D = \frac{(\tau_{0\%} - \tau_{10\%})}{\tau_{10\%}} \tag{5.1}$$

where $\tau_{n\%}$ stands for the decay time of the structure with n% disorder. The values plotted in Figure V.13 are from three different series of structures. It is evident from the figure that the phononic effect decreases with temperature and disappears above 8 K. A possible interpretation is as follows. If we consider a cutoff wavelength – determined for example by the radius of the holes, or the inter-hole spacing – it is possible to consider that all phonons whose wavelength is longer than this distance are coherently affected and thus see their ability to transport heat drastically reduced. As the temperature increases however, these phonons play a less and less important role in phonon transport, thus explaining the decreasing trend observed in Figure V.13.

The series of data clearly indicates that it is impossible to realize a sizable heat flux control by phononic crystal at room temperature with a periodicity above a few hundred nanometers. This finding concurs with existing theoretical reports [129,140]. Additionally, the effective thermocrystal cannot be fabricated by the bottom up approaches such as block copolymer lithography with large disorders. Our findings provide valuable information to develop strategies for heat flux control by thermocrystals. Details about the origin of the observed effect will be reported elsewhere.

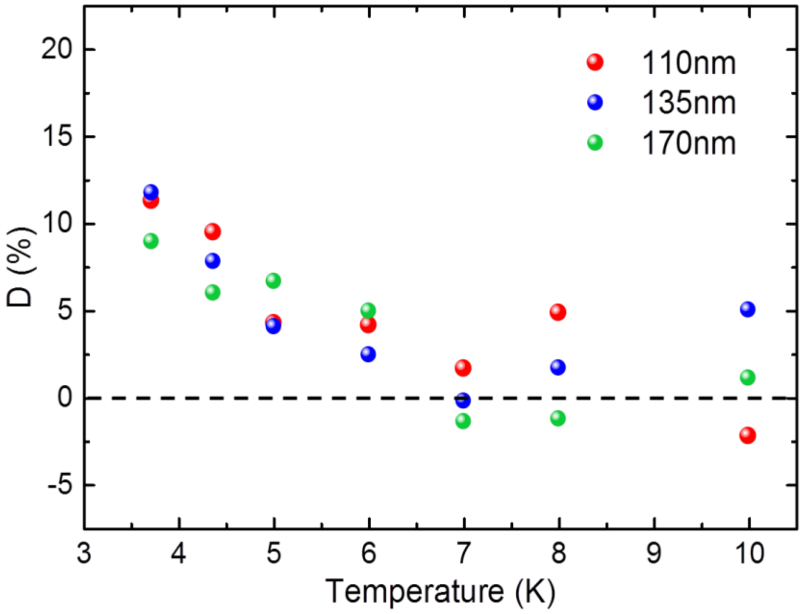

Figure V.13 Temperature dependence of the phononic effect measured for different hole sizes.

V.5 Conclusion on heat transport in 2D PnCs

In this chapter, we have studied heat transport in various kind of 2D PnCs with different lattice types, hole sizes and thicknesses at room temperature and 4 K.

It has been found that, both at room temperature and at 4 K, the thermal conductivity depended on the S/V ratio for most of the structures. However, as soon as the diameter of the holes approaches the period, i.e., when the neck size becomes small enough, this neck size becomes the determining factor for the value of the thermal conductivity. Complementary MC simulations showed that in a purely diffusive regime, the MFP of phonon was directly limited by the neck size, and thermal transport was indeed diffusive at room temperature. Diffusive transport also dominates thermal transport at 4 K as most tendencies observed at room temperature are conserved.

Nonetheless, we demonstrated that it was possible to tune the thermal conductivity of such 2D PnCs at 4 K based solely on the wave nature of phonons. This was achieved by adjusting the amount of disorder in the positions of the holes. A perfectly periodic PnC displayed a lower conductivity than a structure in which the holes positions were random. This effect tends to disappears as the temperature increases and is inexistent in our samples above 8 K.

General conclusion

In this work, we focused on thermal phonon transport in Si nanostructures, especially on PnCs, in order to reveal the wave nature of phonons. As an initial project in the group, we first developed a fabrication and characterization environment. The fabrication is based on classical nanofabrication techniques and was tuned to fit the requirements of PnCs. The characterization technique is based on the thermoreflectance principle, which was also adapted to our need. We performed our analyses thanks to a FEM model used to extract the thermal conductivity.

The results obtained on simple structures such as suspended thin films and nanowires support the findings presented in the existing literature. They also demonstrate the viability of our method. For nanowires, the diffuse boundary scattering of phonons was confirmed at room temperature, whereas at low temperature we observed a shift towards partial specular boundary scattering. Taking this as a starting point, thermal transport in fishbone structures can also be explained by purely diffuse mechanisms at room temperature. Moreover, although their overall conductance is higher than that of nanowires, their thermal conductivity is similar. Defining a transmission function per unit length, we could even observe that such structure displayed a decrease in thermal conductivity when increasing the number of periods. This trend was further confirmed at low temperature, which is cumulated with the decrease due to the partially specular reflections on the surfaces. Our room temperature measurements were further confirmed by MC simulations regarding the thermal conductivity variations with the shape of the side fins. Similarly, switching to 2D PnCs led to a decrease in thermal conductivity, in agreement with MC simulations assuming diffuse scattering. While there were some differences at low temperatures, simply changing the basic shape of such structures did not provide any clear evidence of coherent heat transport. However, by introducing disorder in the hole positions, it was possible to detect variations in thermal conductivity that cannot be explained by the classical incoherent scattering mechanisms. Therefore, we can conclude that this is the first demonstration of thermal tuning in phononic crystals at temperatures above 1 K.

While this work helped establishing experimentally some phenomena pertaining to phonon transport at low and room temperature, much work is still need to be able to use phonons in a manner similar to photons, as well as for the realization of efficient thermoelectric materials.

Based on the present achievements, three main research directions are proposed. First, it would be valuable to develop efficient thermoelectric devices based on Si nanostructures or similar materials, such as Si-germanium (SiGe) alloys. The reduced thermal conductivity of 2D PnCs, as well as their large cross section as compared to nanowires, makes them suitable candidates for such thermoelectric applications. This is especially true for poly-Si structures, which display a comparatively lower thermal conductivity than single-crystalline ones [130,141].

The second research direction we envision is the development of various phononic devices which do not rely exclusively on the thermal conductivity reduction or increase. An example of such devices is the thermal diode, which would pave the way for other phonon logic devices.

The third promising research direction is the development of the coherent phonon transport for various applications. This can certainly encompass the aforementioned thermoelectric devices. Indeed, it has been theoretically shown that it is possible to engineer both the material and the nanostructure shape in order to make use of significant coherent reduction of the thermal conductivity, even at room temperature. Maldovan [142] has demonstrated the pertinence of such a system, using SiGe as the base material.

Lastly, the current optical measurement system that has been developed so far can be improved further. On the one hand, it is possible to automate it in order to simplify measurements even more. On the other hand, it is possible to replace some components permitting the use of even lower laser powers. If these two aspects are reunited, this system could provide a complementary solution to already existing commercially available thermoreflectance systems such as those available from the MicrosanJ or Picotherm companies.

References

[1] “why energy storage is of primary importance,” <http://pythagoreanism.com/why-energy-storage-is-of-primary-importance/>.

[2] L. L. N. Laboratory, “Energy flow charts,” <https://flowcharts.llnl.gov/archive.html#international_archive>.

[3] J. W. Fairbanks, “Thermoelectric Developments For Vehicular Applications,” *DEER Conf.* (2006).

[4] G. J. Snyder and T. S. Ursell, “Thermoelectric efficiency and compatibility.,” *Phys. Rev. Lett.* **91**, 148301 (2003).

[5] G. J. Snyder and E. S. Toberer, “Complex thermoelectric materials.,” *Nat. Mater.* **7**, 105–114 (2008).

[6] A. Majumdar, “Thermoelectricity in Semiconductor Nanostructures,” *Science (80-.).* **303**, 777–778 (2004).

[7] L. M. Goncalves, C. Couto, P. Alpuim, a. G. Rolo, F. Völklein, and J. H. Correia, “Optimization of thermoelectric properties on Bi2Te3 thin films deposited by thermal co-evaporation,” *Thin Solid Films* **518**, 2816–2821 (Elsevier B.V., 2010).

[8] H. Goldsmid, “Bismuth Telluride and Its Alloys as Materials for Thermoelectric Generation,” *Materials (Basel).* **7**, 2577–2592 (2014).

[9] M. Dresselhaus, “Perspectives on Recent Advances in Thermoelectric Materials Research” (2009).

[10] G. a Slack, “CRC Handbook of Thermoelectrics,” in *Handb. Thermoelectr.* (CRC Press, 1995).

[11] T. Caillat, A. Borshchevsky, and O. G. Drive, “Skutterudites: An Update,” 1–11 (1997).

[12] L. D. Hicks and M. S. Dresselhaus, “Thermoelectric figure of merit of a one-dimensional conductor,” *Phys. Rev. B* **47**, 16631–16634 (1993).

[13] L. D. Hicks and M. S. Dresselhaus, “Effect of quantum-well structures on the thermomagnetic figure of merit,” *Phys. Rev. B* **47**, 727–731 (1993).

[14] D. Schurig, J. J. Mock, B. J. Justice, S. A. Cummer, J. B. Pendry, A. F. Starr, and D. R. Smith, “Metamaterial electromagnetic cloak at microwave frequencies.,” *Science* **314**, 977–980 (2006).

[15] M. Nomura, N. Kumagai, S. Iwamoto, Y. Ota, and Y. Arakawa, “Laser oscillation in a strongly coupled single quantum dot-nanocavity system,” *Nat. Phys.* **6**, 279–283 (Nature Publishing Group, 2009).

[16] Y. Akahane, T. Asano, B.-S. Song, and S. Noda, “High-Q photonic nanocavity in a two-dimensional photonic crystal.,” *Nature* **425**, 944–947 (2003).

[17] T. Baba, “Slow light in photonic crystals,” *Nat. Photonics* **2**, 465–473 (2008).

[18] K. Ishizaki, M. Koumura, K. Suzuki, K. Gondaira, and S. Noda, “Realization of three-dimensional guiding of photons in photonic crystals,” *Nat. Photonics* **7**, 133–137 (2013).

[19] A. H. Safavi-Naeini, J. T. Hill, S. Meenehan, J. Chan, S. Gröblacher, and O. Painter, “Two-Dimensional Phononic-Photonic Band Gap Optomechanical Crystal Cavity,” *Phys. Rev. Lett.* **112**, 153603 (2014).

[20] H. Okamoto, A. Gourgout, C.-Y. Chang, K. Onomitsu, I. Mahboob, E. Y. Chang, and H. Yamaguchi, “Coherent phonon manipulation in coupled mechanical resonators,” *Nat. Phys.* **9**, 480–484 (Nature Publishing Group, 2013).

[21] D. Hatanaka, I. Mahboob, K. Onomitsu, and H. Yamaguchi, “A phonon transistor in an electromechanical resonator array,” *Appl. Phys. Lett.* **102**, 213102 (2013).

[22] D. Hatanaka, I. Mahboob, K. Onomitsu, and H. Yamaguchi, “Phonon waveguides for electromechanical circuits,” *Nat. Nanotechnol.* **9**, 520–524 (Nature Publishing Group, 2014).

[23] Y. Fukuta, H. Fujita, and H. Toshiyoshi, “Vapor hydrofluoric acid sacrificial release technique for micro electro mechanical systems using labware,”

Japanese J. Appl. Physics, Part 1 Regul. Pap. Short Notes Rev. Pap. **42**, 3690–3694 (2003).

[24] Z. Tian, K. Esfarjani, J. Shiomi, A. S. Henry, and G. Chen, “On the importance of optical phonons to thermal conductivity in nanostructures,” *Appl. Phys. Lett.* **99**, 7–10 (2011).

[25] Terry M. Tritt, Ed., *Thermal Conductivity - Theory, Properties, and Applications* (Kluwer Academic/Plenum Publishers, 2004).

[26] D. Aketo, T. Shiga, and J. Shiomi, “Scaling laws of cumulative thermal conductivity for short and long phonon mean free paths,” *Appl. Phys. Lett.* **105**, 131901 (2014).

[27] P. G. Klemens, “The Thermal Conductivity of Dielectric Solids at Low Temperatures (Theoretical),” in *Proc. R. Soc. A Math. Phys. Eng. Sci.* **208** (1951).

[28] P. G. Klemens, *Solid State Physics*, F. Seitz and D. Turnbull, Eds. (Academic Press, New York, 1958).

[29] B. Abeles, “Lattice thermal conductivity of disordered semiconductor alloys at high temperatures,” *Phys. Rev.* **131**, 1906–1911 (1963).

[30] J. Callaway, “Model for lattice thermal conductivity at low temperatures,” *Phys. Rev.* **113**, 1046–1051 (1959).

[31] D. Morelli, J. Heremans, and G. Slack, “Estimation of the isotope effect on the lattice thermal conductivity of group IV and group III-V semiconductors,” in *Phys. Rev. B* **66** (2002).

[32] M. Holland, “Analysis of Lattice Thermal Conductivity,” *Phys. Rev.* **132**, 2461–2471 (1963).

[33] C. Herring, “Role of low-energy phonons in thermal conduction,” *Phys. Rev.* **95**, 954–965 (1954).

[34] C. J. Glassbrenner and G. a. Slack, “Thermal conductivity of silicon and germanium from 300K to the melting point,” *Phys. Rev.* **134** (1964).

[35] K. Esfarjani, G. Chen, and H. T. Stokes, “Heat transport in silicon from first-principles calculations,” *Phys. Rev. B - Condens. Matter Mater. Phys.* **84**, 1–11 (2011).

[36] A. A. Maradudin and A. E. Fein, “Scattering of neutrons by an anharmonic crystal,” *Phys. Rev.* **128**, 2589–2608 (1962).

[37] G. P. Srivastava, *The Physics of Phonons* (Taylor and Francis, London, 1990).

[38] R. A. Cowley, “Anharmonic crystals,” in *Reports Prog. Phys.* **31** (2002).

[39] J.-P. M. Peraud, C. D. Landon, and N. G. Hadjiconstantinou, “Monte Carlo Methods for solving the Boltzmann transport equation,” in *Annu. Rev. Heat Transf.* (2014).

[40] S. B. Soffer, “Statistical model for the size effect in electrical conduction,” *J. Appl. Phys.* **38**, 1710–1715 (1967).

[41] N. Zen, T. a Puurtinen, T. J. Isotalo, S. Chaudhuri, and I. J. Maasilta, “Engineering thermal conductance using a two-dimensional phononic crystal.,” *Nat. Commun.* **5**, 3435 (Nature Publishing Group, 2014).

[42] R. Anufriev and M. Nomura, “Thermal conductance boost in phononic crystal nanostructures,” *Phys. Rev. B* **91**, 245417 (2015).

[43] R. Anufriev, J. Maire, and M. Nomura, “Reduction of thermal conductivity by surface scattering of phonons in periodic silicon nanostructures,” *Phys. Rev. B* **93**, 045411 (2016).

[44] J.P. Srivasatava, *Elements of Solid State Physics* (PHI Learning Pvt. Ltd., Dehli, 2014).

[45] A. Majumdar, “Microscale Heat Conduction in Dielectric Thin Films,” *J. Heat Transfer* **115**, 7 (1993).

[46] J. A. Johnson, A. A. Maznev, J. Cuffe, J. K. Eliason, A. J. Minnich, T. Kehoe, C. M. S. Torres, G. Chen, and K. A. Nelson, “Direct measurement of room-temperature nondiffusive thermal transport over micron distances in a silicon membrane,” *Phys. Rev. Lett.* **110** (2013).

[47] Y. He, D. Donadio, J. H. Lee, J. C. Grossman, and G. Galli, “Thermal transport in nanoporous silicon: Interplay between disorder at mesoscopic and atomic scales,” *ACS Nano* **5**, 1839–1844 (2011).

[48] G. Xie, Y. Guo, B. Li, L. Yang, K. Zhang, M. Tang, and G. Zhang, “Phonon surface scattering controlled length dependence of thermal conductivity of silicon nanowires.,” *Phys. Chem. Chem. Phys.* **15**, 14647–14652 (2013).

[49] F. Li and M. K. Balazs, “Native Oxide Growth on Wafer Surface During Final Rinse,” *21st Annu. Semicond. Pure Water Chem. Conf. (SPWCC), St. Clara, Ca*, 1–17 (2002).

[50] Specialty Material Division, “ZEP 520 High Resolution Positive Electron Beam Resist,” *Pediatrics* **108**, 197–205 (2001).

[51] “JEOL_JBX-9300FS Training,” <http://nanolithography.gatech.edu/JEOL_JBX-9300FS_Training.pdf>.

[52] M. A. McCord and M. J. Rooks, Eds., “Microlithography,” in *SPIE Handb. Microlithogr. Micromach. Microfabr.* (2000).

[53] L. Sainiemi, *Cryogenic deep reactive ion etching of silicon micro and nanostructures*, in *Dr. Diss.* (2009).

[54] M. J. De Boer, J. G. E. Gardeniers, H. V. Jansen, E. Smulders, M. J. Gilde, G. Roelofs, J. N. Sasserath, and M. Elwenspoek, “Guidelines for etching silicon MEMS structures using fluorine high-density plasmas at cryogenic temperatures,” *J. Microelectromechanical Syst.* **11**, 385–401 (2002).

[55] S. Tachi, K. Tsujimoto, and S. Okudaira, “Low-temperature reactive ion etching and microwave plasma etching of silicon,” *Appl. Phys. Lett.* **52**, 616–618 (1988).

[56] Z. Liu, Y. Wu, B. Harteneck, and D. Olynick, “Super-selective cryogenic etching for sub-10 nm features.,” *Nanotechnology* **24**, 015305 (2013).

[57] L. Shi, D. Li, C. Yu, W. Jang, D. Kim, Z. Yao, P. Kim, and A. Majumdar, “Measuring Thermal and Thermoelectric Properties of One-Dimensional Nanostructures Using a Microfabricated Device,” *J. Heat Transfer* **125**, 881 (2003).

[58] C. Dames and G. Chen, “1??, 2??, and 3?? Methods for Measurements of Thermal Properties,” *Rev. Sci. Instrum.* **76**, 1–14 (2005).

[59] W. Liu and M. Asheghi, “Phonon-boundary scattering in ultrathin single-crystal silicon layers,” *Appl. Phys. Lett.* **84**, 3819–3821 (2004).

[60] A. M. Marconnet, T. Kodama, M. Asheghi, and K. E. Goodson, “Phonon Conduction in Periodically Porous Silicon Nanobridges,” *Nanoscale Microscale Thermophys. Eng.* **16**, 199–219 (2012).

[61] J. S. Heron, C. Bera, T. Fournier, N. Mingo, and O. Bourgeois, “Blocking phonons via nanoscale geometrical design,” *Phys. Rev. B - Condens. Matter Mater. Phys.* **82**, 1–5 (2010).

[62] J. S. Heron, T. Fournier, N. Mingo, and O. Bourgeois, “Mesoscopic size effects on the thermal conductance of silicon nanowire.,” *Nano Lett.* **10**, 2288 (2010).

[63] O. Bourgeois, T. Fournier, and J. Chaussy, “Measurement of the thermal conductance of silicon nanowires at low temperature,” *J. Appl. Phys.* **101**, 1–4 (2007).

[64] J.-K. Yu, S. Mitrovic, D. Tham, J. Varghese, and J. R. Heath, “Reduction of thermal conductivity in phononic nanomesh structures.,” *Nat. Nanotechnol.* **5**, 718–721 (2010).

[65] A. I. Boukai, Y. Bunimovich, J. Tahir-Kheli, J.-K. Yu, W. a Goddard, and J. R. Heath, “Silicon nanowires as efficient thermoelectric materials.,” *Nature* **451**, 168–171 (2008).

[66] W. Cheng, J. Wang, U. Jonas, G. Fytas, and N. Stefanou, “Observation and tuning of hypersonic bandgaps in colloidal crystals.,” *Nat. Mater.* **5**, 830–836 (2006).

[67] G. S. Doerk, C. Carraro, and R. Maboudian, “Single nanowire thermal conductivity measurements by raman thermography,” *ACS Nano* **4**, 4908–4914 (2010).

[68] S. G. Cloutier, R. S. Guico, and J. M. Xu, “Phonon localization in periodic uniaxially nanostructured silicon,” *Appl. Phys. Lett.* **87**, 1–3 (2005).

[69] J. P. Feser, J. S. Sadhu, B. P. Azeredo, K. H. Hsu, J. Ma, J. Kim, M. Seong, N. X. Fang, X. Li, et al., “Thermal conductivity of silicon nanowire arrays with controlled roughness,” *J. Appl. Phys.* **112** (2012).

[70] J. T. D. A. Young, C. Thomsen, H. T. Grahn, H. J. Maris, “Heat Flow in Glasses on a Picosecond Timescale,” in *Phonon Scatt. Condens. Matter V*, A. C. Anderson and J. P. Wolfe, Eds. (Springer Berlin Heidelberg, 1986).

[71] C. A. Paddock and G. L. Eesley, “Transient thermoreflectance from thin metal films,” *J. Appl. Phys.* **60**, 285–290 (1986).

[72] S. Grauby, B. C. Forget, S. Holé, and D. Fournier, “High resolution photothermal imaging of high frequency phenomena using a visible charge coupled device camera associated with a multichannel lock-in scheme,” *Rev. Sci. Instrum.* **70**, 3603 (1999).

[73] M. Farzaneh, K. Maize, D. Lüerßen, J. a Summers, P. M. Mayer, P. E. Raad, K. P. Pipe, a Shakouri, R. J. Ram, et al., “CCD-based thermoreflectance microscopy: principles and applications,” *J. Phys. D. Appl. Phys.* **42**, 143001 (2009).

[74] Y. S. Ju and K. E. Goodson, “Short-Time-Scale Thermal Mapping of Microdevices Using a Scanning Thermoreflectance Technique,” *J. Heat Transfer* **120**, 306 (1998).

[75] K. Yazawa and D. Kendig, “Understanding the Thermoreflectance Coefficient for High Resolution Thermal Imaging of Microelectronic Devices,” *Electron. Cool.*, 2013.

[76] G. Tessier, S. Holé, and D. Fournier, “Quantitative thermal imaging by synchronous thermoreflectance with optimized illumination wavelengths,” *Appl. Phys. Lett.* **78**, 2267–2269 (2001).

[77] D. G. Cahill, P. V. Braun, G. Chen, D. R. Clarke, S. Fan, K. E. Goodson, P. Keblinski, W. P. King, G. D. Mahan, et al., “Nanoscale thermal transport. II. 2003-2012,” *Appl. Phys. Rev.* **1** (2014).

[78] K. Kang, Y. K. Koh, C. Chiritescu, X. Zheng, and D. G. Cahill, “Two-tint pump-probe measurements using a femtosecond laser oscillator and sharp-edged optical filters,” *Rev. Sci. Instrum.* **79** (2008).

[79] J. P. Feser and D. G. Cahill, “Probing anisotropic heat transport using time-domain thermoreflectance with offset laser spots,” *Rev. Sci. Instrum.* **83** (2012).

[80] V. Moreau, G. Tessier, F. Raineri, M. Brunstein, A. Yacomotti, R. Raj, I. Sagnes, A. Levenson, and Y. De Wilde, “Transient thermoreflectance imaging of active photonic crystals,” *Appl. Phys. Lett.* **96**, 1–4 (2010).

[81] M. Sakata, T. Hori, T. Oyake, J. Maire, M. Nomura, and J. Shiomi, “Tuning thermal conductance across sintered silicon interface by local nanostructures,” *Nano Energy* **13**, 601–608 (Elsevier, 2015).

[82] M. Sakata, T. Oyake, J. Maire, M. Nomura, E. Higurashi, and J. Shiomi, “Thermal conductance of silicon interfaces directly bonded by room-temperature surface activation,” *Appl. Phys. Lett.* **106**, 081603 (2015).

[83] D. G. Cahill, W. K. Ford, K. E. Goodson, G. D. Mahan, A. Majumdar, H. J. Maris, R. Merlin, and S. R. Phillpot, “Nanoscale thermal transport,” *J. Appl. Phys.* **93**, 793–818 (2003).

[84] C. Filloy, G. Tessier, S. Holé, G. Jerosolimski, and D. Fournier, “The contribution of thermoreflectance to high resolution thermal mapping,” in *Sens. Rev.* **23** (2003).

[85] C. Cardenas, D. Fabris, S. Tokairin, F. Madriz, and C. Y. Yang, “Thermoreflectance Measurement of Temperature and Thermal Resistance of Thin Film Gold,” *J. Heat Transfer* **134**, 111401 (2012).

[86] A. Rosencwaig, J. Opsal, W. L. Smith, and D. L. Willenborg, “Detection of thermal waves through optical reflectance,” *Appl. Phys. Lett.* **46**, 1013–1015 (1985).

[87] R. Rosei and D. W. Lynch, “Thermomodulation spectra of Al, Au, and Cu,” *Phys. Rev. B* **5**, 3883–3894 (1972).

[88] M. G. Burzo, P. L. Komarov, and P. E. Raad, “Minimizing the uncertainties associated with the measurement of thermal properties by the transient thermo-reflectance method,” *IEEE Trans. Components Packag. Technol.* **28**, 39–44 (2005).

[89] X. Wang and B. Huang, “Computational Study of In-Plane Phonon Transport in Si Thin Films,” *Sci. Rep.* **4**, 6399 (2014).

[90] M. S. Aubain and P. R. Bandaru, “Determination of diminished thermal conductivity in silicon thin films using scanning thermoreflectance thermometry,” *Appl. Phys. Lett.* **97**, 2010–2013 (2010).

[91] D. P. Sellan, J. E. Turney, a. J. H. McGaughey, and C. H. Amon, “Cross-plane phonon transport in thin films,” *J. Appl. Phys.* **108** (2010).

[92] A. Sikora, H. Ftouni, J. Richard, C. Hébert, D. Eon, F. Omnès, and O. Bourgeois, “Highly sensitive thermal conductivity measurements of suspended membranes (SiN and diamond) using a 3ω-Völklein method,” *Rev. Sci. Instrum.* **83** (2012).

[93] M. Schmotz, P. Bookjans, E. Scheer, P. Leiderer, M. Schmotz, P. Bookjans, E. Scheer, and P. Leiderer, “Optical temperature measurements on thin freestanding silicon membranes,” *Rev. Sci. Instrum.* **81**, 114903 (2010).

[94] J. Cuffe, O. Ristow, E. Chávez, a. Shchepetov, P. O. Chapuis, F. Alzina, M. Hettich, M. Prunnila, J. Ahopelto, et al., “Lifetimes of confined acoustic phonons in ultrathin silicon membranes,” *Phys. Rev. Lett.* **110**, 1–5 (2013).

[95] E. Chávez, J. Cuffe, F. Alzina, C. M. S. Torres, E. Chávez-Ángel, J. Cuffe, F. Alzina, and C. M. Sotomayor Torres, “Calculation of the specific heat in ultra-thin free-standing silicon membranes,” *J. Phys. Conf. Ser.* **395**, 012105 (2012).

[96] E. Houssaine, E. Boudouti, F. Alzina, T. Kehoe, J. Gomis-bresco, D. Dudek, Y. Pennec, B. Djafari-rouhani, M. Prunnila, et al., “Phonons in Slow Motion: Dispersion Relations in Ultrathin Si Membranes,” *Nano Lett.* **12**, 3569–3573 (2012).

[97] J. Cuffe, J. K. Eliason, a. a. Maznev, K. C. Collins, J. a. Johnson, A. Shchepetov, M. Prunnila, J. Ahopelto, C. M. Sotomayor Torres, et al., “Reconstructing phonon

mean-free-path contributions to thermal conductivity using nanoscale membranes," *Phys. Rev. B* **91**, 1–6 (2015).

[98] S.-H. Choi, S. Maruyama, K. Kim, and J. Lee, "Evaluation of the Phonon Mean Free Path in Thin Films by using Classical Molecular Dynamics," 1–18.

[99] S. Neogi, J. S. Reparaz, L. F. C. Pereira, B. Graczykowski, M. R. Wagner, M. Sledzinska, A. Shchepetov, M. Prunnila, J. Ahopelto, et al., "Tuning Thermal Transport in Ultrathin Silicon Membranes by Surface Nanoscale Engineering," *ACS Nano* **9**, 3820–3828 (2015).

[100] M. Asheghi, Y. K. Leung, S. S. Wong, and K. E. Goodson, "Phonon-boundary scattering in thin silicon layers," *Appl. Phys. Lett.* **71**, 1798 (1997).

[101] Y. S. Ju, "Phonon heat transport in silicon nanostructures," *Appl. Phys. Lett.* **87**, 1–3 (2005).

[102] Y. S. Ju and K. E. Goodson, "Phonon scattering in silicon films with thickness of order 100 nm," *Appl. Phys. Lett.* **74**, 3005 (1999).

[103] Z. Hao, L. Zhichao, T. Lilin, T. Zhimin, L. Litian, and L. Zhijian, "Thermal conductivity measurements of ultra-thin single crystal silicon films using improved structure," *2006 8th Int. Conf. Solid-State Integr. Circuit Technol. Proc.*, 2196–2198 (2006).

[104] P. Ferrando-Villalba, a F. Lopeandia, L. Abad, J. Llobet, M. Molina-Ruiz, G. Garcia, M. Gerbolès, F. X. Alvarez, a R. Goñi, et al., "In-plane thermal conductivity of sub-20 nm thick suspended mono-crystalline Si layers.," *Nanotechnology* **25**, 185402 (IOP Publishing, 2014).

[105] A. M. Marconnet, M. Asheghi, and K. E. Goodson, "From the Casimir Limit to Phononic Crystals: 20 Years of Phonon Transport Studies Using Silicon-on-Insulator Technology," *J. Heat Transfer* **135**, 061601 (2013).

[106] M. Asheghi, M. N. Touzelbaev, K. E. Goodson, Y. K. Leung, and S. S. Wong, "Temperature-Dependent Thermal Conductivity of Single-Crystal Silicon Layers in SOI Substrates," *J. Heat Transfer* **120**, 30 (1998).

[107] P. D. Desai, “Thermodynamic Properties of Iron and Silicon,” in *J. Phys. Chem. Ref. Data* **15** (1986).

[108] M. Hasan, M. F. Huq, and Z. H. Mahmood, “A review on electronic and optical properties of silicon nanowire and its different growth techniques.,” *Springerplus* **2**, 151 (2013).

[109] P. R. Bandaru and P. Pichanusakorn, “An outline of the synthesis and properties of silicon nanowires,” *Semicond. Sci. Technol.* **25**, 024003 (2010).

[110] N. Jahr, C. Leiterer, A. Csa, and W. Fritzsche, “Optical Properties of Individual Silicon Nanowires for Photonic Devices,” *ACS Nano* **4**, 7113–7122 (2010).

[111] K.-Q. Peng, X. Wang, L. Li, Y. Hu, and S.-T. Lee, “Silicon nanowires for advanced energy conversion and storage,” *Nano Today* **8**, 75–97 (2013).

[112] J. Zou and A. Balandin, “Phonon heat conduction in a semiconductor nanowire,” *J. Appl. Phys.* **89**, 2932–2938 (2001).

[113] N. Mingo, “Calculation of nanowire thermal conductivity using complete phonon dispersion relations,” *Phys. Rev. B* **68**, 113308 (2003).

[114] D. Dávila, A. Tarancón, C. Calaza, M. Salleras, M. Fernández-Regúlez, A. San Paulo, and L. Fonseca, “Monolithically integrated thermoelectric energy harvester based on silicon nanowire arrays for powering micro/nanodevices,” *Nano Energy* **1**, 812–819 (2012).

[115] A. I. Hochbaum, R. Chen, R. D. Delgado, W. Liang, E. C. Garnett, M. Najarian, A. Majumdar, and P. Yang, “Enhanced thermoelectric performance of rough silicon nanowires.,” *Nature* **451**, 163–167 (2008).

[116] K. Hippalgaonkar, B. Huang, R. Chen, K. Sawyer, P. Ercius, and A. Majumdar, “Fabrication of microdevices with integrated nanowires for investigating low-dimensional phonon transport,” *Nano Lett.* **10**, 4341–4348 (2010).

[117] J. Lim, K. Hippalgaonkar, S. C. Andrews, and A. Majumdar, “Quantifying Surface Roughness E ff ects on Phonon Transport in Silicon Nanowires,” *Nano Lett.* **12**, 2475–2482 (2012).

[118] A. I. Cocemasov, D. L. Nika, V. M. Fomin, D. Grimm, and O. G. Schmidt, “Phonon-engineered thermal transport in Si wires with constant and periodically modulated cross-sections: A crossover between nano- and microscale regimes,” *Appl. Phys. Lett.* **107**, 011904 (2015).

[119] T.-K. Hsiao, H.-K. Chang, S.-C. Liou, M.-W. Chu, S.-C. Lee, and C.-W. Chang, “Observation of room-temperature ballistic thermal conduction persisting over 8.3 µm in SiGe nanowires.,” *Nat. Nanotechnol.* **8**, 534–538 (Nature Publishing Group, 2013).

[120] T.-K. Hsiao, B.-W. Huang, H.-K. Chang, S.-C. Liou, M.-W. Chu, S.-C. Lee, and C.-W. Chang, “Micron-scale ballistic thermal conduction and suppressed thermal conductivity in heterogeneously interfaced nanowires,” *Phys. Rev. B* **91**, 035406 (2015).

[121] W. Fon, K. Schwab, J. Worlock, and M. Roukes, “Phonon scattering mechanisms in suspended nanostructures from 4 to 40 K,” *Phys. Rev. B* **66**, 3–7 (2002).

[122] C. Blanc, A. Rajabpour, S. Volz, T. Fournier, and O. Bourgeois, “Phonon heat conduction in corrugated silicon nanowires below the Casimir limit,” *Appl. Phys. Lett.* **103** (2013).

[123] X. Zianni, “Diameter-modulated nanowires as candidates for high thermoelectric energy conversion efficiency,” *Appl. Phys. Lett.* **97**, 1–4 (2010).

[124] X. Zianni and P. Chantrenne, “Thermal conductivity of diameter-modulated silicon nanowires within a frequency-dependent model for phonon boundary scattering,” *J. Electron. Mater.* **42**, 1509–1513 (2013).

[125] D. L. Nika, A. I. Cocemasov, C. I. Isacova, A. A. Balandin, V. M. Fomin, and O. G. Schmidt, “Suppression of phonon heat conduction in cross-section-modulated nanowires,” *Phys. Rev. B - Condens. Matter Mater. Phys.* **85** (2012).

[126] J.-K. Yu, S. Mitrovic, D. Tham, J. Varghese, and J. R. Heath, “Reduction of thermal conductivity in phononic nanomesh structures.,” *Nat. Nanotechnol.* **5**, 718–721 (Nature Publishing Group, 2010).

[127] P. E. Hopkins, C. M. Reinke, M. F. Su, R. H. Olsson, E. a. Shaner, Z. C. Leseman, J. R. Serrano, L. M. Phinney, and I. El-Kady, “Reduction in the thermal conductivity of single crystalline silicon by phononic crystal patterning,” *Nano Lett.* **11**, 107–112 (2011).

[128] J. Tang, H. T. Wang, D. H. Lee, M. Fardy, Z. Huo, T. P. Russell, and P. Yang, “Holey silicon as an efficient thermoelectric material,” *Nano Lett.* **10**, 4279–4283 (2010).

[129] A. Jain, Y. J. Yu, and A. J. H. McGaughey, “Phonon transport in periodic silicon nanoporous films with feature sizes greater than 100 nm,” *Phys. Rev. B* **87**, 195301 (2013).

[130] M. Nomura, Y. Kage, J. Nakagawa, T. Hori, J. Maire, J. Shiomi, R. Anufriev, D. Moser, and O. Paul, “Impeded thermal transport in Si multiscale hierarchical architectures with phononic crystal nanostructures,” *Phys. Rev. B* **91**, 205422 (2015).

[131] M. Nomura, J. Nakagawa, Y. Kage, J. Maire, D. Moser, and O. Paul, “Thermal phonon transport in silicon nanowires and two-dimensional phononic crystal nanostructures,” *Appl. Phys. Lett.* **106**, 143102 (2015).

[132] R. Anufriev and M. Nomura, “Reduction of thermal conductance in two-dimensional phononic crystals by coherent phonon scattering,” *Phys. Rev. B* **93**, 045410 (2016).

[133] E. Chávez-Ángel, J. S. Reparaz, J. Gomis-Bresco, M. R. Wagner, J. Cuffe, B. Graczykowski, a. Shchepetov, H. Jiang, M. Prunnila, et al., “Reduction of the thermal conductivity in free-standing silicon nano-membranes investigated by non-invasive Raman thermometry,” *APL Mater.* **2** (2014).

[134] J. Li, Q. Zeng, and Z. Liu, “Enhanced resonance transmission of acoustic waves based on asymmetric excitation of Lamb waves in phononic crystals with wedges-like structures,” *J. Appl. Phys.* **116**, 073510 (2014).

[135] J. Nakagawa, Y. Kage, T. Hori, J. Shiomi, and M. Nomura, “Crystal structure dependent thermal conductivity in two-dimensional phononic crystal nanostructures,” *Appl. Phys. Lett.* **107**, 023104 (2015).

[136] B. Fu, G. H. Tang, and C. Bi, “Thermal conductivity in nanostructured materials and analysis of local angle between heat fluxes,” *J. Appl. Phys.* **116**, 124310 (2014).

[137] J. Gomis-Bresco, D. Navarro-Urrios, M. Oudich, S. El-Jallal, A. Griol, D. Puerto, E. Chavez, Y. Pennec, B. Djafari-Rouhani, et al., “A 1D Optomechanical crystal with a complete phononic band gap,” *Nat. Commun.* **5**, 1401.1691 (2014).

[138] Y. Achaoui, V. Laude, S. Benchabane, and A. Khelif, “Local resonances in phononic crystals and in random arrangements of pillars on a surface,” *J. Appl. Phys.* **114**, 104503 (2013).

[139] R. Dettori, C. Melis, R. Rurali, and L. Colombo, “Model for thermal conductivity in nanoporous silicon from atomistic simulations,” *Phys. Rev. B* **91**, 1–10 (2015).

[140] E. Dechaumphai and R. Chen, “Thermal transport in phononic crystals: The role of zone folding effect,” *J. Appl. Phys.* **111**, 073508 (2012).

[141] M. Nomura, Y. Kage, D. Müller, D. Moser, and O. Paul, “Electrical and thermal properties of polycrystalline Si thin films with phononic crystal nanopatterning for thermoelectric applications,” *Appl. Phys. Lett.* **106**, 223106 (2015).

[142] M. Maldovan, “Sound and heat revolutions in phononics.,” *Nature* **503**, 209–217 (Nature Publishing Group, 2013).

dernière page de la thèse

AUTORISATION DE SOUTENANCE

Vu les dispositions de l'arrêté du 7 août 2006,

Vu la demande du Directeur de Thèse

Monsieur C. SEASSAL

et les rapports de

Monsieur I. MAASILTA
Professor - University of Jyväskylä - Survontie 9C P.O. Box 35 (YFL) Jyväskylä FI-40014 Finland

Et de

Monsieur O. BOURGEOIS
Directeur de Recherche CNRS - Institut Néel - 25 avenue des Martyrs bâtiment E - bureau E 412 - BP 166
38042 Grenoble cedex 9

Monsieur MAIRE Jérémie

est autorisé à soutenir une thèse pour l'obtention du grade de **DOCTEUR**

Ecole doctorale ELECTRONIQUE, ELECTROTECHNIQUE, AUTOMATIQUE

Fait à Ecully, le 27 novembre 2015

P/Le directeur de l'E.C.L.
La directrice des Etudes

M-A. GALLAND

ECOLE CENTRALE DE LYON
Service Scolarité
ECULLY